Microrheology of Biomaterials in Healthcare Applications

A thesis submitted
in partial fulfillment of the requirements
for the degree of
Doctor of Philosophy

by

Mr. Nayanjyoti Kakati

Department of Chemical Engineering
Indian Institute of Technology Guwahati
December 2024

CERTIFICATE

It is certified that the works contained in this thesis entitled "**Microrheology of Biomaterials in Healthcare Applications**" by Mr. Nayanjyoti Kakati, have been carried out under my supervision and have not been submitted as a thesis elsewhere for a Ph.D degree.

Thesis supervisor
Prof. Dipankar Bandyopadhyay
Professor
Department of Chemical Engineering,
Centre for Nanotechnology, &
Jyoti and Bhupat Mehta School of Health
Sciences and Technology
Indian Institute of Technology Guwahati
October, 2024

ACKNOWLEDGEMENT

“विद्या ददाति विनयं विनयाद् याति पात्रताम्।
पात्रत्वात् धनमाप्नोति धनात् धर्मं ततः सुखम्॥”

Meaning: Knowledge imparts humility, from humility comes worthiness. With worthiness comes wealth, from wealth, righteousness, and from righteousness, happiness.

In this voyage of discovery, where knowledge meets perseverance, I find myself indebted to souls who bestowed their brilliance.

I express my profound gratitude to my thesis supervisor, **Prof. Dipankar Bandyopadhyay**. His continuous guidance, invaluable advice, and thought-provoking discussions have been vital to my study. Despite his hectic work schedule, he always found time to analyze problems and offer essential suggestions to improve my work. Working under his supervision greatly influenced my life. His commitment to his profession, unwavering quest for excellence, and patience in mentoring novice researchers will always inspire me. It is an honor to have been mentored by him. I am extremely thankful to my doctoral committee members, **Prof. Siddhartha Sankar Ghosh**, Department of Biosciences and Bioengineering Engineering, **Prof. Tapas Kumar Mandal**, Department of Chemical Engineering, and **Prof. Partha Sarathi Gooh Pattader**, Department of Chemical Engineering, for their invaluable suggestions and efforts during my thesis work. My heartfelt gratitude also extends to **Prof. Omkar Suresh Deshmukh** from the Department of Chemical Engineering for his invaluable suggestions in my work.

I wish to express my greatest gratitude to my best friends, **Dr. Abhijit Mazumdar** and **Dr. Aniruddha Mazumdar** for supporting and motivating me throughout my PhD journey. I am very grateful to **Dr. Nabendu Paul**, **Ms. Tanusree Ghoshal**, **Mr. Saurabh Dubey**, and **Mr. Jiwajyoti Mahanta** for their support in experiments and computations.

I am also deeply thankful to all the members of our research group: **Mr. Prathu Raja Parmar**, **Mr. Chintak K. Parashar**, **Ms. Devi Rupa Saha**, **Mr. Ankit Chowdhury**, **Dr. Mitali Basak**, **Mr. Sahil Jagnani**, **Mr. Sanbed Das**, **Ms. Srijita De**, **Mr. Rahul Deka**, **Mr. Vinod Vanarse,** **Mr. Shubham Sanjay Agrawal**, **Mr. Aman Paul**, **Mr. Musaddique Mahfuz Ahmed**, **Ms. Debashreeta Singha**, **Ms. Aayushi**, **Mr. Yeshudan Bora**, **Mr. Arijit Mohanta**, **Dr. Satarupa Dutta**, **Dr. Joidip Chaudhury**, **Dr. Shirsendu Mitra**, **Dr. Siddharth Thakur**, **Dr.**

Surjendu Maity and **Dr. Tamanna Bhuyan**. I am grateful to my friends and colleagues **Ms. Anindita Talukdar**, **Mr. Nayanmoni Baishya**, **Mr. Rijuban Rangslang**, **Mr. Abhishek Paikray, and Dr. Sashank Kulkarni**, whose companionship made my stay at IIT Guwahati memorable.

Special thanks to all the faculty and staff members of the Centre for Nanotechnology, Department of Chemical Engineering, Department of Chemistry, and Central Instruments Facility, IIT Guwahati, for their support and cooperation. I also acknowledge the support from the Analytical Laboratory in Chemical Engineering, Centre for Nanotechnology, Department of Chemistry, and Central Instruments Facility, IIT Guwahati, for providing essential characterization facilities.

Above all, I wish to thank my Parents, and my family members for their unwavering love and support.

Nayanjyoti Kakati

Dedicated to M*y Family*


Indian Institute of Technology Guwahati

SYNOPSIS

Microrheology of Biomaterials in Healthcare Applications

1.Introduction

Rheology originates from the Greek terms "Rheo" for flow and "logos" for study, and is related to the investigation of the flow properties of diverse materials. In general, the materials can be typically categorized into elastic, viscous, and viscoelastic types based on their mechanical behaviors. Examples of viscous materials encompass water, ethanol, and honey, which flow easily, while elastic materials like steel, wood, and plastic possess the ability to store energy. The viscoelastic substances exhibit both elastic and viscous characteristics, as observed in blood, synovial fluid, mucus, and tissues. Viscoelastic liquids, displaying both elasticity and viscosity, may be of Newtonian and Hookean type and may also demonstrate non-Newtonian and non-Hookean behaviors, with viscosity (elasticity) altering in response to shear rates (shear stress). The rheological studies of such materials hold extensive applications across various domains such as material science, healthcare, drug delivery, food processing, cosmetics, and pharmaceuticals.

Thus far, among the other methodologies, two principal measurement techniques are employed to uncover the rheological aspects of diverse materials: (a) bulk rheology measurements – providing comprehensive rheological insights, and (b) microrheology measurements – enabling localized analysis of viscous and elastic properties. In particular, microrheology offers advantages over traditional methods, requiring minimal sample volume and facilitating non-destructive analysis across a broader frequency spectrum. Given the delicate nature of biological materials, microrheology plays a crucial role in investigating the flow properties. For instance, mucus, synovial fluid, blood, and cerebrospinal fluids exhibit distinct viscoelastic behaviors, alterations of which may implicate various pathological conditions. Microrheological investigations are pivotal for understanding the fundamental properties of these materials and devising solutions to various pathological conditions.

For example, in recent years, the research on mucus has gained significant attention within the area of biophysics. This focus ranges from the fundamental processes underlying mucus assembly to exploring its potential in facilitating oral drug delivery. Mucus research has provided insights into engineering the mucus layer to enhance drug delivery efficiency and simulate disease conditions. Mucus is integral to maintaining physiological equilibrium, serving functions such as pathogen prevention and nutrient absorption. It acts as a barrier, safeguarding epithelial linings against toxic gastrointestinal fluids.

Furthermore, research focusing on mucus-microbe interactions helps in understanding pathogen evasion strategies and facilitates the development of antimicrobial interventions. Conversely, the mucus barrier poses challenges for formulating oral drug treatments. For example, it has been reported recently that the use of ionic liquids helps in manipulating the mucus layer for drug delivery purposes. However, there is a requirement for comprehensive investigations, particularly from a microrheological perspective.

On the other hand, synovial fluid is another vital biofluid that enables smooth joint movement across the animal kingdom. It serves as a lubricant and provides nourishment to cartilage and cushions against shock during motion. Synovial fluid has unique viscoelastic properties and preserves optimal joint functionalities. Disruption of this distinctive viscoelastic fluid is observed in diverse arthritic conditions. Hence, research on the synovial fluid is important to understand its viscoelastic behavior as well as identify potential therapeutic targets for arthritis treatment. A microrheological investigation of synovial fluid can be utilized to elucidate the assembly processes of this biofluid and advance the development of artificial viscosupplements.

In view of this background, the current thesis explores the microrheology of two different biomaterials—mucus and synovial fluid in the direction of self-assembly, drug delivery, disease model, and therapeutic intervention. The objectives of the thesis follow:

- Microrheology of mucin-albumin assembly using diffusing wave spectroscopy
- Microrheological investigation of ionic liquid doped mucus for effective delivery of protein-based drugs
- Lactic acid-induced colloidal microrheology of synovial fluids
- Designing an Articular Viscosupplement for Rheumatoid Arthritis Using Microrheological Analysis

The thesis focuses on addressing the aforementioned objectives in four chapters. A detailed list of the publications has been provided at the end of the thesis in Appendix 1.

2. Microrheology of Mucin-Albumin Assembly using Diffusing Wave Spectroscopy

In Chapter 2, we use diffusing wave spectroscopy (DWS), to investigate the microrheological characteristics over a wide range of frequencies (~10^{-1} to 10^{7} Hz) of mucin in the presence of albumin, which is rather impossible for the conventional bulk rheological measurement techniques. Such non-invasive measurements unveil that indeed the interaction between the mucus proteins and albumin can significantly change the rheological properties, which may lead to a diseased condition beyond a critical limit. The chapter also provides evidence related to the physical and electrostatic interaction in such systems with the help of isothermal titration calorimetry (ITC) to check the binding affinity of mucin and BSA. Further, the evidence on the formation of secondary structures of mucin-BSA complexes is unearthed with the help of circular dichroism (CD) experiments.

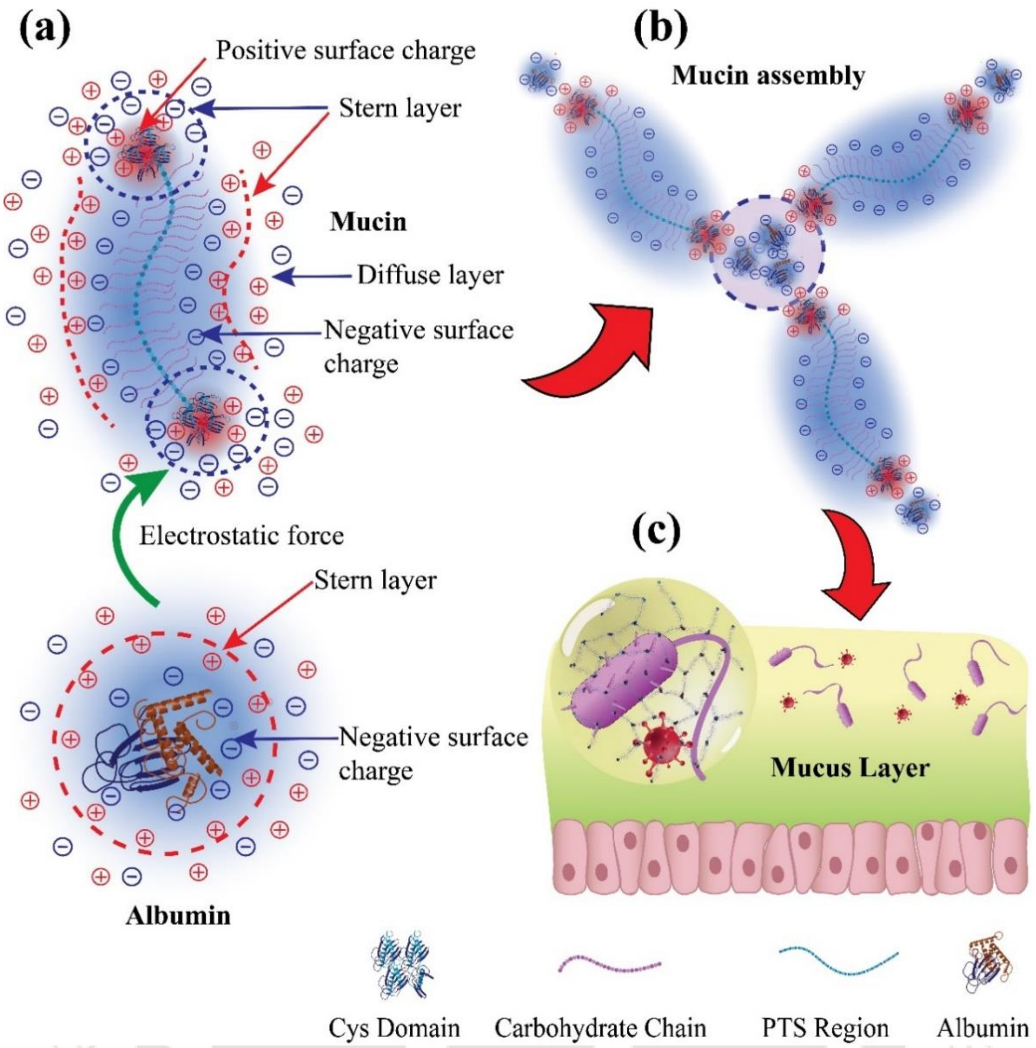

Figure 1. Schematic diagram of mucin-albumin assembly. (a) Structure of mucin monomer with negatively charged carbohydrate chains in PTS region and positively charged cysteine rich domains at the ends. Albumin interacts with the cysteine domains of mucin facilitating mucin-mucin binding. (b) Mucin-albumin interaction leads to assembly of more mucin molecules. (c) Hierarchical assembly of mucin-albumin complex with decreased diffusivity, which restricts the penetration of pathogens through the mucus layer.

The morphological changes during such interactions are also captured using high-resolution atomic force microscopy (AFM). In a nutshell, the chapter unveils and establishes the possible interactions between the albumin and mucin protein in the mucosal layer, which may help in mucin gel assembly to protect the epithelial cells by inhibiting the penetration of bacterial and viral pathogens through the mucus layer. In another way, when the concentration of non-mucin protein rises, it might create a more stiffed mucus layer leading to diseased conditions.

3. Microrheology of Ionic Liquid Doped Mucus for an Efficient Delivery of Protein-based Oral Drugs

Developing protein-based drugs for oral administration is one of the most challenging aspects of pharmaceutical academia and industry. Such medications are rather less bioavailable due to their low stability alongside their inability to permeate through the intestinal barriers of mucus. A few recent works have shown that ionic liquids (ILs) can be combined with protein-based drugs to improve their stability under in-vivo conditions alongside improving their mucus-penetrating capabilities. However, one of the major knowledge gaps in this direction has been the interactions of protein-based drugs, ILs, and mucin, which play a pivotal role in such drug delivery systems.

In Chapter 3, with the help of systematic experiments and DFT simulations, we unveil the diverse molecular mechanisms that play key roles during the delivery of protein-based drugs. The chapter employs a model mesoscale drug delivery system composed of an IL–choline bicarbonate-maleic acid, a protein–mucin, and bovine serum albumin (BSA) as a model drug. In particular, following the microrheological changes of such systems helps in tracing the molecular interactions at the various stages of BSA, mucin, and IL assemblage, which has been corroborated by morphological studies using atomic force microscopy (AFM). Further, DFT simulation sheds light on the interactions of ionic liquids on the different components of mucin monomer. Finally, a human intestine has been simulated as a biomimetic in-vitro microfluidic prototype to demonstrate a larger stability and penetration of BSA through mucin in the presence of IL.

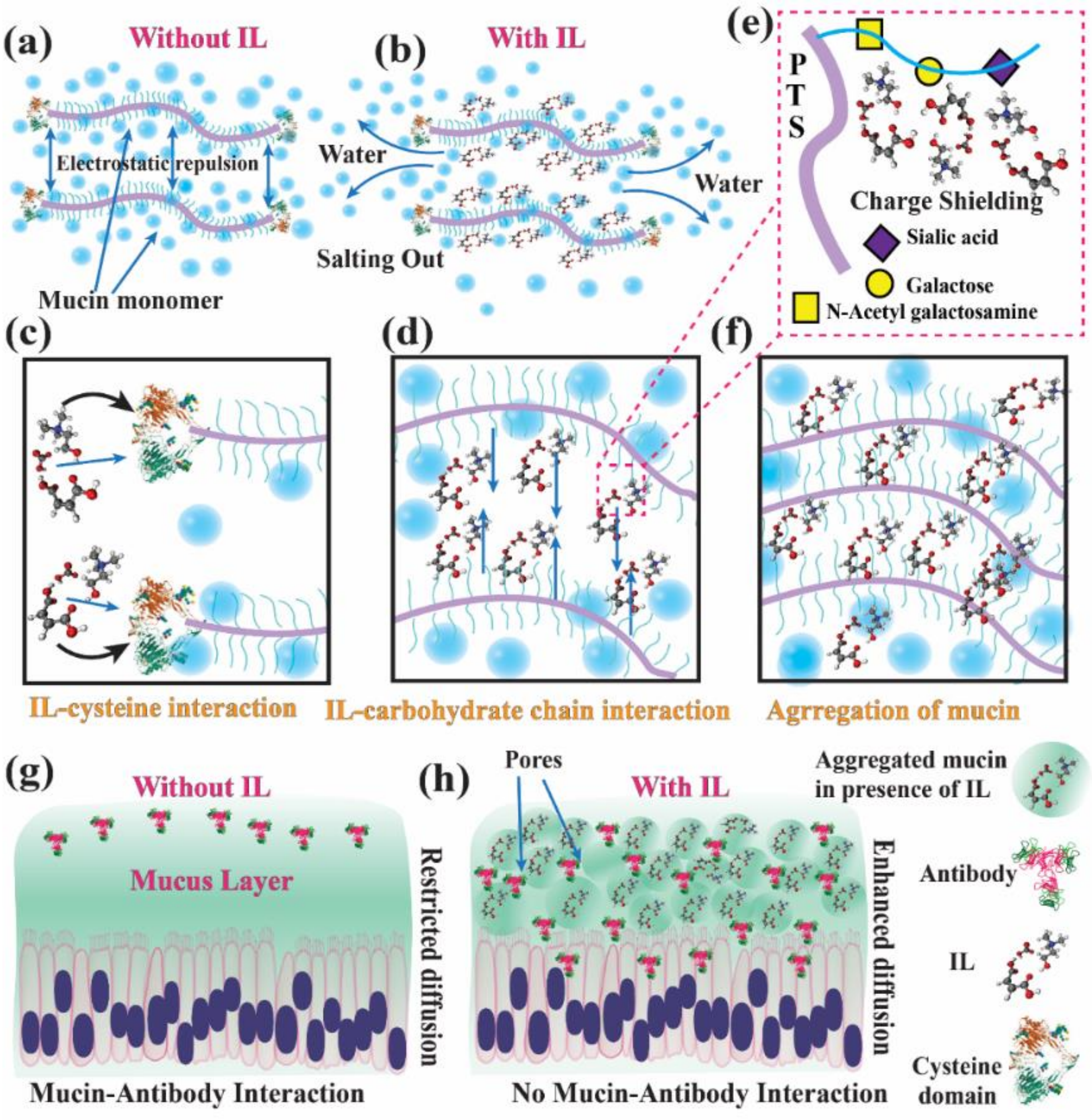

Figure 2. A schematic diagram of IL-mucin interaction resulted in enhanced diffusion of antibodies. (a) the homogenous structural arrangement of mucin monomers, (b) disruption of water mucin interaction in presence of IL, (c) IL complexation with cysteine domain of mucin resulted in disruption of chain elongation as well as mucin-nonmucin protein interaction, (d) Charge shielding of carbohydrate chains by IL, (e) Enlarged view of IL complexation with the carbohydrate chain components, (f) The overall interaction resulted in aggregation of mucin, (g) Restricted diffusion of antibodies through mucus layer without IL, and (h) Enhanced diffusion of antibodies through mucus layer in presence of IL.

4. Lactic Acid-Induced Colloidal Microrheology of Synovial Fluids

In chapter 4, we have studied the viscoelastic behavior of another important biofluid i.e. synovial fluid under lactic acid environments. As the lactic acid concentration is elevated in all arthritic conditions. We perform a detailed microrheological investigation on the effects of LA on the porcine SF. To determine the microrheology we have used diffusing wave spectroscopy (DWS) which provides the intensity autocorrelation function (ICF) and mean squared displacement (MSD) of the probed particles. Figure 1b shows the schematic diagram of DWS. The study has been performed directly under the microscope to uncover unique cross-linking phenomena of high MW proteins and HA in the SF in the presence of LA.

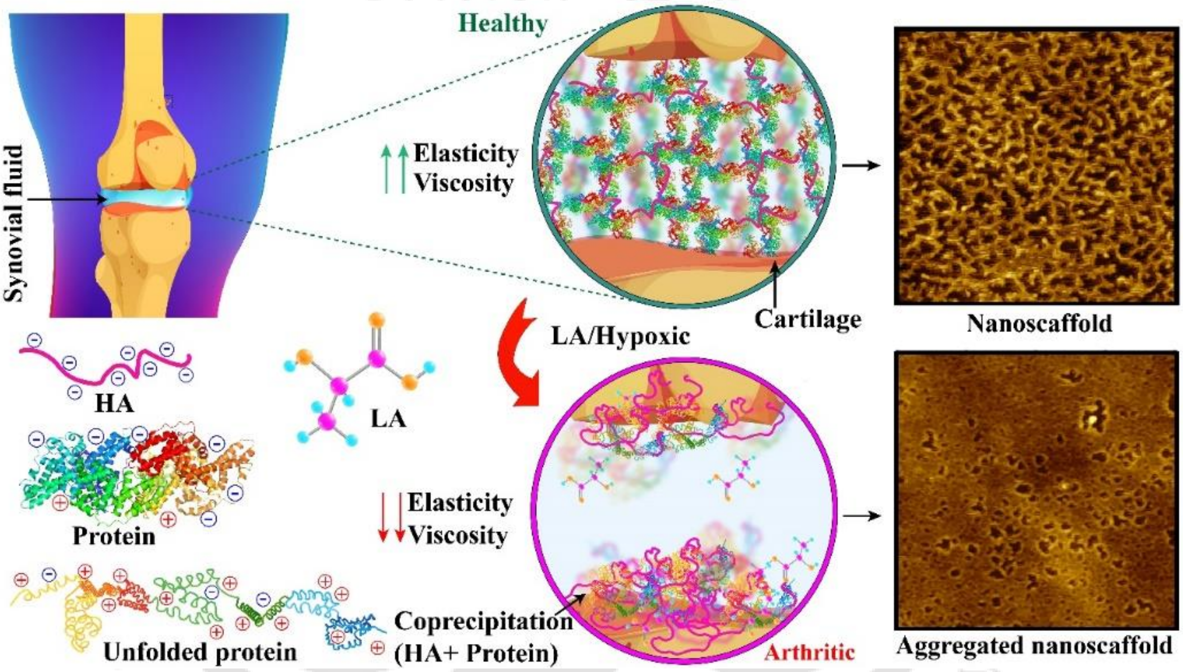

Figure 3. Schematic diagram of protein-HA interaction in the presence of lactic acid inside the synovium. In the presence of LA, Protein (albumin) unfolds and possesses net positively charged patches, which interact with net negatively charged HA and coprecipitates.

The study also uncovers the nature of the interaction between HA, LA, and albumin in SF with the help of a detailed ζ-potential, Circular Dichroism (CD), and fluorescence spectra analyses. All these characterizations help to connect the cross-linking of the SF phenomenon to the folding of albumin with increasing LA concentration in an SF, which can be a simple but major finding in future studies related to the microrheology of SF. The aforementioned phenomenon elucidates the interaction between albumin and HA in LA environments to simulate real-life arthritic conditions. Subsequently, this information helps us in the biosynthesis of a novel biomimetic therapeutic SF, which has properties similar to the real SF and can be suitable for arthritic treatments. The proposed artificial SF formulation consists of HA mixed with bovine Serum albumin (BSA) and γ-globulin, to engender microrheological properties such as viscosity, elasticity, and relaxation time resembling the natural SF. Overall, the results reported here will not only enable a much deeper insight into understanding the reasons behind the special properties of synovial fluid but also help in the synthesis of artificial SFs for future commercial use.

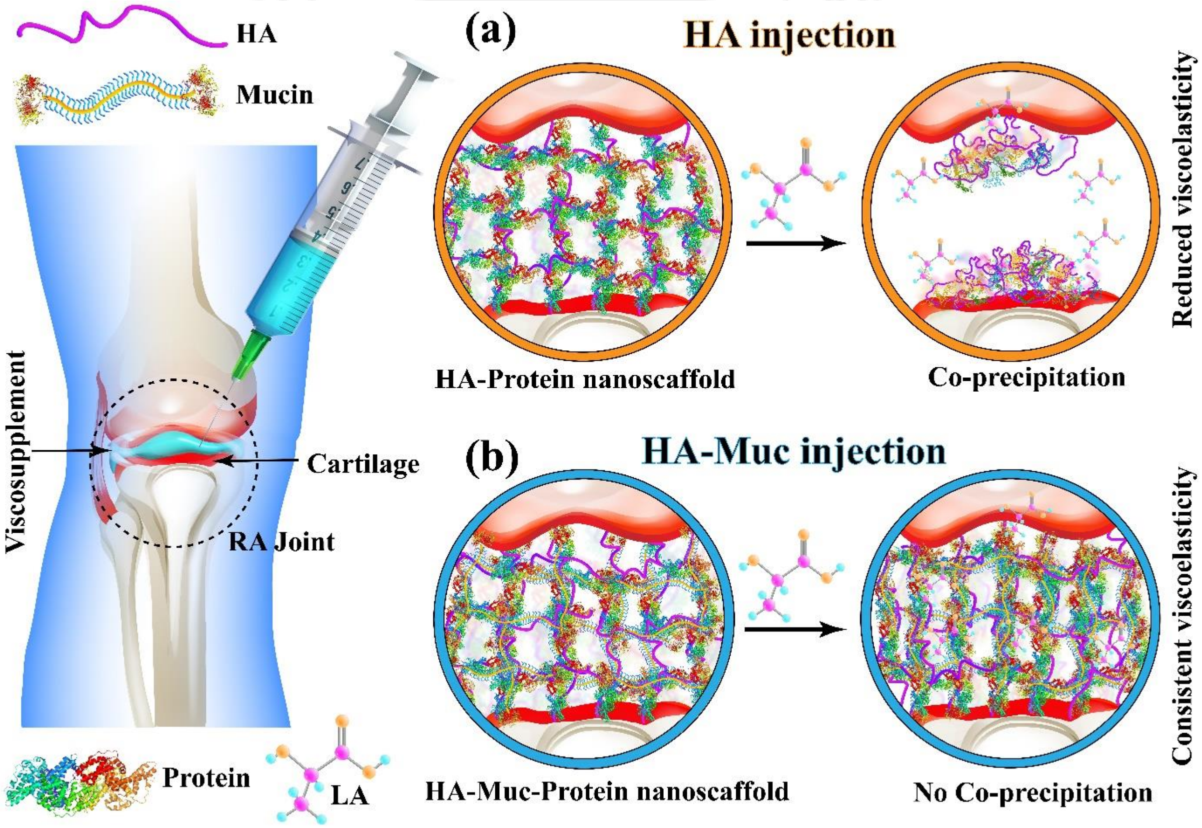

Figure 4. A schematic representation that depicts the behavior of the prepared HA and HA-Muc viscosupplements in a simulated rheumatoid arthritis (RA) joint. (a) In the presence of lactic acid, pristine HA co-precipitates with synovial proteins, compromising its function. (b) HA-Muc complex does not co-precipitate and retains its viscoelastic properties.

5. Designing an Articular Viscosupplement for Rheumatoid Arthritis Using Microrheological Analysis

In this chapter, we have explored the use of mucin in the hyaluronic acid system to prepare a novel viscosupplement. For this, we studied the microrheology of mucin-blended hyaluronic acid with a range of physiological pH conditions. In order to emulate the characteristics of normal and arthritic synovium, two model systems were prepared: one comprising synovial protein without lactic acid and the other including synovial protein with lactic acid. The synovial protein is prepared by mixing the albumin and γ- globulin in phosphate buffer saline. To elucidate the HA-Muc effects inside normal and arthritic synovium, microrheology of the HA-Muc complex is performed in the aforementioned two systems. Further, AFM is used to visualize the morphology of HA and HA-Muc complex. Furthermore, to know the microrheology near the interface between cartilage surface and viscosupplement, the multiple particle tracking technique is employed using confocal laser scanning microscopy.

6. Summary & Future Scopes

The major chapter-wise outcomes from the thesis can be summarized below. In Chapter 2, the results unveil that,

- Although the mucin molecules exist in the form of monomers or dimers due to a disulfide linkage in a solution, the overlapping of monomers and dimers leads to the formation of a weakly aggregated network at a higher concentration of mucin. Subsequently, the microrheological response of the solution goes from viscous to viscoelastic.
- Interestingly, the presence of other proteins such as albumin further facilitates such assembly of the mucins. For example, in such a scenario, the ITC analysis shown here confirms that albumin not only binds with the mucins but also tends to stabilize the physical crosslinking between the mucin domains to facilitate a higher-order assembly by forming additional links. As a result, enhancements in both viscous and elastic responses of the materials are observed, which can intuitively be correlated to the gel formation of the mucus in the lung airways due to the secretion of albumin in cysteine fibrosis and asthma diseases.
- Interestingly, the binding of BSA with mucin to form mucin-BSA complexes is found to be strongly dependent on the pH of the solution. For example, at a lower pH 3, the BSA molecules

do not bind with mucins owing to the repulsive force between the positive charge of BSA and positive residues of the binding site of the cysteine domain of mucin. This leads to a rheological response similar to that of pure mucin. However, the CD analysis of mucin and mucin-BSA samples at pH 7.4 shows that BSA not only binds with mucin but also alters its secondary structure.

- ❖ An AFM analysis reveals the presence of concatenated colloidal nano-network of the mucin-BSA complex. Concisely, the study highlights some of the very fundamental aspects of the interaction of the mucosal proteins with other non-mucin proteins such as albumin to highlight their importance in mucus gel formation to prevent the viral and bacterial penetration with the variation in the microrheology of the materials.

In Chapter 3, we find the following interesting outcomes,

- ❖ Mucin tends to aggregate in the presence of CBMA-based ionic liquid due to shielding of the negatively charged sialic acid residues of mucin monomer. This has been confirmed with the morphological characterization with AFM where the native structure of mucin has been altered.
- ❖ On the contrary in the presence of albumin, ionic liquid has increased the diffusivity of the probed particles due to the unwinding of mucin assembly tailored by the albumin. More precisely ionic liquid interferes with the electrostatic binding of mucin and albumin.
- ❖ Further, the DFT simulation study confirms that ionic liquid interacts with the sialic acid residue and neutralizes its negative charge. Moreover, ionic liquid also interacts with the binding sites of mucin which hinders the binding of mucin and albumin. From the DFT simulation study, the charge transfer (CT) process plays a significant role in participating in closed-range charged interactions among the IL-mucin components which is in the order of GalNAc (−0.084e) < sialic acid (−0.263e) < cysteine (−0.3e). Short and medium-range interactions were confirmed with the range of distances between IL-mucin components to be 1.52 to 2.2Å. The presence of multiple electrophilic and nucleophilic active sites within the

molecular groups present in the systems as displayed by the ESP charge analysis gave rise to electron cloud distribution and the evolution of H-bonding, electrostatic as well, and dispersion interactions that have been confirmed from the NCI/RDG analysis.

- The decisive selectivity of the IL interaction towards the principal mucin components (cysteine, GalNAc, and sialic acid) has been verified by a comparative analysis consisting of IL and charged amino acids (arginine and histidine

In Chapter 4, the study uncovers that

- The SF present inside the moving joints consists of an aqueous colloidal nano scaffold composed of hyaluronic acid and proteins, which eventually provides a viscoelastic nature to the same. The weak colloidal assemblage of such biomaterials in the aqueous medium provides unique load bearing (elasticity) and resistance to wear and tear (Non-Newtonian fluidity) capacities to the SF during the joint movements.
- Interestingly, the experiments also uncover that SF is found to lose its viscoelastic behavior in the presence of LA. The SDS-PAGE, gel-electrophoresis, and AFM studies together uncover that HA binds specifically with the high MW proteins of SF to co-precipitates in the presence of LA. The results are important from the perspective of anaerobic respiration in the synovium during hypoxic, arthritic, or excess workload conditions wherein LA is produced aplenty.
- The micro and bulk rheology experiments uncover that the destruction of the colloidal nano-scaffolds of the pig- and artificial SFs leads to a fluid with very little elasticity (low load-bearing capacity) and viscosity (fluidity of joints and resistance to wear and tear).
- The ζ-potential analysis reveals that BSA becomes positively charged when treated with a higher amount of LA to bind with a negatively charged HA to engender the phenomenon. Further, CD spectra of LA-treated BSA reveal that the LA-induced unfolding of BSA favors the electrostatic interaction with HA due to elevated exposures of charged amino acids.

In Chapter 5, the study shows that,

- The incorporation of mucin in hyaluronic acid solution changes its microstructure which has been reflected in the microrheological analysis. As the arthritic joints have elevated lactic acid, conventional hyaluronic acid injections might not be effective for joint lubrication particularly for rheumatoid arthritis condition.
- The blending of mucin in hyaluronic acid resists the lactic acid effects and maintains its viscoelasticity. Further, the multiple particle tracking microrheology near the cartilage surface reveals that the HA-Muc complex forms a less viscous layer near the cartilage surface compared to HA alone. This layer helps in boundary lubrication in high load conditions as well as facilitates joint movements without wear and tear of cartilage surfaces.

Future Scopes

The investigations in the present thesis explore various aspects of biomaterial research, which could be extended for future study. The future research scopes are enumerated as follows:

- Microrheology of mucin shown in the thesis can be studied with an actual human mucus-on-chip model.
- Design and development of mucus-modifying agents that could be useful for drug delivery as well as therapeutic purposes.
- Development of an effective therapeutic viscosupplement for complete remediation of all types of arthritis.
- Microrheology of tumor microenvironment for designing a tumor model for drug screening application.

List of Figures

List of Tables

Contents

Topic **Page No.**

CHAPTER 1

Introduction

Contents

1. Introduction

Rheology is the science of understanding the flow behavior of materials, derived from the Greek words "rheos" meaning "flow" and "logy" meaning "study,".[1–3] It encompasses the mechanical behavior of materials ranging from simple fluids like honey and glycerol to complex fluids such as mucus, blood, and tissues.[3] Rheology examines how materials respond to applied stress or strain, characterizing their properties based on flow behavior. Fluids can be classified into two types based on their flow characteristics— Newtonian and non-Newtonian. Newtonian fluids maintain a consistent viscosity over time, whereas non-Newtonian fluids exhibit viscosity that varies with external forces such as shear rates and shear stress.[4,5] Viscous fluids, which exhibit flow under stress, are typically Newtonian in nature, while solid materials that display elastic behavior are known as Hookean solids.[6] Materials that exhibit both viscous and elastic behavior are termed viscoelastic and are generally non-Newtonian in nature.[7,8] Rheology primarily addresses the flow behavior of non-Newtonian fluids.

As a branch of engineering, rheology focuses on the deformation and flow of materials and is particularly useful for measuring the viscous and elastic properties of materials with complex microstructures, including muds, sludges, suspensions, polymers, foods, body fluids, and other biological substances.[8] Biorheology is a specialized area within rheology that examines the relationship between the application of forces and the deformation and flow of biomaterials, including bones, soft tissues, synovial fluid, mucus, blood, and other biological substances.[9–12] This field also extends to the study of interactions between biological systems and non-biological materials.

Biorheology holds significant interest within the rapidly growing biotherapeutic industry, particularly in the development of stable protein-based formulations with controlled rheological responses.[13–16] Understanding, characterizing, and controlling the complex self-assembly and particle formation processes under various formulation conditions—such as pH, ionic strength, buffer salts, and temperature—are crucial for developing formulations that enhance stability, extend shelf life, and exhibit optimal rheological properties for specific applications. [17,18]

Early detection and characterization of protein particles or aggregates, including their size, structure, morphology, interactions, and rheology in therapeutic protein formulations, are critical for reducing safety issues (e.g., immunogenic responses in biologics) and ensuring stability and optimized delivery. Biorheology, which links the mechanical and structural characteristics of cells with their biochemical properties, is particularly promising in this regard. Based on the measurement methods, there are two types of rheology- Bulk-rheology and Microrheology. Bulk rheology tells us about a material's overall mechanical properties, while microrheology tells us about the rheology of a material at a micron level deals with the confined rheology of a material.[19–21] Bulk rheology is useful for developing food hydrocolloids, paints, lubricants, etc. However, microrheology is more useful in the biomedical sectors for the development of innovative materials for tissue engineering, medication formulations to fundamental studies. For instance, the mechanical behavior of complex biological fluids like cells, tissues, synovial fluid, blood, mucus, cerebrospinal fluids, and scaffolds could be studied via microrheological techniques.[22,23] In bulk rheology, a rheometer is employed where a revolving plate is moved over the sample on a flat plate. Conversely, in a typical microrheological measurements probe particles have been embedded in the sample and measured its movements over a period of time. Additionally, microrheolgy is a non-destructive technique with a small sample requirement.[19–21] Based on the measurement methods microrheology can be split into two categories—Passive microrheology and active microrheology. In passive microrheology, the thermal motion of probed particles is utilized. Conversely, for the active microrheology, an external field like a magnetic field, or optical tweezer is applied for the movements of investigated particles.[24] For passive microrheology, several approaches optical or scattering-based techniques are used. Optical approaches like multiple particle tracking (MPT) and video particle tracking (VPT) have been utilized to track probe particles using MATLAB or Python algorithms. On the other hand, Dynamic light scattering (DLS) and Diffusing wave spectroscopy (DWS) are based on the light scattering phenomenon of investigated particles.[25–28] Both the DLS and DWS approaches offer high-frequency rheology of material with ranges from 10^{-1} to 10^{5} for DLS and 10^{-1} to 10^{7} for DWS.[29] The advantage of optical-based approaches is the option to choose a particle location of interest for a sample. This is advantageous for microrheological research of cell nuclei or heterogenous tissue settings. However, passive microrheology is limited in the case of extremely stiffed-gelled materials as the Brownian movements are confined.[29] In such cases, active microrheology is advantageous which which uses external fields like magnetic or optical tweezers, is more effective.

Rheology has recently gained significant attention in the field of biology, particularly in the development of pharmaceutical drugs such as monoclonal antibodies, insulin, DNA vaccines, and hydrogels for drug delivery. Apart from conventional rheology, microrheology, especially has gained lots of interest due to its precise localized rheology with a small sample volume. This technology has shed light on the various fundamental problems in the domain of biology. This technique has enabled the measurements of the viscoelastic properties of various biofluids and helps in fundamental studies ranging from mucus behavior in cystic fibrosis to the mechanical properties of the tumor microenvironment.

In recent times mucus research has been accentuated in the arena of biophysical research. The mucus is a protective viscoelastic layer known as mucus is found in the human body throughout the gastrointestinal system.[30–33] This semi-gelled layer hydrates the eyes, nose, and oral cavity and acts as a selective filter in the small intestine by absorbing nutrients while protecting against pathogens. The thickened mucus in the stomach shields the epithelial lining from digestive acids. The viscoelastic properties of mucus vary depending on its location and the disease state. However, this mucus layer stands as a major barrier to the oral delivery of protein-based drugs as the mucin interacts with the drugs.[34] Therefore, the rheological analysis of mucus is crucial for understanding the disease progression as well as different treatment options for mucus-related diseases. Similarly, Synovial fluid, a biological lubricant found in the joints of vertebrates, plays a critical role in protecting cartilage surfaces and preventing bone-to-bone contact during movement.[35] It also nourishes synoviocytes and chondrocytes to maintain a healthy joint environment.[36,37] The unique viscoelasticity of synovial fluid is essential for joint lubrication; however, this property is compromised in arthritic conditions, leading to inflammation and joint stiffness.[38–41] In this scenario, the microrheological technique helps in understanding the assembly of the synovial fluids as well as the development of artificial synovial fluids for arthritic patients.

Another important application of microrheology is the understanding of the mechanical behavior of cells and their microenvironment. It has been reported that cancer cells exhibit distinct viscoelastic properties, enabling them to migrate through narrow blood capillaries to distant sites.[42–44] Additionally, the tumor microenvironment's viscoelastic behavior evolves as the tumor progresses, with metastatic tumors being stiffer than benign ones.[27,45,46] Therefore, microrheological studies can be crucial in understanding tumor progression as well as for drug screening purposes by mimicking the mechanical behavior of a tumor microenvironment. Furthermore, the microrheological technique has been used to design and develop scaffold material for tissue engineering and regenerative medicines.

In summary, microrheology has emerged as a powerful tool for measuring the mechanical properties of highly complex biomaterials which is unattainable with the usual Bulk-rheological techniques. The emergence of new technology in microrheological study leads to new discoveries and developments in biology and medicine.

1.1. Objectives of the Thesis

In view of the above background, the thesis utilizes the passive microrheology technique using DWS to understand the viscoelastic behavior of two biomaterials mucin and synovial fluid with a special emphasis on fundamentals and its applications. The objectives of the thesis are divided into four chapters followed by a conclusion and future scopes. A detailed list of publications has been provided at the end of the thesis. The objectives of the present work are as follows—

(i) **Microrheology of mucin-albumin assembly using diffusing wave spectroscopy**

In this chapter, DWS has been employed to study the microrheology of mucin in the presence of a non-mucin protein; albumin. Throughout this investigation, it has been observed that albumin enhances mucin assembly via electrostatic interaction and forms a compact network which might be useful for impeding the bacterial and viral pathogens.

(ii) **Microrheology of Ionic Liquid Doped Mucus for an Efficient Delivery of Protein-based Oral Drugs**

This chapter delved into the study of ionic liquid mucin interaction to effectively deliver a protein-based oral drug through the mucus layer. This study involves the changes in microrheology in the mucin ionic liquid system and mucin ionic liquid protein system. Later on, the mucus on a chip device is utilized to study the diffusion of antibodies in a simulated intestine environment.

(iii) Lactic acid-induced colloidal microrheology of synovial fluids

In this chapter, we have investigated the effects of lactic acid on the microrheology of synovial fluid. The study unveils that the elevated lactic acid concentration in the joint impacts the viscoelasticity of synovial fluid. The study shows that the unfolding of protein enhances the electrostatic interaction, resulting in the coprecipitation of major constituents, namely hyaluronic acid and albumin.

(iv) Designing an Articular Viscosupplement for Rheumatoid Arthritis Using Microrheological Analysis

This chapter delved into the formulation of a mucin-blended hyaluronic acid for lactic acid-elevated arthritic conditions. The study has shown that the incorporation of mucin in hyaluronic acid has come out to be better viscosupplement than hyaluronic acid alone special in the case of rheumatoid arthritis condition. Later on, the interfacial microrheology has been performed in between collagen surface and mucin blended hyaluronic acid through confocal microscopy technique. This study elucidates the interaction between the cartilage surface and the viscosupplement.

References

(1) Rudolph, N.; Osswald, T. *Polymer Rheology: Fundamentals and Applications*; 2015. https://doi.org/10.1007/978-1-56990-523-4.

(2) Feng, Y.; Taraban, M.; Yu, Y. The Effect of Ionic Strength on the Mechanical, Structural and Transport Properties of Peptide Hydrogels. *Soft Matter* **2012**, *8*, 11723–11731. https://doi.org/10.1039/C2SM26572A.

(3) Joyner, K.; Yang, S.; Duncan, G. A. Microrheology for Biomaterial Design. *APL Bioeng.* **2020**, *4* (4). https://doi.org/10.1063/5.0013707.

(4) Cross, M. M. Rheology of Viscoelastic Fluids: Elasticity Determination from

Tangential Stress Measurement. *J. Colloid Interface Sci.* **1968**, *27* (1), 84–90. https://doi.org/10.1016/0021-9797(68)90012-X.

(5) Alexander, D. E. Chapter 4 - Biological Materials Blur Boundaries. In *Nature's Machines*; Alexander, D. E., Ed.; Academic Press, 2017; pp 99–120. https://doi.org/https://doi.org/10.1016/B978-0-12-804404-9.00004-9.

(6) De Nardo, L.; Farè, S. 9 - Dynamico-Mechanical Characterization of Polymer Biomaterials. In *Characterization of Polymeric Biomaterials*; Tanzi, M. C., Farè, S., Eds.; Woodhead Publishing, 2017; pp 203–232. https://doi.org/https://doi.org/10.1016/B978-0-08-100737-2.00009-1.

(7) Zhou, J.; Papautsky, I. Viscoelastic Microfluidics: Progress and Challenges. *Microsystems Nanoeng.* **2020**, *6* (1), 113. https://doi.org/10.1038/s41378-020-00218-x.

(8) Zhang, M.; Zhang, W.; Wu, Z.; Shen, Y.; Wu, H.; Cheng, J.; Zhang, H.; Li, F.; Cai, W. Modulation of Viscoelastic Fluid Response to External Body Force. *Sci. Rep.* **2019**, *9* (1), 9402. https://doi.org/10.1038/s41598-019-45612-2.

(9) Hoppmann, W. H. 2nd. The Nature and Meaning of Biorheology. *Ann. N. Y. Acad. Sci.* **1966**, *130* (3), 873–879. https://doi.org/10.1111/j.1749-6632.1966.tb12631.x.

(10) Gupta, S.; Wang, W. S.; Vanapalli, S. A. Microfluidic Viscometers for Shear Rheology of Complex Fluids and Biofluids. *Biomicrofluidics* **2016**, *10* (4), 43402. https://doi.org/10.1063/1.4955123.

(11) Dimakopoulos, Y.; Giannokostas, K. From Biorheology to Biofluid Mechanics: Elucidating the Behavior of Biofluids in Complex Flows. *Sci. Talks* **2023**, *5*, 100139. https://doi.org/https://doi.org/10.1016/j.sctalk.2023.100139.

(12) Hollister, J. C. P.; Wang, A. C.; Kim, W.; Giza, C. C.; Prins, M. L.; Kavehpour, H. P. Shear Thinning Behavior of Cerebrospinal Fluid with Elevated Protein or Cellular Concentration. *Front. Phys.* **2023**, *11*. https://doi.org/10.3389/fphy.2023.1308136.

(13) Zarraga, I. E.; Taing, R.; Zarzar, J.; Luoma, J.; Hsiung, J.; Patel, A.; Lim, F. J. High Shear Rheology and Anisotropy in Concentrated Solutions of Monoclonal Antibodies. *J. Pharm. Sci.* **2013**, *102* (8), 2538–2549. https://doi.org/https://doi.org/10.1002/jps.23647.

(14) Lewis, C. M.; Heise, C. T.; Harasimiuk, N.; Tovey, J.; Lu, J. R.; Waigh, T. A. The Viscoelasticity of High Concentration Monoclonal Antibodies Using Particle Tracking Microrheology. *APL Bioeng.* **2024**, *8* (2), 26105. https://doi.org/10.1063/5.0201626.

(15) Acharya, P. C.; Suares, D.; Shetty, S.; Fernandes, C.; Tekade, R. K. Chapter 16 - Rheology and Its Implications on Performance of Liquid Dosage Forms. In *Dosage Form Design Considerations*; Tekade, R. K., Ed.; Advances in Pharmaceutical Product Development and Research; Academic Press, 2018; pp 549–597. https://doi.org/https://doi.org/10.1016/B978-0-12-814423-7.00016-2.

(16) Budai, L.; Budai, M.; Fülöpné Pápay, Z. E.; Vilimi, Z.; Antal, I. Rheological Considerations of Pharmaceutical Formulations: Focus on Viscoelasticity. *Gels*

2023, *9* (6). https://doi.org/10.3390/gels9060469.

(17) Sharma, V. K.; Patapoff, T. W.; Kabakoff, B.; Pai, S.; Hilario, E.; Zhang, B.; Li, C.; Borisov, O.; Kelley, R. F.; Chorny, I.; Zhou, J. Z.; Dill, K. A.; Swartz, T. E. In Silico Selection of Therapeutic Antibodies for Development: Viscosity, Clearance, and Chemical Stability. *Proc. Natl. Acad. Sci.* **2014**, *111* (52), 18601–18606. https://doi.org/10.1073/pnas.1421779112.

(18) Srivastava, A.; O'Dell, C.; Bolessa, E.; McLinden, S.; Fortin, L.; Deorkar, N. Viscosity Reduction and Stability Enhancement of Monoclonal Antibody Formulations Using Derivatives of Amino Acids. *J. Pharm. Sci.* **2022**, *111* (10), 2848–2856. https://doi.org/https://doi.org/10.1016/j.xphs.2022.05.011.

(19) Huck, B. C.; Hartwig, O.; Biehl, A.; Schwarzkopf, K.; Wagner, C.; Loretz, B.; Murgia, X.; Lehr, C.-M. Macro- and Microrheological Properties of Mucus Surrogates in Comparison to Native Intestinal and Pulmonary Mucus. *Biomacromolecules* **2019**, *20* (9), 3504–3512. https://doi.org/10.1021/acs.biomac.9b00780.

(20) Del Giudice, F.; Tassieri, M.; Oelschlaeger, C.; Shen, A. Q. When Microrheology, Bulk Rheology, and Microfluidics Meet: Broadband Rheology of Hydroxyethyl Cellulose Water Solutions. *Macromolecules* **2017**, *50* (7), 2951–2963. https://doi.org/10.1021/acs.macromol.6b02727.

(21) Samaniuk, J. R.; Vermant, J. Micro and Macrorheology at Fluid–Fluid Interfaces. *Soft Matter* **2014**, *10* (36), 7023–7033. https://doi.org/10.1039/C4SM00646A.

(22) Waigh, T. A. Microrheology of Complex Fluids. *Reports Prog. Phys.* **2005**, *68* (3), 685. https://doi.org/10.1088/0034-4885/68/3/R04.

(23) Weihs, D.; Mason, T. G.; Teitell, M. A. Bio-Microrheology: A Frontier in Microrheology. *Biophys. J.* **2006**, *91* (11), 4296–4305. https://doi.org/https://doi.org/10.1529/biophysj.106.081109.

(24) Wilson, L. G.; Poon, W. C. K. Small-World Rheology: An Introduction to Probe-Based Active Microrheology. *Phys. Chem. Chem. Phys.* **2011**, *13* (22), 10617–10630. https://doi.org/10.1039/C0CP01564D.

(25) Kakati, N.; Ahari, D.; Parmar, P. R.; Deshmukh, O. S.; Bandyopadhyay, D. Lactic Acid-Induced Colloidal Microrheology of Synovial Fluids. *ACS Biomater. Sci. Eng.* **2024**. https://doi.org/10.1021/acsbiomaterials.3c01846.

(26) Kakati, N.; Parashar, C. K.; Thakur, S.; Deshmukh, O. S.; Bandyopadhyay, D. Microrheology of Mucin–Albumin Assembly Using Diffusing Wave Spectroscopy. *ACS Appl. Bio Mater.* **2022**, *5* (9), 4118–4127. https://doi.org/10.1021/acsabm.2c00098.

(27) Krajina, B. A.; LeSavage, B. L.; Roth, J. G.; Zhu, A. W.; Cai, P. C.; Spakowitz, A. J.; Heilshorn, S. C. Microrheology Reveals Simultaneous Cell-Mediated Matrix Stiffening and Fluidization That Underlie Breast Cancer Invasion. *Sci. Adv.* **2021**, *7* (8). https://doi.org/10.1126/sciadv.abe1969.

(28) Krajina, B. A.; Tropini, C.; Zhu, A.; DiGiacomo, P.; Sonnenburg, J. L.; Heilshorn, S.

C.; Spakowitz, A. J. Dynamic Light Scattering Microrheology Reveals Multiscale Viscoelasticity of Polymer Gels and Precious Biological Materials. *ACS Cent. Sci.* **2017**, *3* (12), 1294–1303. https://doi.org/10.1021/acscentsci.7b00449.

(29) Mao, Y.; Nielsen, P.; Ali, J. Passive and Active Microrheology for Biomedical Systems. *Front. Bioeng. Biotechnol.* **2022**, *10*. https://doi.org/10.3389/fbioe.2022.916354.

(30) Mason', T. G.; Weitz', D. A. *Optical Measurements of Frequency-Dependent Linear Viscoelastic Moduli of Complex Fluids*; 1994; Vol. 74.

(31) Bansil, R.; Turner, B. S. The Biology of Mucus: Composition, Synthesis and Organization. *Adv. Drug Deliv. Rev.* **2018**, *124*, 3–15. https://doi.org/10.1016/j.addr.2017.09.023.

(32) McGuckin, M. A.; Thornton, D. J.; Whitsett, J. A. *Mucins and Mucus*, Fourth Edi.; Elsevier, 2015; Vol. 1–2. https://doi.org/10.1016/B978-0-12-415847-4.00014-8.

(33) Bansil, R.; Stanley, E.; Thomas LaMont, J. Mucin Biophysics. *Annu. Rev. Physiol.* **1995**, *57* (February), 635–657. https://doi.org/10.1146/annurev.ph.57.030195.003223.

(34) Banerjee, A.; Ibsen, K.; Brown, T.; Chen, R.; Agatemor, C.; Mitragotri, S. Ionic Liquids for Oral Insulin Delivery. *Proc. Natl. Acad. Sci.* **2018**, *115* (28), 7296–7301. https://doi.org/10.1073/pnas.1722338115.

(35) Schurz, J.; Ribitsch, V. Rheology of Synovial Fluid. *Biorheology* **1987**, *24*, 385–399. https://doi.org/10.3233/BIR-1987-24404.

(36) Zou, Y.; Zeng, S.; Huang, M.; Qiu, Q.; Xiao, Y.; Shi, M.; Zhan, Z.; Liang, L.; Yang, X.; Xu, H. Inhibition of 6-Phosphofructo-2-Kinase Suppresses Fibroblast-like Synoviocytes-Mediated Synovial Inflammation and Joint Destruction in Rheumatoid Arthritis. *Br. J. Pharmacol.* **2017**, *174* (9), 893–908. https://doi.org/10.1111/bph.13762.

(37) Garcia-Carbonell, R.; Divakaruni, A. S.; Lodi, A.; Vicente-Suarez, I.; Saha, A.; Cheroutre, H.; Boss, G. R.; Tiziani, S.; Murphy, A. N.; Guma, M. Critical Role of Glucose Metabolism in Rheumatoid Arthritis Fibroblast-like Synoviocytes. *Arthritis and Rheumatology*. 2016, pp 1614–1626. https://doi.org/10.1002/art.39608.

(38) Quiñonez-Flores, C. M.; González-Chávez, S. A.; Pacheco-Tena, C. Hypoxia and Its Implications in Rheumatoid Arthritis. *J. Biomed. Sci.* **2016**, *23* (1), 62. https://doi.org/10.1186/s12929-016-0281-0.

(39) Pucino, V.; Certo, M.; Bulusu, V.; Cucchi, D.; Goldmann, K.; Pontarini, E.; Haas, R.; Smith, J.; Headland, S. E.; Blighe, K.; Ruscica, M.; Humby, F.; Lewis, M. J.; Kamphorst, J. J.; Bombardieri, M.; Pitzalis, C.; Mauro, C. Lactate Buildup at the Site of Chronic Inflammation Promotes Disease by Inducing CD4+ T Cell Metabolic Rewiring. *Cell Metab.* **2019**, *30* (6), 1055-1074.e8. https://doi.org/https://doi.org/10.1016/j.cmet.2019.10.004.

(40) Anderson, J. R.; Phelan, M. M.; Clegg, P. D.; Peffers, M. J.; Rubio-Martinez, L. M. Synovial Fluid Metabolites Differentiate between Septic and Nonseptic Joint

Pathologies. *J. Proteome Res.* **2018**, *17* (8), 2735–2743. https://doi.org/10.1021/acs.jproteome.8b00190.

(41) Eugene Arthur, R.; Stern, M.; Galeazzi, M.; Baldassare, A. R.; Weiss, T. D.; Rogers, J. R.; Zuckner, J. Synovial Fluid Lactic Acid in Septic and Nonseptic Arthritis. *Arthritis Rheum.* **1983**, *26* (12), 1499–1505. https://doi.org/10.1002/art.1780261212.

(42) Onwudiwe, K.; Najera, J.; Holen, L.; Burchett, A. A.; Rodriguez, D.; Zarodniuk, M.; Siri, S.; Datta, M. Single-Cell Mechanical Analysis Reveals Viscoelastic Similarities between Normal and Neoplastic Brain Cells. *bioRxiv : the preprint server for biology*. United States September 2023. https://doi.org/10.1101/2023.09.23.559055.

(43) Hu, J.; Zhou, Y.; Obayemi, J. D.; Du, J.; Soboyejo, W. O. An Investigation of the Viscoelastic Properties and the Actin Cytoskeletal Structure of Triple Negative Breast Cancer Cells. *J. Mech. Behav. Biomed. Mater.* **2018**, *86*, 1–13. https://doi.org/https://doi.org/10.1016/j.jmbbm.2018.05.038.

(44) Mierke, C. T. Viscoelasticity Acts as a Marker for Tumor Extracellular Matrix Characteristics. *Front. cell Dev. Biol.* **2021**, *9*, 785138. https://doi.org/10.3389/fcell.2021.785138.

(45) Akinpelu, A.; Akinsipe, T.; Avila, L. A.; Arnold, R. D.; Mistriotis, P. The Impact of Tumor Microenvironment: Unraveling the Role of Physical Cues in Breast Cancer Progression. *Cancer Metastasis Rev.* **2024**, *43* (2), 823–844. https://doi.org/10.1007/s10555-024-10166-x.

(46) Nijenhuis, N.; Mizuno, D.; Spaan, J. A. E.; Schmidt, C. F. High-Resolution Microrheology in the Pericellular Matrix of Prostate Cancer Cells. *J. R. Soc. Interface* **2012**, *9* (73), 1733–1744. https://doi.org/10.1098/rsif.2011.0825.

CHAPTER 2

Microrheology of Mucin-Albumin Assembly using Diffusing Wave Spectroscopy

Contents

ABSTRACT

Mucus plays an important role in the protection of the epithelial cells from various pathogens or low pH environments apart from helping in the absorption of nutrients. Alteration of the rheology of the mucus layer leads to various diseased conditions such as cystic fibrosis, Crohn's disease and gastric ulcers, among others. Importantly, mucus consists of various mucins along with proteins such as immunoglobulin, lysozyme and albumin. In this Chapter, we explore the dependence of pH on the interactions between of bovine serum albumin (BSA) and porcine gastric mucins using diffusing wave spectroscopy (DWS). The study unveils that BSA actively binds with mucin to form mucin-BSA complexes, which is largely driven by the electrostatic interactions. Interestingly, such physical interactions significantly alter the microrheology of such biomaterials, which leads to the indicated by the reduction in the diffusivity of tracer particles in DWS. An array of DWS experiments suggest that, the interaction between mucin and BSA is highest in pH 7.4 on the contrary the interaction is minimum in pH 3 condition. Further analysis using atomic force microscopy uncover the formation of compact cross-linked colloidal network of mucin-BSA complexes at pH 7.4, which is the major reason behind the reduction in the diffusivity of the tracer particles in DWS. Furthermore, circular dichroism analysis reveals that the secondary structures of mucin-BSA complex are markedly different from the same of only mucin at pH 7.4. Importantly, such difference has not been observed at pH 3, which confirms that largely electrostatic interactions drive the formation of mucin-BSA complexes at neutral pH. In such a scenario, presence of Ca^{2+} ions are also found to facilitate bridging between BSA molecules, which is also reflected in the microrheology of the suspension of BSA-mucin complexes.

2.1. Introduction

Recent outbreak of the COVID pandemic has shown the crucial role of the rheological properties of the mucus layer in the lung linings during the onset and growth of various acute respiratory distress syndromes – ARDS.[1] The enhancement of viscous and elastic resistances in the mucus due to the macromolecular chain growth and cross-linking of protein matrices are found to restrict the ease of breathing through the lungs of the infected patients, often leading to the dreaded cystic fibrosis (CF) followed by edema.[2,3] For a healthy human, mucus is a harmless protective and moisturizing layer on the inner membranes of respiratory, digestive and urogenital organs. This slippery film is produced by the lining tissues and consists of inorganic salts, immunoglobulin, glycoproteins, lysozymes, and mucin.[4] The layer helps in the absorption of nutrients alongside preventing the attacks by various pathogens. However, during the viral or bacterial infections, the secreted globular proteins do bind with mucin and alter the rheological properties of the mucus to cause various respiratory disorders.[5] Thus, in order to achieve an in-depth fundamental understanding, it is of utmost importance to study the various rheological aspects of mucin and mucus layer with various protein or carbohydrate components amid varied surrounding conditions such as pH or temperature.

The key components of the mucus layer are different types mucins such as MUC2, MUC5AC, MUC5B, MUC6, and MUC19,[6] which are glycoproteins with ~80% carbohydrate and ~20% protein.[7] The carbohydrate chain includes N-acetyl-galactosamine, fructose, galactose and sialic acid, which are linked with PTS amino acid residues, namely proline, threonine and serine.[6] The terminal part of gel forming mucin is rich in cysteine residues,[8] which facilitates different types of chain propagation and cross-linking behaviors to alter the rheological properties and cause the diseased condition such as the CF in the respiratory disorders. On the other hand, a lower than normal viscosity of gastric mucus leads to ulcers,[9,10] which indicate the necessity of the maintenance of the appropriate rheology of mucin in the smooth functions of the various organs of the human body. In view of this background, herein we focus on the study of the rheology of a commercial type 2 mucin from porcine stomach under varied conditions.

It may be noted here that, in porcine stomach, two major gel forming proteins MUC5AC and MUC6 are found.[11–13] Importantly, since MUC5AC and MUC6 along with MUC2 and MUC5B genes are clustered from chromosome 11p15.5, they have high similarities in their molecular architechture.[13,9] In general, the MUC5AC gene is expressed on surface of epithelial tissues including the respiratory systems while MUC6 gene is expressed on glands of gastric mucosa.[13] It is now well established that an alteration of MUC5AC structure leads to the onset of CF.[14,15] Previous studies suggest that the structures of MUC5AC and MUC6 are very similar in N-termini, however, in the C-termini region MUC6 is much shorter than MUC5AC.[16]

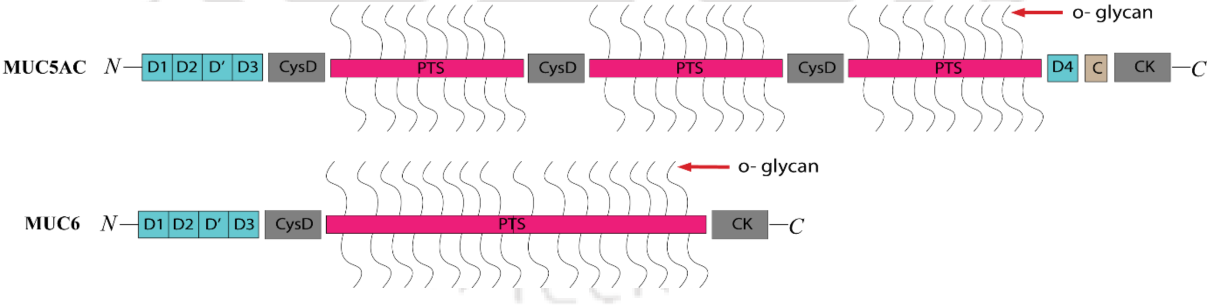

Figure 2.1. Domain organization of MUC5AC and MUC6.

Figure 2.1 schematically shows that the domains are arranged sequentially as D1, D2, $D^{/}$, D3 in the N-terminus followed by CysD and tandemly repeated PTS region, and at the C-terminus D4, C and cysteine knot (CK). After translation, primary sequence of mucin forms dimers at C-terminus in the endoplasmic reticulum (ER),[17] before it moves to the Golgi apparatus where its PTS domains are O-glycosylated to form a pair of mucin domains.

Thereafter, the glycosylated domain is trimerized in the D3 domain by di-sulfide bridges.[18] The secretary pathway of mucin, has different pH environments starting from pH 7 in the ER followed by pH 6 in Golgi complex and finally pH 5.2 in secretary granule. This helps in the polymerization of the mucin, which is followed by the packaging through the enhanced concentration of intragranular Ca^{2+}.[19]

In addition to the mucins, the crude mucus also consists of various non-mucin proteins such as albumin, keratin and other digestive enzymes.[20] They also possess several protein residues from microorganisms, antigen or antibodies. It has been found that such non-mucin proteins helps in assembly of mucin to form mucus.[20] Given their presence in the mucus with mucins, the exact role of non-mucin proteins in the assembly of mucins and their interactions with mucins at different ionic conditions is not very well understood. A very recent study has shown that the rheology of gastrointestinal mucus alters due to the formation of a complex hierarchical gel-like structure owing to the interactions between mucin glycoproteins, non-mucin proteins and Ca^{2+} ions. Importantly, the rheology of this system is also strongly dependent on the pH.[12] In the similar lines, a host of other studies have reported that presence of proteins such as lysozyme and immunoglobulins result in an increased viscosity of the mucus.[15] However, the effects of albumin on the mucosal rheology remains rather unclear. It may be noted here that albumin is the major constituent of mammalian blood serum,[21] most commonly found non-mucin protein in porcine intestinal mucus,[16] and plays an important role in maintaining blood pH and osmotic pressure apart from transporting various ligands and hormones.[22] Thus, it is important to study the microrheological variations of mucin in presence of albumin.

In this Chapter, we use diffusing wave spectroscopy (DWS), to investigate the microrheological characteristics over a wide range of frequencies (~10^{-1} to 10^{7} Hz) of mucin in presence of albumin, which is rather impossible for the conventional bulk rheological measurement techniques.[23–25] Such non-invasive measurements[26,27] unveil that indeed the interaction between the mucus proteins and albumin can significantly change the rheological properties, which may lead to a diseased condition beyond a critical limit. The study also provides the evidences related to the physical and electrostatic interaction in such systems with the help of isothermal titration calorimetry (ITC) to check the binding affinity of mucin and BSA. Further, the evidences on the formation of secondary structures of mucin-BSA complexes are unearthed with the help of circular dichroism (CD) experiments. The morphological changes during such interactions are also captured using high resolution atomic force microscopy (AFM). In a nutshell, the study unveils and establishes the possible interactions between the albumin and mucin protein in the mucosal layer, which may help in mucin gel assembly to protect the epithelial cells by inhibiting the penetration of bacterial and viral pathogens through the mucus layer.

2.2. Experimental Section

2.2.1. Materials

Mucin (98% pure) from porcine stomach was purchased from Sigma-Aldrich Pvt. Ltd. Bovine serum albumin (98% pure) was purchased from Sisco Research Laboratories Pvt. Ltd (SRL). The polystyrene tracer particle diameter of 510 nm (10%) was purchased from LS instruments AG, Switzerland. All the chemicals used without further purification. Milli-Q water was used in all experiments for preparing solutions.

2.2.2. Preparation of mucin–BSA complex

Mucin BSA complex were prepared by adding 30 mg/ml mucin in 2mg/ml BSA solution and allowed to mix gently in a shaker for 4 hours after that stored at 4°C. Solutions at pH

7.4 and pH 5.8 was prepared in 10 mM Phosphate buffer, while solutions at pH 3 was prepared using 10 mM sodium acetate buffer. A constant value of ionic strength was maintained for all the buffers to avoid any variations related to ionic strength of the buffers.[28] Subsequently 80 µl (10%) suspension containing the polystyrene tracer particles was added to the 920 µl of prepared solution and mixed thoroughly to be used as samples for DWS measurements. The tracer concentration was 0.8% for all the different groups, hence it did not affects the overall experimental results due to minimal dilution of sample. All the experiments have been performed thrice for precision and reproducibility of the data.

2.2.3. DWS Microrheology

The DWS measurements were performed by DWS RheoLab instrument, LS instruments AG, Switzerland. In all the experiments, we used 685 nm laser source and a 2 mm cuvette. The instrument has a Peltier unit, which controls the temperature of the cuvette chamber. **Figure 2.2** shows the instrumental diagram of the DWS. We have conducted all the experiments at 37ºC with 10 min of incubation time and turbidity index L/l* > 6, as mentioned in the DWS manual of LS instruments. It may be noted here that DWS is a light scattering technique to determine the microrheology of turbid samples.[29,30] In this technique, a high intensity laser light is incident on a square glass cuvette containing sample solution and tracer particles. The tracer particle inside the glass cuvette scatters the laser light and it gets detected by a photon detector.

The scattered laser intensity fluctuates with time due to Brownian motions of tracer particles and a correlator measures the autocorrelation function $\left[g_2(\tau)-1\right]$ to evaluate the ensemble averaged mean squared displacements (MSD) of the tracer particles, denoted as $\left\langle \Delta r^2(s) \right\rangle$.[31]

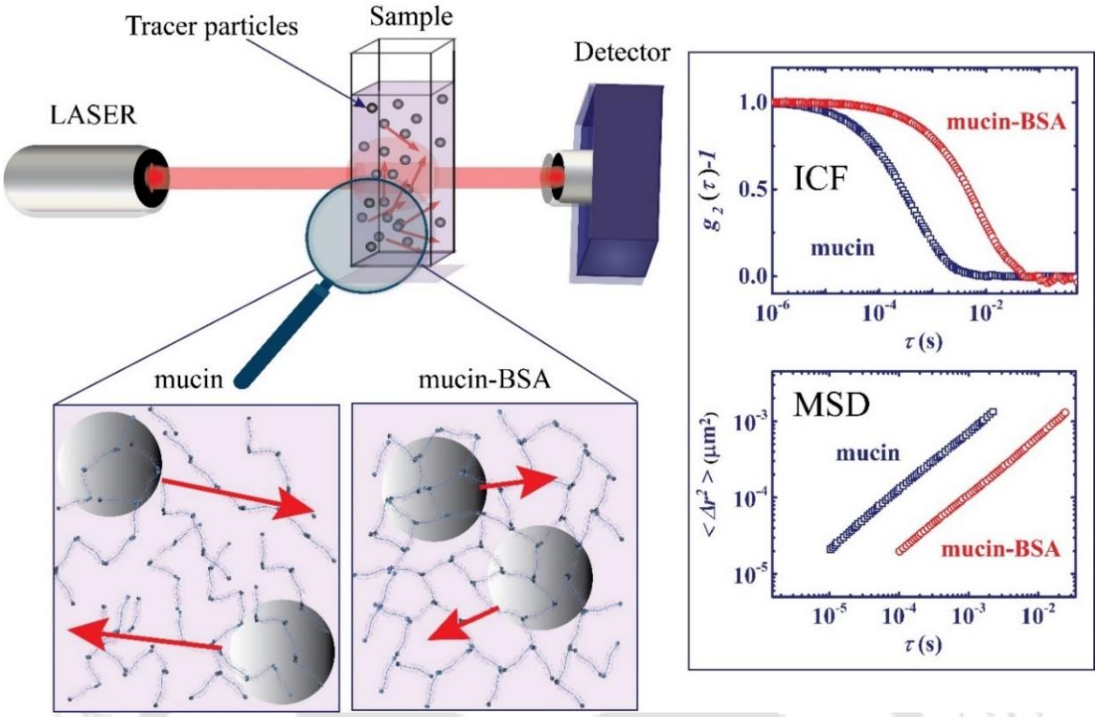

Figure 2.2. Schematic diagram of DWS instrumental setup. The graphs depict typical evolution of ICF as a function of lag time and the corresponding MSD as a function of lag time.

The relationship between the MSD and the lag time (τ) for a particle performing Brownian motion in a viscoelastic liquid is given as,

$$\langle \Delta r^2(\tau) \rangle = 2nD_t\tau^{\alpha}. \tag{1}$$

Where D_t is the time dependent diffusivity of the tracer particle and $0 < \alpha < 1$, n refers to the dimensionality (n =3 for a 3-dimensional analysis). For a tracer particle diffusing in a purely viscous environment, the exponent α = 1 and the diffusion coefficient D of the probe is inversely proportional to the viscosity (η) of the surrounding liquid. The viscoelastic modulus can be calculated from the MSD using the generalized Stokes- Einstein relation,[25,32] where $G(s)$ is the Laplace transform of the viscoelastic relaxation modulus $G(t)$, $\langle \Delta r^2(s) \rangle$ is the Laplace transform of the MSD, k_B is the Boltzmann constant, T is absolute temperature, a is radius of tracer particle. Replacing s with $i\omega$, we can get the complex modulus $\left(G^*(\omega)\right)$ and complex viscosity $\left(\eta^*(\omega) = G^*(\omega)/\omega\right)$.

$$G(s) = \frac{k_B T}{\pi a s \langle \Delta r^2(s) \rangle}. \tag{2}$$

2.2.4. Isothermal Titration Calorimetry (ITC)

MicroCal iTC 200, GE Healthcare instrument was used to study the binding affinity of mucin and BSA. About 20 micromolar of mucin was placed in the sample cell of calorimeter. 2000 micromolar of bovine serum albumin was loaded into the syringe and titration was carried out for 20 injections at 37˚C. Both the samples were prepared in 10mM phosphate buffer at pH 7.4. Another titration was carried out between mucin and buffer for heat values produced from the buffer or the mucin. The raw data were analyzed with origin7 software (Origin Lab,USA) and fitted with sequential site binding model for final analysis.

2.2.5. ζ-potential measurements

ζ-potential measurements were performed using Litesizer 500 instrument from Anton Paar, for mucin, BSA and mucin-BSA samples at pH 7.4, pH 5.8 and pH 3. Prior to measurements samples were diluted 100 times. All the measurements were performed in triplcates and mean data was used for the analysis.

2.2.6. Circular Dichroism analysis (CD)

UV-CD (JASCO, J-1500) analysis was done for determination of secondary structure of mucin, BSA and mucin BSA complex. Samples were taken in a quartz cuvette with a pathlength of 2 mm. All the Measurements were done with the average of 3 accumulations and the scanning range of 260–190 nm with a scanning speed of 100 nm/min, 0.1 nm of bandwidth. Prior to the measurements, a buffer sample was used for baseline correction.

2.2.7. Morphology analysis by AFM

AFM (Cypher asylum, Oxford) was used to observe the morphology of mucin and mucin BSA complex. For this, the samples were diluted to 100 times and drop casted on a silicon wafer of size 5 mm × 8 mm. After that, it was allowed to dry for 5 min then washed with milli-Q water and allowed to dry overnight in a vacuum desiccator. The scan rate was kept 1to 2 Hz and the set point was around 500 mV. Comparative analysis was performed for scan areas of 2 μm^2 and 5 μm^2 for both mucin and mucin-BSA complex.

2.3. Results and Discussion

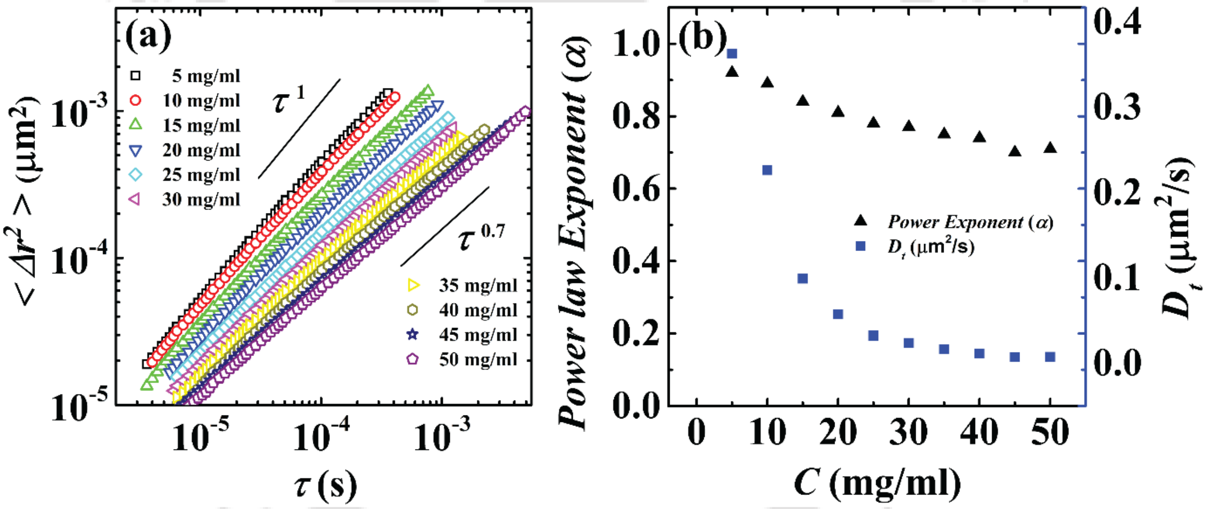

Figure 2.3. Microrheology of mucin (a) MSD of tracer particles embedded in 5 ≤ *C* ≤50 mg/ml mucin. From low to high concentration, a log-log scaling of τ^1 to $\tau^{0.7}$ has been observed, which indicates the transition from diffusive to sub-diffusive behavior. (b) Power law behavior is observed in the concentration range 5 ≤ *C* ≤50 mg/ml at $\tau = 10^{-4}$ s. *Power law exponent (α)* in left *y*-axis and *diffusivity* (D_t) plot in right *y*-axis have been varied with the concentration (*C*) in *x*-axis. Power law exponent and diffusivity does not change much after 25 mg/ml.

To begin with, we study the rheological behavior of mucin solution as a function of its concentration. **Figure 2.3a** shows the mean square displacement (MSD – Δr^2) vs. lag time (τ) data, which is a signature of the motions of the probe particles in presence of the mucin matrices. The relationship between MSD and τ is given previously by the equation (1). The plot suggests that the exponent α progressively shifts from ~ 1 at low mucin concentrations ($C < 10$ mg/ml) to ~ 0.7 at the higher mucin concentrations ($C > 25$ mg/ml). The shift reflects the change in the rheological behavior of the sample from purely viscous at a lower concentration to viscoelastic at a higher concentration. At the lower mucin loading, the rheological response of the solution is governed purely by the intermolecular hydrodynamic interactions between the mucin molecules alongside the deformation of the individual mucin molecules. However, as the concentration increases, the polymeric chains tend to overlap, interacting physically, or crosslinking, which eventually gives rise to the viscoelastic response.[33] In such a scenario, the motion of the tracer particles transform from diffusive to sub-diffusive as they are trapped inside the entangled macromolecules. Subsequently, as the plots in the **Figure 2.3b** suggests, a progressive reduction in α and diffusivity (D_t) is observed with increasing C. The plots also suggest that, at a significantly higher concentration, both the parameters saturate to a constant value indicating the possible limits of such interactions. This might be because of excluded volume effect of high concentrations of mucin polymers as well as high repulsion between negatively charged carbohydrate chains between mucin molecules.

In order to probe the effect of BSA on the assembly of mucins, we study the microrheology of 30 mg/ml of mucin in presence of BSA with concentrations, C_B, ranging from 2 mg/ml to 10 mg/ml shown in **Figure 2.4**. The choice of mucin concentration and the range of BSA concentrations has been made keeping in mind the actual physiological concentrations found in the mucus.[34–36]

Figure 2.4a shows that the addition of BSA to the mucin solution increases the decay time, which is also reflected in MSD vs. τ plot. Further, the MSD vs. τ plots for both the

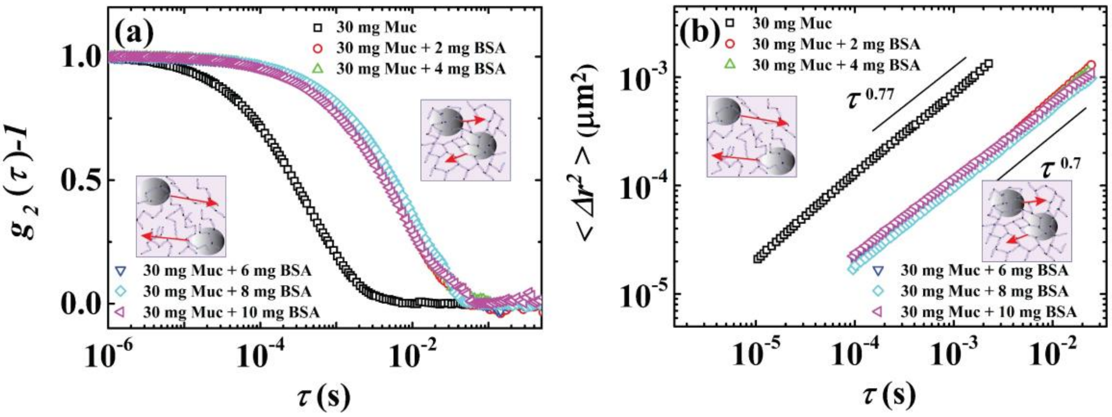

Figure 2.4. Microrheology of mucin treated with different concentrations of BSA (a) ICF of 30 mg/ml mucin with BSA concentration $2 \le C_B \le 10$ mg/mL. mucin with BSA decays slowly compared to mucin alone. It has been observed the change in ICF decay is independent of BSA concentration after 2 mg/ml, (b) MSD of tracer particles embedded in 30 mg/ml mucin with BSA concentration $2 \le C_B \le 10$ mg/mL. The MSD of tracer particles in mucin with BSA is lower than the mucin alone. There is a marginal change in power law exponent for mucin with BSA. However, the increasing concentration of BSA does not affect the MSD and power law exponent.

mucin and the mucin-BSA complex solutions exhibit a similar power law behavior as shown in **Figure 2.4b**.However, the dynamics of tracer particles in mucin-BSA solutions are found to be much slower as compared to those in pure mucin solutions. The results point to the fact that the non-mucin proteins tend to stabilize the physical crosslinking between mucin domains which in turn facilitate a higher order assembly by forming additional links either through electrostatic interaction or by forming the hydrogen bonds and disulfide bridges.[20,37] Importantly, the binding of such non-mucin proteins with mucins is also dependent on the entanglement of mucins. For example, we observe that for a mucin concentration of 30 mg/ml, a very small concentration of BSA (~2 mg/ml) is sufficient to saturate all the binding sites. Any further addition of BSA has marginal effect on the microstructure and hence on the microrheology of the mucin-BSA complexes.

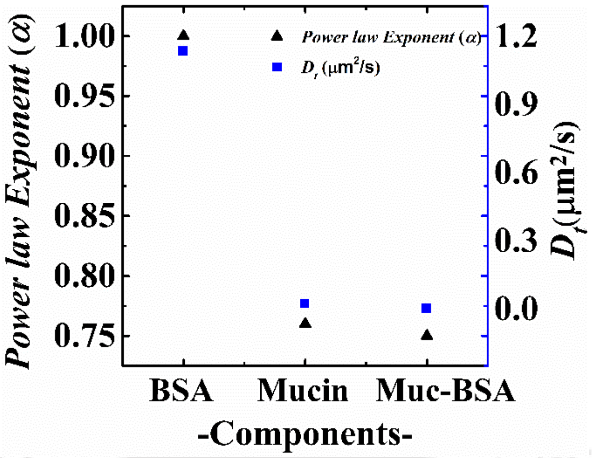

Figure 2.5. Comparison of *diffusion coefficient* D_t (in right *y*-axis) and *Power law exponent* (in left y-axis) of 30 mg/ml mucin, 2 mg/ml BSA and mucin-BSA complex (30mg/ml mucin + 2 mg/ml BSA) at 10^{-4} s. Diffusivity of tracer in BSA is much higher and similar to water. The tracer particles embedded in mucin BSA shows lower diffusivity compared to pristine mucin. *Power law exponent* for BSA is 1 and for mucin and mucin-BSA complex is 0.76 and 0.75, respectively.

In order to compare the microrheological response of pure mucin, pure BSA and mucin-BSA solutions, α and D_t at a time $\tau = 10^{-4}$ s from the MSD vs. τ curves are summarized in the **Figure 2.5**. In this situation, we observe that, owing to the small size of its molecules and low concentrations, the BSA solution exhibits a purely viscous response, $\alpha = 1$ and D_t similar to the one predicted by the Stokes-Einstein relation. On the other hand, the mucin and mucin-BSA complex have much lower values of α and D_t as compared to BSA. For example, α for mucin and mucin-BSA solutions are found to be ~0.76 and ~0.75 and D_t for mucin-BSA is ~0.02 μm²/s, which is much lower than the same for mucin, ~0.15 μm²/s.

Following this, isothermal titration calorimetry (ITC) has been performed to elucidate the binding affinity of mucin and BSA at 37℃. **Figure 2.5** shows the ITC thermogram where BSA is titrated with mucin in 10 mM phosphate buffer at pH 7.4. Subsequently, the ITC data has been fitted with two site sequential binding model, which signifies the multiple ligand binding sites that are independent or cooperative. Here we have observed that binding affinity of K_1 is much higher than the binding affinity of K_2, which indicates that initial binding event does not affect the secondary binding event. We have only considered K_1 as the binding constant. **Table 2.1** shows the thermodynamic parameters extracted by fitting the thermogram to a two-site sequential binding model. It shows that BSA exothermically binds with mucin with the ΔH value of $-4.386 \times 10^4 \pm 3.79 \times 10^3$ cal/mol and there is no binding affinity towards the solvent i.e. 10 mM Phosphate buffer at pH 7.4.

Table 2.1. Thermodynamic parameters of mucin and BSA interaction obtained from ITC.

K (M^{-1})	ΔH (cal/M)	ΔS (cal/mol/deg)
$1.26 \times 10^5 \pm 3.6\ 10^4$	$-4.386 \times 10^4 \pm 3.79 \times 10^3$	-118

In order to analyze the nature of the interactions between mucin and BSA, the microrheology of mucin and mucin-BSA complex have been analyzed for the pH values of 7.4, pH 5.8 and pH 3 at 37°C. **Figures 2.7a**, **2.7c** and **2.7e** show MSD vs. τ and the complex viscosity (η^*) vs. frequency (ω) and elastic modulus (G_1), loss modulus (G_2) vs. frequency (ω), for pure mucin solutions and **Figures 2.7b**, **2.7d** and **2.7f** shows the same results for mucin-BSA solution. The shift can be attributed to the increase in the crosslinks between mucin molecules due to less repulsion in between the negatively charged carbohydrate chains of two mucin molecules.[38] However, as the pH is lowered to 3, BSA molecules becomes positively charged which is above the isoelectric point (IEP) of BSA, [39,40] the BSA molecules no longer bind to the mucin molecules. Thus, the viscoelastic network of mucin-BSA complexes no longer exists at pH 3 and the microrheological response is instead driven by the weak hydrophobic interactions between the mucin molecules.

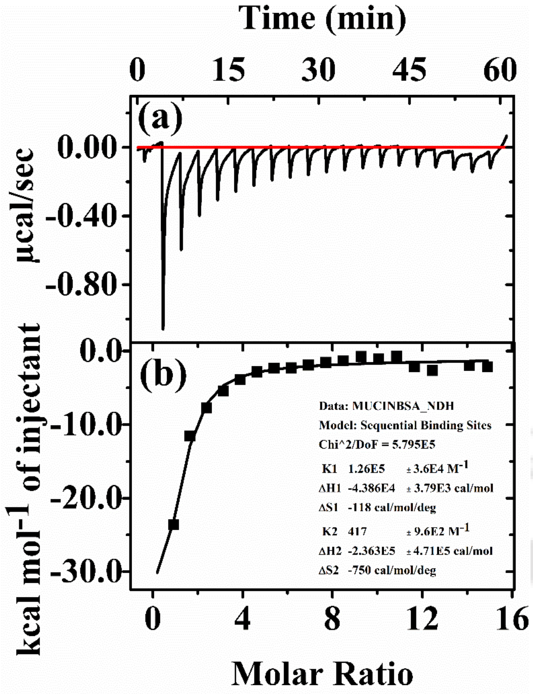

Figure 2.6. ITC profile of mucin and BSA, (a) shows the raw data and (b) shows the binding isotherm created by plotting the integrated heat peaks from the raw data against the molar ratio of BSA. The solid line is a best fit of a two-site sequential binding model.

Subsequently, the MSD curves at pH 3 are shifted to shorter timescales, which also reflects in lower $\eta^*(\omega)$ as well as G_1 and G_2. Upon a closer inspection, one can easily observe that the rheological response of mucin-BSA solution at pH 3 is very similar to that of a pure mucin solution at pH 3. The results shown highlight the role of BSA in stabilizing the physical crosslinking between mucin molecules when it is present in the solution and allowed to bind with mucin.

The effect of pH on the interactions of the protein matrices are further corroborated by the ζ-potential measurements of mucin, BSA and mucin-BSA solutions at different pH of 7.4, 5.8 and 3, as shown in **Table 2.2**. The table shows that, at pH 7.4, mucin, BSA and mucin-BSA solutions have ζ-potentials of –21.9, –18.2 and –22.8 mV, respectively. Thus, mucin and BSA have an effective negative charge at neutral pH. However, the DWS experiments suggest a higher degree of interactions between mucin and BSA matrices under such circumstances.

Table 2.2. ζ-potential of mucin, BSA and mucin-BSA complex at pH 7.4, pH 5.8 and pH 3 with or without Ca^{2+}

pH	ζ-potential (mV)					
	Mucin	**Mucin-Ca^{2+}**	**BSA**	**BSA-Ca^{2+}**	**Mucin-BSA**	**Mucin-BSA -Ca^{2+}**
7.4	−21.9 ± 1.33	−12.3± 2.05	−18.2 ± 0.6	−12.5± 0.5	−22.8 ± 1.1	−12.2± 1.9
5.8	−15 ± 0.38	−7.1 ± 1.99	−9.16 ± 0.85	−6.5 ± 1.93	−13.56 ± 2.33	−8.11 ± 1.74
3	−3.33 ±0.05	−1.8± 0.35	+3.83 ± 1.42	+5.1± 1.25	−3 ± 0.4	−0.08± 0.01

Such interactions and associations can be explained from the presence of the positively charged cysteine domains in the mucin matrices (**Figure 2.1**), which is already established in the literature.[29,35,41,42] The experiments suggest that the BSA matrices with an effective negative ζ-potential are attracted towards these positively charged cysteine domain residues of mucin to increase the viscosity of the solution. In case of pH 5.8, the effective ζ-potential of BSA remained negative, however, reduced by half of its magnitude. Thus, it can be anticipated that the interaction between mucin-BSA is still there as evidenced by similar MSD behavior, as compared to the same at the pH 7.4. As the pH is lowered further to 3, which is very close to the IEPs of mucin[43] and BSA,[39,40] the mucin still have an effective negative charge of −3.33 mV while BSA has a ζ-potential of 3.83 mV. In such a scenario, the BSA is unable to bind with the positively charged cysteine residues of the mucin matrix. As the ζ-potential of mucin-BSA complex is also near to its IEP, and absence of interaction indicates possibilities of absence of hydrophobic interactions. This explanation is in contrast to a recent study where it has been demonstrated that at the IEP of humic acid-lysozyme complex, the aggregation has been the highest due to hydrophobic interactions.[44]

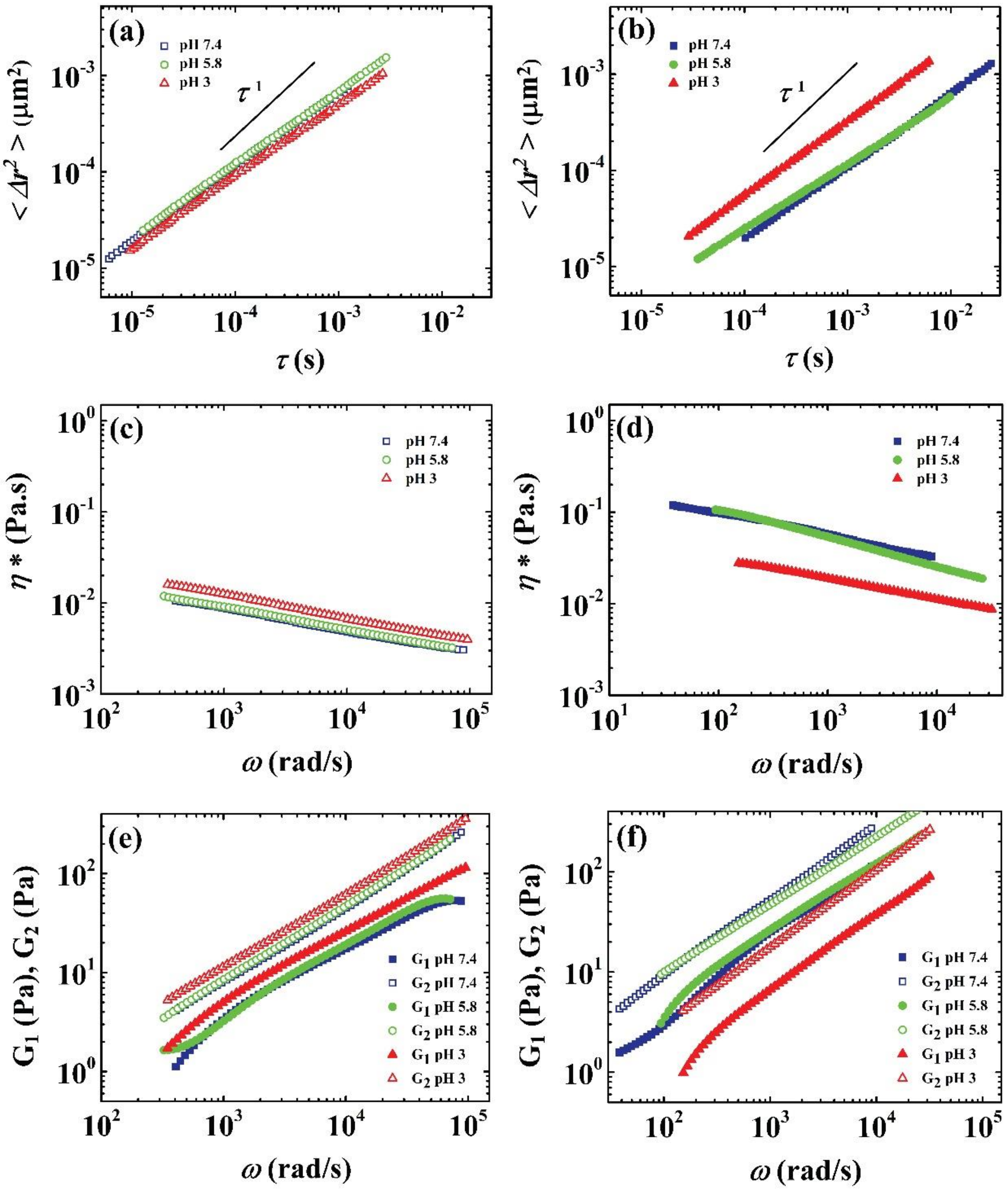

Figure 2.7. Effects of pH on the microrheology of mucin and mucin-BSA complex. All the experiments have been carried out in 3 different pH conditions pH 7.4, pH 5.8 and pH 3. (a) MSD of 30 mg/ml mucin. A marginal decrease in MSD is observed with decreasing pH. (b) MSD of mucin-BSA complex (30 mg/ml mucin + 2 mg/ml BSA) wherein MSD increases with decreasing pH. (c) Complex viscosity (η^*) of 30 mg/ml mucin increases at lower pH. (d) Complex viscosities (η^*) of mucin-BSA complex (30 mg/ml mucin + 2 mg/ml BSA) decreases at the low pH condition. (e) Elastic modulus (G_1) and loss modulus (G_2) of 30 mg/ml mucin increases with decreasing pH. (f) Elastic modulus (G_1) and loss modulus (G_2) of mucin-BSA complex (30 mg/ml mucin + 2 mg/ml BSA) decreases at low pH condition.

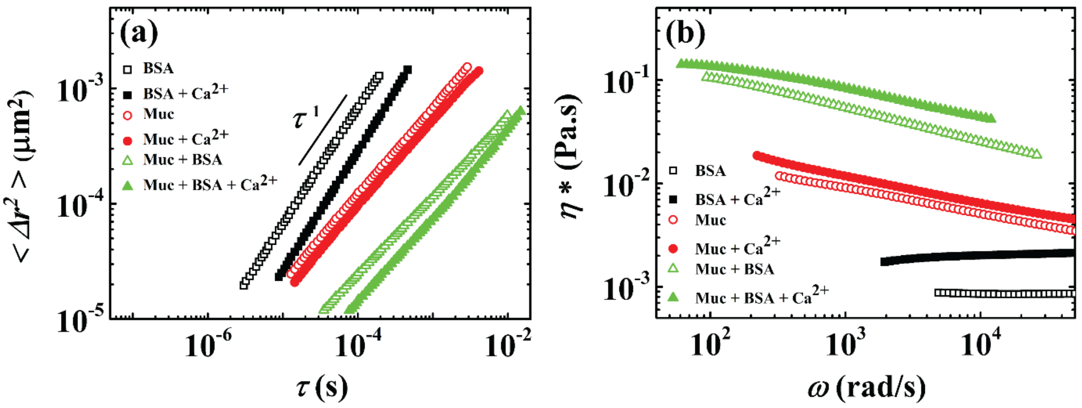

Figure 2.8. Effects of 10mM Ca^{2+} on BSA, mucin and mucin-BSA complex (a) Comparison of MSD of tracer particles in Ca^{2+} treated and untreated BSA, mucin and mucin-BSA complex samples. Treatment with Ca^{2+} decreases the MSD of both BSA and mucin-BSA complex, whereas for mucin Ca^{2+} has very little or no effects, (b) Comparison of complex viscosity of Ca^{2+} treated and untreated BSA, mucin and mucin-BSA complex. Treatment with Ca^{2+} increases the complex viscosity of BSA, mucin and mucin-BSA complex.

In the mucus layer there is an increased concentrations of Ca^{2+} ions which are secreted in goblet cells, facilitating mucin packing by neutralizing the negative charges of sialic acids on the mucin backbone. However, the role of Ca^{2+} in influencing interactions between mucin and non-mucin proteins was previously unclear. In order to elucidate whether the Ca^{2+} has a role in facilitating the binding of mucin with BSA, we performed the microrheology of 30 mg/ml mucin, 2mg/ml BSA and mixture of both i.e 30 mg/ml mucin and 2 mg/ml BSA with or without the presence of 10 mM $CaCl_2.2H_2O$ in 10mM phosphate buffer at pH 5.8. We have observed that there is a decrease in magnitudes of MSD for Ca^{2+} treated both BSA and mucin BSA samples compared to untreated samples, as shown in **Figure 2.8a**. However, this change in MSD for mucin sample is less. This is also evident in complex viscosity plot, where there is an increase in the complex viscosity for the case with the Ca^{2+} treated BSA and mucin-BSA samples, as shown in **Figure 2.8b**. Further, the **Table 2.2** suggests that there is a reduction in the ζ-potentials of mucin, BSA and mucin-BSA complex after the addition of Ca^{2+} at all pH. However, it is evident that, although in case of the mucin samples, the ζ-potential reduces in presence of the Ca ions, the microrheology remains similar to the samples without Ca ions. However, the variation in the microrheology of both BSA and mucin-BSA in presence of the Ca ions can be attributed to the diminishing double layer between the molecules, which eventually results in a reduction in the MSD and increase in the viscosity. Such interactions of Ca^{2+} with molecules with negative surface charge has also been observed wherein humic acid aggregation takes place in the presence of Ca ions.[45]

In case of mucin-BSA solution Ca^{2+} aids more BSA to the cysteine domain of mucin, which further enhances the mucin assembly. Thus, Ca^{2+} ions are found to aid the formation of a viscoelastic network by formation of links between non-mucin proteins that are attached to mucins.[46] In absence of Ca^{2+} ions, the network formation relies on hydrogen bonding between the non-mucin proteins, which results in a weakly aggregated network. In presence of Ca^{2+} ions however, both the mechanisms synergistically contribute to the formation of the network with the Ca^{2+} mediated links being the dominant factor.[20] It is important to note here that the Ca^{2+} ions interact majorly via the BSA molecules. Thus, the presence of even a small concentration of Ca^{2+} ions, leads to a noticeable change in both MSD and $\eta^*(\omega)$ values of pure BSA solution as well as mucin-BSA solution. In comparison, pure mucin solution shows little or no effect of addition of Ca^{2+} ions. In such a scenario, whatever minor change occurs can be attributed to the marginally increased overlapping of the mucin molecules due to the screening of their negative charge by the positively charged Ca^{2+} ions.

Figures 2.9a-b show the AFM analysis for mucin in 5×5 μm^2 and 2×2 μm^2 area, which depicts the concatenated thread like micro/nano patterns all over the area. The results observed in the AFM further support the claim that the microstructure comprises of mucin molecules physically overlapping and interacting via weak hydrophobic interactions. This kind of weakly assembled network allows faster dynamics of tracer particles while the overall translation of the tracer particles remains sub-diffusive.

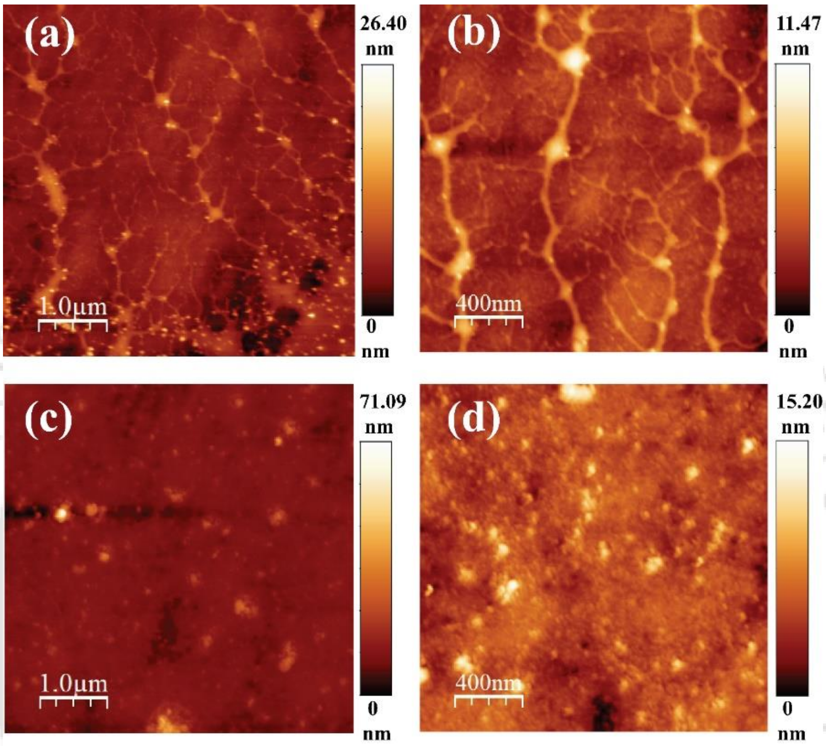

Figure 2.9. Morphology of mucin studied by AFM (a) 5×5 μm ^{2} field, (b) 2×2 μm ^{2} field, and Mucin BSA complex (c) 5×5 μm ^{2} field, (d) 2×2 μm ^{2} field.

On the contrary, AFM analysis of mucin-BSA complex (**Figures 2.9c-d**) shows cluster of smaller structures in the lateral dimension, which tends to increase the topography (height) of the sample. This signifies a more compact and rigid network formed by cross linked mucin molecules stabilized by the presence of BSA. Such a clustered micro-environment leads to a slow-down in the dynamics of tracer particles while the translation of the particles is sub-diffusive.

The CD spectra of 0.02 mg/ml of BSA, 0.3 mg/ml of mucin and the 0.3mg/ml mucin with 0.02 mg/ml BSA have been recorded at 37°C with two pH conditions pH 7.4 and pH

3. At both the pH conditions, BSA spectra is similar with a slight decrease in ellipticity in case of pH 3. A characteristic α-helix negative peak at 208 nm and 222 nm is present in both cases, as shown in **Figure 2.10a**. The plots suggest that the secondary structure of BSA is the same at pH 3 as well as at pH 7.4 with some unfolding structure.[47,48] Mucin at pH 7.4 and pH 3 show a typical negative ellipticity from 200 to 205 nm, which suggests a random secondary structure[49] in the **Figure 2.10b**.

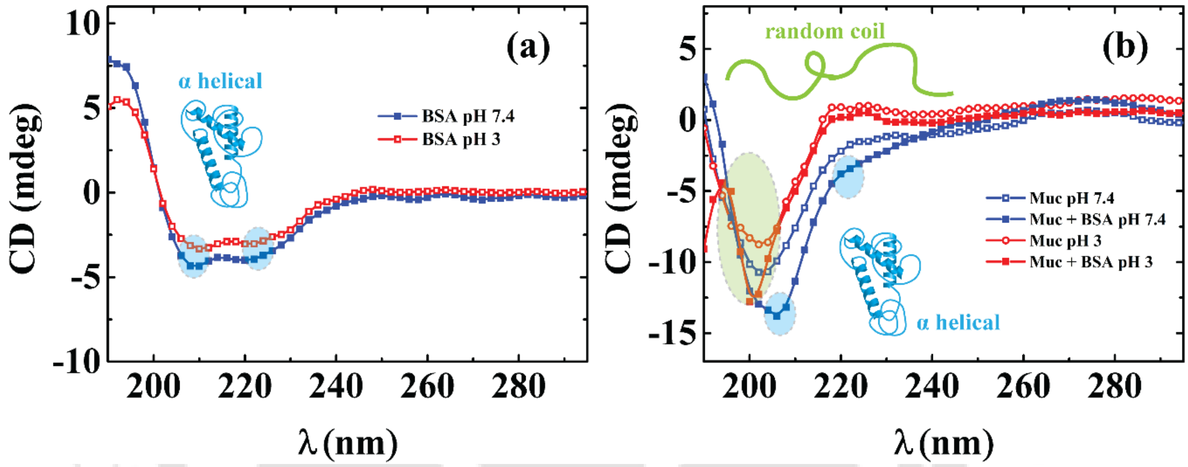

Figure 2.10. Secondary structure determination of BSA, mucin and mucin-BSA complex at pH 7.4 and pH 3. (a) CD spectra of BSA at pH 7.4 and pH 3, (b) CD spectra of mucin, and mucin BSA complex at pH 7.4 and pH 3.

At pH 7.4 both mucin and mucin-BSA complex shows higher negative ellipticity at around 222 nm, which is the characteristic peak of presence of an α-helix structure. We can also see that the peak intensity for mucin-BSA complex at 222 nm with higher negative values compared to mucin alone. This suggests that binding of BSA might lead to an enhancement in the α-helix structure of mucin. However, this peak is absent in case of both mucin and mucin-BSA complex at pH 3. mucin-BSA complex at pH 7.4 shows characteristic α-helix negative peak at 206 nm which is also absent in case of pH 3, thus corroborating our findings that BSA does not bind with mucins at pH 3. It is also evident from these findings that BSA not only binds with mucin at pH 7.4 but also alters its secondary structure resulting in a higher content of α-helix.

Figure 2.11 schematically shows mucin-albumin assembly and their consequences to the mucus layer. It has already been established in the literature that mucin monomers form oligomers through disulfide bridges,[20,36] which is reflected in decreasing diffusivity of mucins with increasing concentrations.

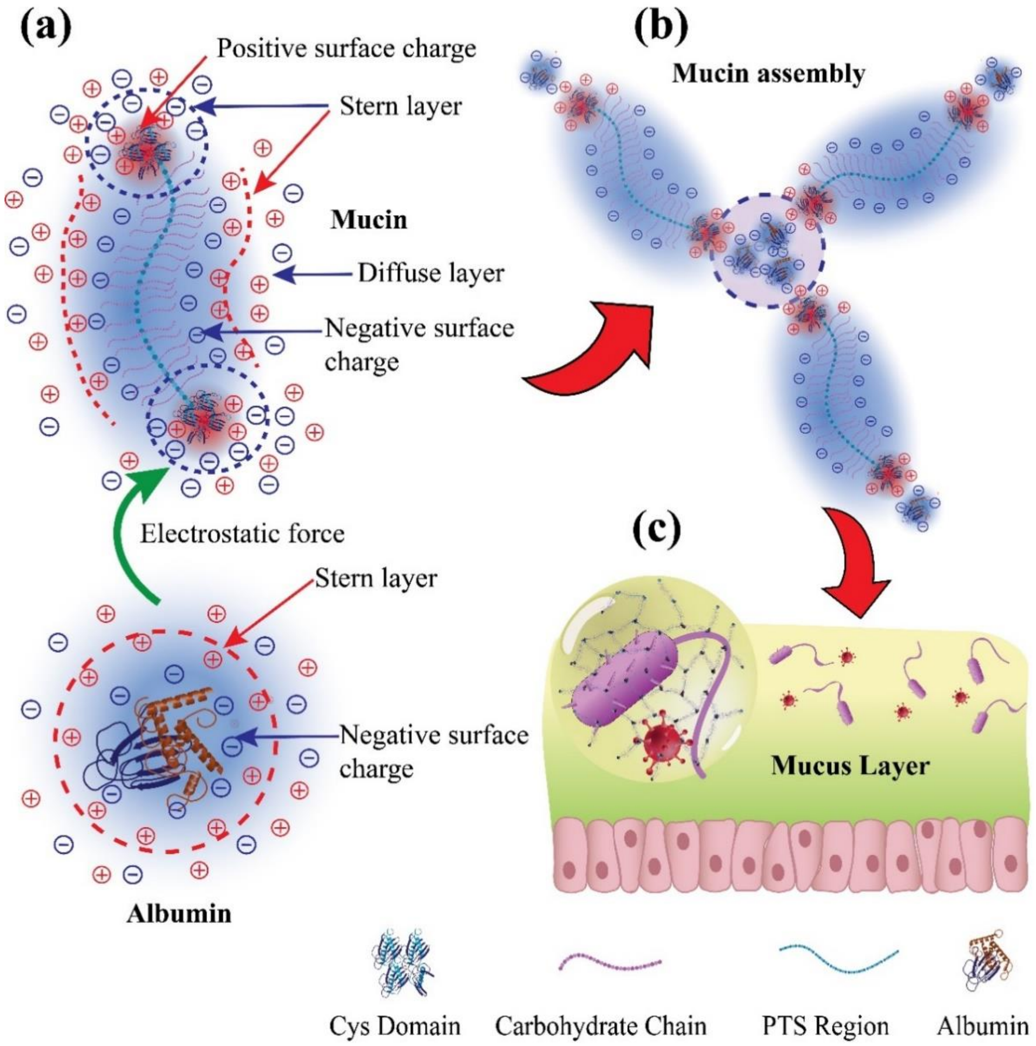

Figure 2.11. Schematic diagram of mucin-albumin assembly. (a) Structure of mucin monomer with negatively charged carbohydrate chains in PTS region and positively charged cysteine rich domains at the ends. Albumin interacts with the cysteine domains of mucin facilitating mucin-mucin binding. (b) Mucin-albumin interaction leads to assembly of more mucin molecules. (c) Hierarchical assembly of mucin-albumin complex with decreased diffusivity, which restricts the penetration of pathogens through the mucus layer.

In view of this background, since the mucus contains albumin and other proteins, it is expected that a more complex assembly of mucin and other proteins may take place in a functional mucus layer. The present work shows the role of albumin in such assemblies, which may have a lasting influence on the microrheology and hence the microstructure of the mucosal layer. In a way, electrostatic interaction and subsequent binding of mucin-albumin can decrease the diffusivity of the micro/nano tracers and hence pathogens to restrict them in their penetration toward the epithelial cells. On the other hand, inside a diseased condition, there can be an elevated albumin loading on the mucus layer which in turn may again change the microstructure of the mucus leading to the mucus-plugs in respiratory systems. **Figure 2.11** summarizes a hypothesis originating from all the experimental evidences obtained. The first and foremost thing we establish that the interaction between the mucin and albumin is largely electrostatic.

Further, **Figure 2.11a** suggest that the dumbbell shaped mucin monomer has a PTS region with electronegative glycosylated carbohydrate chains, which facilitates a negative ζ-potential even in a neutral pH solution. In contrast, the cysteine domains are electropositive locally, which can attract the protein matrices with a negative ζ-potential, such as, BSA. Such interactions eventually result in a hierarchical assembly of mucins as shown in **Figure 2.11b**, which leads to a microstructure causing the decrease in the diffusivity of the tracer elements into the mucin-BSA matrix. This is also the reason behind the increase in the viscosity of such solutions, which is crucial for the inhibition of pathogen penetration through the mucus lining, as depicted in the **Figure 2.11c**. On the other hand, at a lower pH 3, ζ-potential of mucin becomes less negative while BSA acquires a positive ζ-potential, which reduces the BSA-cystine interactions and results in an increase in MSD of the tracers. In such a scenario, inclusion of Ca^{2+} enhances the mucin-BSA crosslinking resulting in additional assembly of mucin.

2.4. Conclusions

In summary, this Chapter shows the variations in the microrheology due to the interactions and assembly of porcine gastric mucins with BSA using a high-precision DWS technique. The study unveils that, although the mucin molecules exist in the form of monomers or dimers due to a disulfide linkage, the overlapping of monomers and dimers leads to the formation of a weakly aggregated network at a higher concentration of mucin. Subsequently, the microrheological response of the solution goes from viscous to viscoelastic. Interestingly, the presence of other proteins such as albumin further facilitates such assembly of the mucins. For example, in such a scenario, the ITC analysis shown here confirms that albumin not only binds with the mucins but also tend to stabilize the physical crosslinking between the mucin domains to facilitate a higher order assembly by forming additional links. As a result, enhancements in both viscous and elastic responses of the materials is observed, which can intuitively be correlated to the gel formation of the mucus in the lung airways due to the secretion of albumin in cysteine fibrosis and asthma diseases. The experiments also corroborate that the mucin-albumin interaction leads to decreased diffusivity of the tracer particles in the mucus layer, which may inhibit the penetration of bacterial and viral pathogens to protect the epithelial cells. Interestingly, the binding of BSA with mucin to form mucin-BSA complexes is found to be strongly dependent on the pH of the solution. For example, at a lower pH 3 emulating the bioenvironment of stomach, the BSA molecules do not bind with mucins owing to the lack of repulsive force between the positive charge of BSA and positive residues of binding site of cysteine domain of mucin.

This leads to a rheological response similar to that of pure mucin. However, at a neutral pH 7.4 emulating the bioenvironment of lungs, the CD analysis of mucin and mucin-BSA samples shows that BSA not only binds with mucin but also alters its secondary structure. In such a scenario, an AFM analysis reveals the presence of concatenated colloidal nano-network of mucin-BSA complex. Concisely, the Chapter highlights some of the fundamental aspects of the interaction of the mucosal proteins with the non-mucinal ones such as albumin to highlight the importance of microrheology of the materials in preventing the pathogenic penetration through the mucosal layers. In the mucus system various other non mucin proteins are also present, though their interaction with mucin is largely unexplored. Investiagting these interactions will shed light on the assembly of an functional mucus layer, which could be advantageous for addressing various mucus related diseases.

References

(1) Chen, Z.; Zhong, M.; Luo, Y.; Deng, L.; Hu, Z.; Song, Y. Determination of Rheology and Surface Tension of Airway Surface Liquid: A Review of Clinical Relevance and Measurement Techniques. *Respir. Res.* **2019**, *20* (1), 1–14. https://doi.org/10.1186/s12931-019-1229-1.

(2) De Lisle, R. C.; Borowitz, D. The Cystic Fibrosis Intestine. *Cold Spring Harb. Perspect. Med.* **2013**, *3* (9), 1–18. https://doi.org/10.1101/cshperspect.a009753.

(3) Henderson, A. G.; Ehre, C.; Button, B.; Abdullah, L. H.; Cai, L. H.; Leigh, M. W.; DeMaria, G. C.; Matsui, H.; Donaldson, S. H.; Davis, C. W.; Sheehan, J. K.; Boucher, R. C.; Kesimer, M. Cystic Fibrosis Airway Secretions Exhibit Mucin Hyperconcentration and Increased Osmotic Pressure. *J. Clin. Invest.* **2014**, *124* (7), 3047–3060. https://doi.org/10.1172/JCI73469.

(4) Bansil, R.; Turner, B. S. The Biology of Mucus: Composition, Synthesis and Organization. *Adv. Drug Deliv. Rev.* **2018**, *124*, 3–15. https://doi.org/10.1016/j.addr.2017.09.023.

(5) Wallace, L. E.; Liu, M.; van Kuppeveld, F. J. M.; de Vries, E.; de Haan, C. A. M. Respiratory Mucus as a Virus-Host Range Determinant. *Trends Microbiol.* **2021**, *29* (11), 983–992. https://doi.org/10.1016/j.tim.2021.03.014.

(6) Linden, S. K.; Sutton, P.; Karlsson, N. G.; Korolik, V.; McGuckin, M. A. Mucins in the Mucosal Barrier to Infection. *Mucosal Immunol.* **2008**, *1* (3), 183–197.

https://doi.org/10.1038/mi.2008.5.

(7) Libao-Mercado, A. J.; de Lange, C. F. M. Refined Methodology to Purify Mucins from Pig Colonic Mucosa. *Livest. Sci.* **2007**, *109* (1–3), 141–144. https://doi.org/10.1016/j.livsci.2007.01.125.

(8) Perez-Vilar, J.; Eckhardt, A. E.; DeLuca, A.; Hill, R. L. Porcine Submaxillary Mucin Forms Disulfide-Linked Multimers through Its Amino-Terminal D-Domains. *J. Biol. Chem.* **1998**, *273* (23), 14442–14449. https://doi.org/10.1074/jbc.273.23.14442.

(9) De Lisle, R. C.; Borowitz, D. The Cystic Fibrosis Intestine. *Cold Spring Harb. Perspect. Med.* **2013**, *3* (9), 1–18. https://doi.org/10.1101/cshperspect.a009753.

(10) Su, C.; Padra, M.; Constantino, M. A.; Sharba, S.; Thorell, A.; Lindén, S. K.; Bansil, R. Influence of the Viscosity of Healthy and Diseased Human Mucins on the Motility of Helicobacter Pylori. *Sci. Rep.* **2018**, *8* (1), 1–13. https://doi.org/10.1038/s41598-018-27732-3.

(11) De Bolós, C.; Garrido, M.; Real, F. X. MUC6 Apomucin Shows a Distinct Normal Tissue Distribution That Correlates with Lewis Antigen Expression in the Human Stomach. *Gastroenterology* **1995**, *109* (3), 723–734. https://doi.org/10.1016/0016-5085(95)90379-8.

(12) Ho, S. B.; Roberton, A. M.; Shekels, L. L.; Lyftogt, C. T.; Niehans, G. A.; Toribara, N. W. Localization of Mucin Gene Expression. *Gastroenterology* **1995**, 735–747.

(13) Nordman, H.; Davies, J. R.; Lindell, G.; De Bolós, C.; Real, F.; Carlstedt, I. Gastric MUC5AC and MUC6 Are Large Oligomeric Mucins That Differ in Size, Glycosylation and Tissue Distribution. *Biochem. J.* **2002**, *364* (1), 191–200. https://doi.org/10.1042/bj3640191.

(14) Guo, X.; Zheng, S.; Dang, H.; Pace, R. G.; Stonebraker, J. R.; Jones, C. D.; Boellmann, F.; Yuan, G.; Haridass, P.; Fedrigo, O.; Corcoran, D. L.; Seibold, M. A.; Ranade, S. S.; Knowles, M. R.; O'Neal, W. K.; Voynow, J. A. Genome Reference and Sequence Variation in the Large Repetitive Central Exon of Human MUC5AC. *Am. J. Respir. Cell Mol. Biol.* **2014**, *50* (1), 223–232. https://doi.org/10.1165/rcmb.2013-0235OC.

(15) Vinall, L. E.; Fowler, J. C.; Jones, A. L.; Kirkbride, H. J.; De Bolos, C.; Laine, A.; Porchet, N.; Gum, J. R.; Kim, Y. S.; Moss, F. M.; Mitchell, D. M.; Swallow, D. M. Polymorphism of Human Mucin Genes in Chest Disease Possible Significance of MUC2. *Am. J. Respir. Cell Mol. Biol.* **2000**, *23* (5), 678–686. https://doi.org/10.1165/ajrcmb.23.5.4176.

(16) Rousseau, K.; Byrne, C.; Kim, Y. S.; Gum, J. R.; Swallow, D. M.; Toribara, N. W. The Complete Genomic Organization of the Human MUC6 and MUC2 Mucin Genes. *Genomics* **2004**, *83* (5), 936–939. https://doi.org/10.1016/j.ygeno.2003.11.003.

(17) Lidell, M. E.; Johansson, M. E. V.; Mörgelin, M.; Asker, N.; Gum, J. R.; Kim, Y. S.; Hansson, G. C. The Recombinant C-Terminus of the Human MUC2 Mucin Forms Dimers in Chinese-Hamster Ovary Cells and Heterodimers with Full-Length MUC2

in LS 174T Cells. *Biochem. J.* **2003**, *372* (2), 335–345. https://doi.org/10.1042/BJ20030003.

(18) Godl, K.; Johansson, M. E. V.; Lidell, M. E.; Mörgelin, M.; Karlsson, H.; Olson, F. J.; Gum, J. R.; Kim, Y. S.; Hansson, G. C. The N Terminus of the MUC2 Mucin Forms Trimers That Are Held Together within a Trypsin-Resistant Core Fragment. *J. Biol. Chem.* **2002**, *277* (49), 47248–47256. https://doi.org/10.1074/jbc.M208483200.

(19) Ambort, D.; Johansson, M. E. V.; Gustafsson, J. K.; Nilsson, H. E.; Ermund, A.; Johansson, B. R.; Koeck, P. J. B.; Hebert, H.; Hansson, G. C. Calcium and PH-Dependent Packing and Release of the Gel-Forming MUC2 Mucin. *Proc. Natl. Acad. Sci. U. S. A.* **2012**, *109* (15), 5645–5650. https://doi.org/10.1073/pnas.1120269109.

(20) Meldrum, O. W.; Yakubov, G. E.; Bonilla, M. R.; Deshmukh, O.; McGuckin, M. A.; Gidley, M. J. Mucin Gel Assembly Is Controlled by a Collective Action of Non-Mucin Proteins, Disulfide Bridges, Ca2+ -Mediated Links, and Hydrogen Bonding. *Sci. Rep.* **2018**, *8* (1), 1–16. https://doi.org/10.1038/s41598-018-24223-3.

(21) Peters, T. *All about Albumin: Biochemistry, Genetics, and Medical Applications*; Academic press, 1996.

(22) Carter, D. C.; Ho, J. X. Structure of Serum Albumin. *Adv. Protein Chem.* **1994**, *45* (C), 153–176. https://doi.org/10.1016/S0065-3233(08)60640-3.

(23) Hemar, Y.; Pinder, D. N. DWS Microrheology of a Linear Polysaccharide. *Biomacromolecules* **2006**, *7* (3), 674–676. https://doi.org/10.1021/bm050566l.

(24) Oelschlaeger, C.; Cota Pinto Coelho, M.; Willenbacher, N. Chain Flexibility and Dynamics of Polysaccharide Hyaluronan in Entangled Solutions: A High Frequency Rheology and Diffusing Wave Spectroscopy Study. *Biomacromolecules* **2013**, *14* (10), 3689–3696. https://doi.org/10.1021/bm4010436.

(25) Mason, T. G.; Gang, H.; Weitz, D. A. Diffusing-Wave-Spectroscopy Measurements of Viscoelasticity of Complex Fluids. *J. Opt. Soc. Am. A* **1997**, *14* (1), 139. https://doi.org/10.1364/josaa.14.000139.

(26) Scheffold, F.; Schurtenberger, P. Light Scattering Probes of Viscoelastic Fluids and Solids. *Soft Mater.* **2003**, *1* (2), 139–165. https://doi.org/10.1081/smts-120022461.

(27) Pine, D.J.; Weitz, D.A.; Zhu, J.X.; Herbolzheimer, E. Diffusing-Wave Spectroscopy: Dynamic Light Scattering in the Multiple Scattering Limit. *J. Phys. Fr.* **1990**, *51* (18), 2101–2127. https://doi.org/10.1051/jphys:0199000510180210100.

(28) Afshinnia, K.; Baalousha, M. Effect of Phosphate Buffer on Aggregation Kinetics of Citrate-Coated Silver Nanoparticles Induced by Monovalent and Divalent Electrolytes. *Sci. Total Environ.* **2017**, *581–582*, 268–276. https://doi.org/10.1016/j.scitotenv.2016.12.117.

(29) Bansil, R.; Stanley, E.; Thomas LaMont, J. Mucin Biophysics. *Annu. Rev. Physiol.* **1995**, *57* (84), 635–657. https://doi.org/10.1146/annurev.ph.57.030195.003223.

(30) Waigh, T. A. Advances in the Microrheology of Complex Fluids. *Reports Prog. Phys.* **2016**, *79* (7). https://doi.org/10.1088/0034-4885/79/7/074601.

(31) Weitz, D.; Brown, D. P.-W.; Ed, undefined; 1993, undefined. Dynamic Light Scattering.

(32) Mason, T. G.; Weitz, D. A. Optical Measurements of Frequency-Dependent Linear Viscoelastic Moduli of Complex Fluids. *Phys. Rev. Lett.* **1995**, *74* (7), 1250–1253. https://doi.org/10.1103/PhysRevLett.74.1250.

(33) Clasen, C.; Plog, J. P.; Kulicke, W.-M.; Owens, M.; Macosko, C.; Scriven, L. E.; Verani, M.; McKinley, G. H. How Dilute Are Dilute Solutions in Extensional Flows? *J. Rheol. (N. Y. N. Y).* **2006**, *50* (6), 849–881. https://doi.org/10.1122/1.2357595.

(34) Leal, J.; Smyth, H. D. C.; Ghosh, D. Physicochemical Properties of Mucus and Their Impact on Transmucosal Drug Delivery. *International Journal of Pharmaceutics*. Elsevier B.V. October 30, 2017, pp 555–572. https://doi.org/10.1016/j.ijpharm.2017.09.018.

(35) Yakubov, G. E.; Papagiannopoulos, A.; Rat, E.; Easton, R. L.; Waigh, T. A. Molecular Structure and Rheological Properties of Short-Side-Chain Heavily Glycosylated Porcine Stomach Mucin. *Biomacromolecules* **2007**, *8* (11), 3467–3477. https://doi.org/10.1021/bm700607w.

(36) Waigh, T. A.; Papagiannopoulos, A.; Voice, A.; Bansil, R.; Unwin, A. P.; Dewhurst, C. D.; Turner, B.; Afdhal, N. Entanglement Coupling in Porcine Stomach Mucin. *Langmuir* **2002**, *18* (19), 7188–7195. https://doi.org/10.1021/la025515d.

(37) Godl, K.; Johansson, M. E. V.; Lidell, M. E.; Mörgelin, M.; Karlsson, H.; Olson, F. J.; Gum, J. R.; Kim, Y. S.; Hansson, G. C. The N Terminus of the MUC2 Mucin Forms Trimers That Are Held Together within a Trypsin-Resistant Core Fragment. *J. Biol. Chem.* **2002**, *277* (49), 47248–47256. https://doi.org/10.1074/jbc.M208483200.

(38) Bhaskar, K. R.; Gong, D.; Bansil, R.; Pajevic, S.; Hamilton, J. A.; Turner, B. S.; LaMont, J. T. Profound Increase in Viscosity and Aggregation of Pig Gastric Mucin at Low PH. *Am. J. Physiol. - Gastrointest. Liver Physiol.* **1991**, *261* (5 24-5). https://doi.org/10.1152/ajpgi.1991.261.5.g827.

(39) Phan, H. T. M.; Bartelt-Hunt, S.; Rodenhausen, K. B.; Schubert, M.; Bartz, J. C. Investigation of Bovine Serum Albumin (BSA) Attachment onto Self-Assembled Monolayers (SAMs) Using Combinatorial Quartz Crystal Microbalance with Dissipation (QCM-D) and Spectroscopic Ellipsometry (SE). *PLoS One* **2015**, *10* (10). https://doi.org/10.1371/journal.pone.0141282.

(40) Kopac, T.; Bozgeyik, K.; Yener, J. Effect of PH and Temperature on the Adsorption of Bovine Serum Albumin onto Titanium Dioxide. *Colloids Surfaces A Physicochem. Eng. Asp.* **2008**, *322* (1–3), 19–28. https://doi.org/10.1016/j.colsurfa.2008.02.010.

(41) Käsdorf, B. T.; Weber, F.; Petrou, G.; Srivastava, V.; Crouzier, T.; Lieleg, O. Mucin-Inspired Lubrication on Hydrophobic Surfaces. *Biomacromolecules* **2017**, *18* (8), 2454–2462. https://doi.org/10.1021/acs.biomac.7b00605.

(42) Yakubov, G. E.; Papagiannopoulos, A.; Rat, E.; Waigh, T. A. Charge and Interfacial Behavior of Short Side-Chain Heavily Glycosylated Porcine Stomach Mucin.

Biomacromolecules **2007**, *8* (12), 3791–3799. https://doi.org/10.1021/bm700721c.

(43) Curnutt, A.; Smith, K.; Darrow, E.; Walters, K. B. Chemical and Microstructural Characterization of PH and [Ca2+] Dependent Sol-Gel Transitions in Mucin Biopolymer. *Sci. Rep.* **2020**, *10* (1), 21–23. https://doi.org/10.1038/s41598-020-65392-4.

(44) Khodir, W. K. W. A.; Hakim, A.; Kobayashi, M. Strength of Flocs Formed by the Complexation of Lysozyme with Leonardite Humic Acid. *Polymers (Basel).* **2020**, *12* (8). https://doi.org/10.3390/polym12081770.

(45) Hakim, A.; Suzuki, T.; Kobayashi, M. Strength of Humic Acid Aggregates: Effects of Divalent Cations and Solution PH. *ACS Omega* **2019**, *4* (5), 8559–8567. https://doi.org/10.1021/acsomega.9b00124.

(46) Raynal, B. D. E.; Hardingham, T. E.; Thornton, D. J.; Sheehan, J. K. Concentrated Solutions of Salivary MUC5B Mucin Do Not Replicate the Gel-Forming Properties of Saliva. *Biochem. J.* **2002**, *362* (2), 289–296. https://doi.org/10.1042/0264-6021:3620289.

(47) Li, R.; Wu, Z.; Wangb, Y.; Ding, L.; Wang, Y. Role of PH-Induced Structural Change in Protein Aggregation in Foam Fractionation of Bovine Serum Albumin. *Biotechnol. Reports* **2016**, *9*, 46–52. https://doi.org/10.1016/j.btre.2016.01.002.

(48) El Kadi, N.; Taulier, N.; Le Huérou, J. Y.; Gindre, M.; Urbach, W.; Nwigwe, I.; Kahn, P. C.; Waks, M. Unfolding and Refolding of Bovine Serum Albumin at Acid PH: Ultrasound and Structural Studies. *Biophys. J.* **2006**, *91* (9), 3397–3404. https://doi.org/10.1529/biophysj.106.088963.

(49) Barbero, N.; Coletti, M.; Catalano, F.; Visentin, S. Exploring Gold Nanoparticles Interaction with Mucins: A Spectroscopic-Based Study. *Int. J. Pharm.* **2018**, *535* (1–2), 438–443. https://doi.org/10.1016/j.ijpharm.2017.11.026.

CHAPTER 3

Microrheology of Ionic Liquid Doped Mucus for an Efficient Delivery of Protein-based Oral Drugs

Contents

ABSTRACT

Developing protein-based drugs for oral administration is one of the most challenging aspects of the pharmaceutical industry. Such medications are less bioavailable due to their low stability and inability to permeate through the intestinal barriers of mucus. A few recent works have shown that ionic liquids (ILs) can be combined with protein-based drugs to improve their stability under in-vivo conditions enhancing their mucus-penetrating capabilities. One of the major knowledge gaps in this regard has been the interactions among protein-based drugs, ILs, and mucin, which can play a pivotal role in such drug delivery processes. The present Chapter unveils the diverse molecular mechanisms that play key roles during the delivery of protein-based drugs, with the help of systematic microrheology experiments and density functional theory (DFT) simulations. The study employs a model mesoscale drug delivery system composed of an IL (choline bicarbonate: maleic acid – 2:1), a protein (mucin), and bovine serum albumin (BSA) as a model drug. In particular, following the microrheological changes of such drug formulations helps in tracing the charge transfer mechanism and molecular interactions such as electrostatic, van der Waals, steric, and hydrogen bonds, at the various stages of BSA, mucin, and IL assemblage. The results have been corroborated by the morphological studies using atomic force microscopy (AFM) supplemented by the microrheological studies using diffusing-wave spectroscopy (DWS). Further, a human intestine has also been simulated as a biomimetic in-vitro microfluidic prototype to demonstrate a larger stability and penetration of BSA through mucin in the presence of IL.

3.1. Introduction

Over the years, oral drug delivery has been preferred over intravenous ones owing to their ease of administration alongside the capacity to facilitate a sustained release.[1–3] Of late, the intravenous administration of protein-based drugs such as insulin or monoclonal antibodies has been found to have severe side effects such as the suppression of the immune system during the repeated usage.[4] In such a scenario, intensive research efforts have been invested to develop protein-based drug formulations that can be delivered orally. However, protein-based oral drug formulations need to be designed in such a manner that they are not only stable in the harsh biochemical environment of the gastrointestinal tract but can also diffuse easily through the thin viscoelastic mucus layer coated on the inner surface of the stomach and intestines.[5–7]

It is now well understood that the mucus layer present in the inner tract of the gut or intestine can kinetically control the transport of materials into the body with the help of its unique rheological maneuvering. First of all, the surface of a mucus[8–10] film is specifically designed to selectively absorb nutrients while preventing the entry of various pathogens.[11–13] For example, the mucus film acts as the primary layer of defense to filter out the larger molecules (>100 nm) and allows the permeation of smaller ones (<100 nm) to diffuse inside the human body.[14,15] Different types of binding and charged interactions between the nutrients and the mucus also play key roles in the absorption and transport of the same inside the body. For example, the positively charged particles are more prone to binding with the sialic acid residues of mucin molecules,[16] while the negatively charged peptides or protein molecules also have tendencies towards binding with the mucin part of the mucus layer.[17,18] Interestingly, during the diseased condition, a more viscous mucus lining can also kinetically impede the entry of nutrients or pathogens, whereas a thinner mucus lining during a healthy state of a human body can promote a much faster diffusion. Thus, it is of utmost importance to understand the microrheology of various protein-based drug moieties while they transport through the mucus layer, which may help in the translation of the protein-based oral formulations.

Of late, one of the major aims of research in this regard has been to develop in-vitro models that can emulate the in-vivo gut or intestinal conditions which in turn can be employed for the design and testing of the efficacy of the absorption and transport of protein-based drug formulations. **Figure 3.1a** schematically shows that complex microrheological transport, filtering, and absorption are some of the key factors that impair the development of protein-based oral medicines. For example, during some of the diseased states of mucus, e.g. ‘fibrosis’, a viscous thickening of the mucus layer often disallows the permeation of the required drugs. In order to circumvent this problem, there is a need for the modulation of the mucus layer, which can facilitate the absorption of drugs during the highly viscous state of the mucus.

In recent times, a plethora of research activities have been observed wherein ‘smart’ carrier molecules have been designed to facilitate the transport of protein-based drugs through the mucus layer.[1,19–21] For example, the ionic liquids (ILs), with a low melting point, lower vapor pressure, high thermal stability, and higher solvation properties, are found to be very much suitable for facile delivery of poorly water-soluble drugs through a highly viscous lining of mucus.[22] The ILs have an inherent capacity to penetrate the various barriers such as skin and buccal mucosa to intestines.[20,21,23,24] Thus, a concoction of drugs like insulin and monoclonal antibodies with ILs have been synthesized before testing them under in-vitro conditions to elucidate their efficacy in drug transport through the mucus layer. For example, a very recent study has demonstrated that the IL-choline glycolate can enhance the uptake of IgG in the jejunum by reducing the viscosity of mucus.[25]

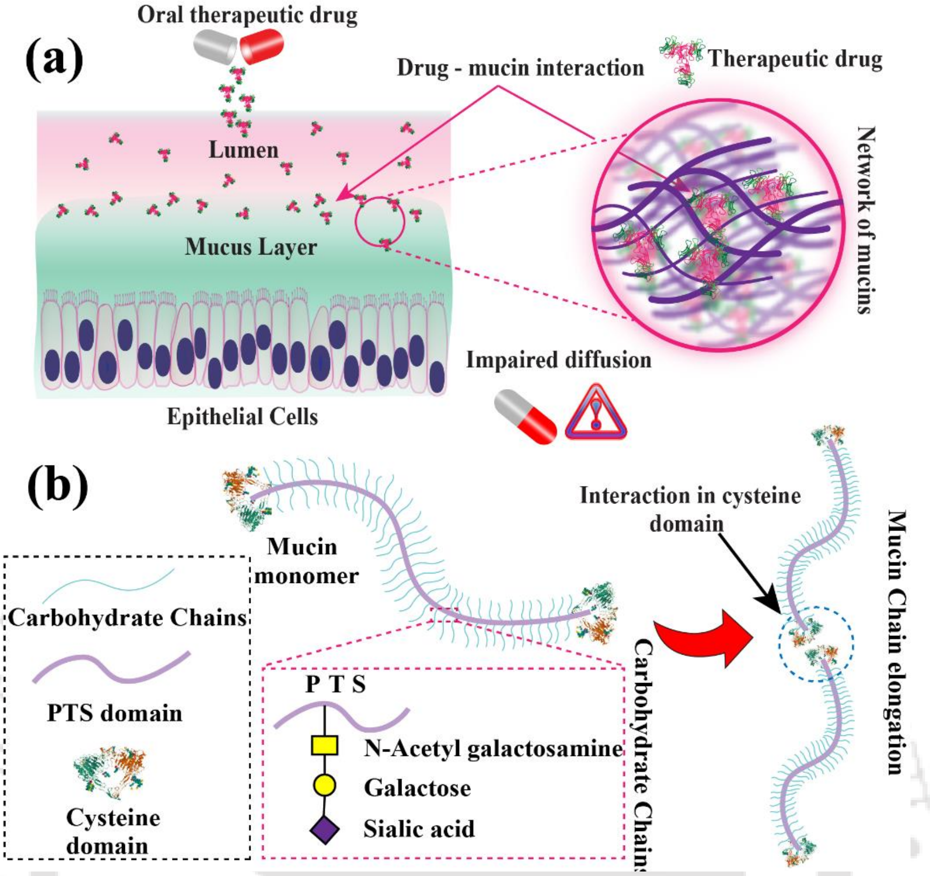

Figure 3.1. (a) Schematic representation of the mucus layer which acts as a barrier against therapeutic drugs; (b) mucus is formed by the assembly of mucin proteins, the structure of a mucin monomer.

At this stage, it is also important to note that the key components of the mucus layer are different types of mucins such as MUC2, MUC5AC, MUC5B, MUC6, and MUC19,[12] which are glycoproteins with ~80% carbohydrate and ~20% protein matrices.[26] The carbohydrate chain includes sialic acid, fucose, galactose, and N-acetyl-galactosamine, which are linked with PTS amino acid residues, namely proline, threonine, and serine as shown in **Figure 3.1b**.[12] The terminal part of gel-forming mucin is rich in cysteine residues,[27] which enables various forms of chain propagation and cross-linking behaviors to alter the rheological properties during the diseased states of health. On the other hand, a lower-than-normal viscosity of gastric mucus leads to ulcers.[28,29] This highlights the importance of maintaining the proper rheology of mucin for the optimal functioning of many organs in the human. The prior art reports that the mucin moieties bind with different non-mucin proteins to form a more compact structure.[30,31] In the case of diseased conditions like asthma, albumin electrostatically binds with the mucin components and results in a cluster-like formation.[31] A similar situation may also emerge in the case of protein-based drugs like insulin and monoclonal antibodies, where the proteins bind with the mucin components and impede their diffusion through the mucus layer. This creates a substantial challenge in the development of oral-based drug formulations. Certainly, there is a need to modulate the microrheology of the mucus layer so that protein-based oral drug formulations can penetrate through the mucus layer before absorbing in the human body to address the diseased tissues.

In view of this background, the present chapter focuses on synthesizing an array of composite ILs composed of choline bicarbonate and maleic acid, by mixing them at different ratios before characterizing them using ^{1}H NMR spectroscopy. Afterward, we investigate the effects of IL on the viscoelastic behavior of mucin through microrheology and bulk-rheology experiments. Subsequently, AFM studies are performed to provide insights into the morphological changes of mucin after the treatment with the ILs. To understand the interaction between drugs and mucin, we have utilized bovine serum albumin (BSA) as a model therapeutic protein and observed their rheology with and without IL. In a way, treating albumin as a model therapeutic protein, we explore the rheological properties of the mucin-albumin complex in the presence of the ILs. The experimental observations are corroborated by the DFT simulations to delve into the nature of IL-mucin interactions, focusing on parameters like interaction range, orbital energies, and charge transfer (CT) analysis, thereby exploring the strength and characteristics of non-covalent interactions (NCI). Such quantum chemical (QC) calculations uncover a deeper knowledge at the atomic and molecular levels.[32–35] Finally, we have fabricated a mucus-on-chip device employing a native partially purified mucin to simulate an intestinal condition wherein the temporal diffusion of a FITC-labeled antibody is monitored across the simulated in-vitro intestinal environment. The proposed mucus-on-chip device helps in understanding the diffusional aspects of antibodies through mucin.

3.2. Experimental Section

3.2.1. Materials

Porcine mucin (98% pure) and γ-globulin were purchased from Sigma-Aldrich Pvt. Ltd., Bovine serum albumin – BSA (98% pure) was purchased from Sisco Research Laboratories Pvt. Ltd (SRL). Choline bicarbonate and maleic acid were purchased from Sigma-Aldrich Pvt. Ltd. The polystyrene tracer particle with a diameter of 510 nm (10%) was purchased from LS Instruments AG, Switzerland. Single crystal silicon (Si) wafers, specifically prime grade (<100>, n-type), with a thickness of 525 µm, were acquired from Vin Karola Instruments (USA). The SU-8 2075 permeant epoxy negative photoresist, along with its corresponding developer solution, was sourced from KAYAKU Advanced Materials (USA). Additionally, the polydimethylsiloxane (PDMS, Sylgard 184) was obtained from Dow Corning Corporation. All the chemicals are used without further purification. Milli-Q water was used in all experiments for preparing solutions.

3.2.2. Preparation of mucin–BSA complex and IL

All the mucin and mucin-BSA solutions were prepared in 10 mM phosphate buffer saline (PBS). For mucin-albumin solutions, BSA was mixed with the prepared mucin solutions and allowed to mix properly overnight in a rocker at 4°C. The initial concentration of mucin stock solution was 100 mg/mL, to which 4 mg/mL BSA was subsequently added for the mucin-albumin solution. For the concentration-dependent experiments, the stock solution was diluted with 10 mM PBS buffer. Prior to the microrheology measurement, 80 µL of polystyrene tracer particles were added to 920 µL of the prepared sample. The tracer particle concentration was kept at 0.8% in all microrheological experiments and did not affect the overall experimental results. For the microfluidic experiment, before the preparation, BSA and γ-globulin (antibody) were labeled with FITC dye as described in the previous literature and observed under 2.5X objective with an excitation wavelength at 495 nm.[36,37] All the measurements were performed thrice for the precision and reproducibility of the data. ILs were synthesized using three ratios of choline bicarbonate and maleic acid, such as 1:2, 1:1, and 2:1 where the salt metathesis reaction occurred as depicted in **Figure 3.2a**. After mixing these components, the resulting mixture was kept for some time to complete the evolution of CO_2 gas. After the gas was discarded, the liquid mixtures were put to vacuum drying at 60°C for 24-36 h to remove moisture. The ILs after successful-

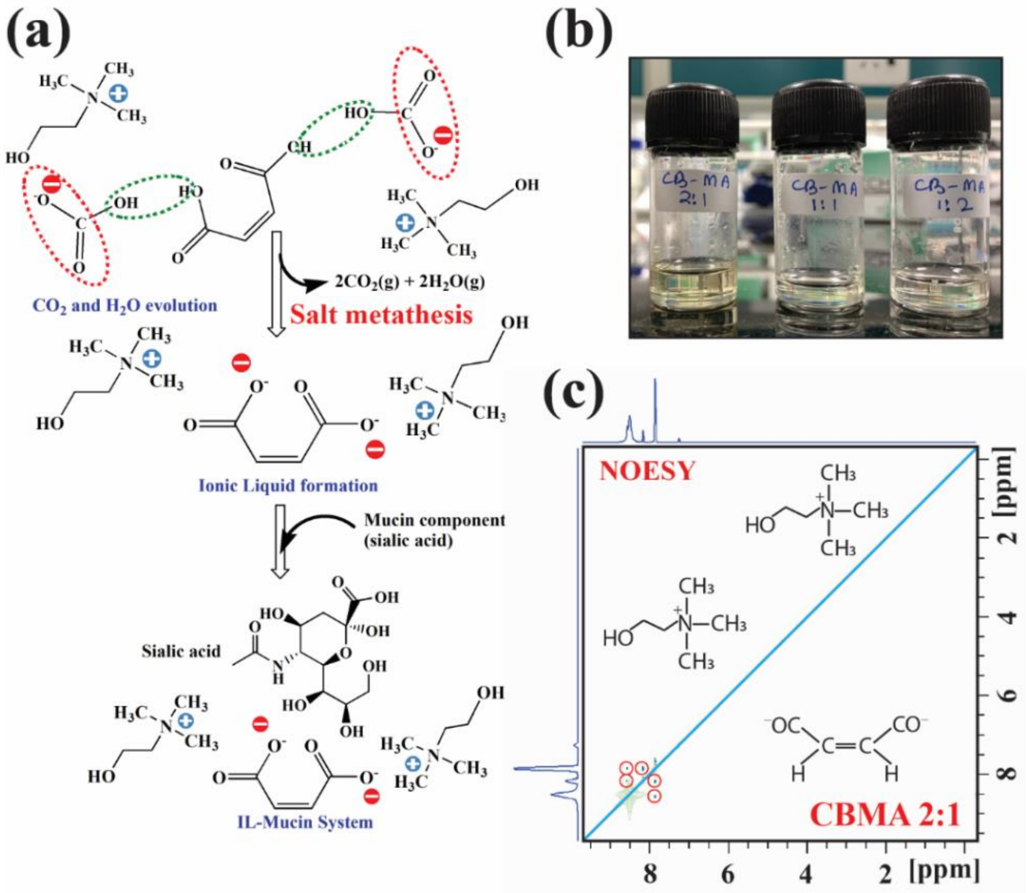

Figure 3.2. (a) Synthesis of 2:1, 1:1, and 1:2 CBMA IL by salt metathesis reaction which further reacts with mucin components (b) image showing pale yellow colored synthesized IL, (c) 2D-^{1}H NOESY spectra for CBMA (2:1) IL, showing the red-circled through-space interactions.

-drying turned out to be clear and transparent **(Figure 3.2b)**. These IL formulations were characterized by $_1$H NOESY NMR.

3.2.3. DWS Microrheology

The diffusing wave spectroscopy (DWS) is utilized for all microrheological assessments, employing a light scattering technique to determine microrheology in turbid samples.[8,38] To make the samples turbid, 10% polystyrene tracer particles, with a diameter of 510 nm, were added. Before the measurement, the samples were placed in a 2 mm cuvette and allowed to incubate for 10 min at 37°C in the sample holder of the instrument. The microrheology measurements were conducted using the DWS RheoLab instrument by LS Instruments AG, Switzerland. A laser light of wavelength 685 nm is incident onto the cuvette containing the sample. The Brownian motion of tracer particles causes light intensity fluctuations over time, and a correlator measures the autocorrelation function $\left[g_2(\tau)-1\right]$ to assess the ensemble-averaged mean squared displacements (MSD) of the tracer particles, indicated as $\left\langle \Delta r^2(\tau)\right\rangle$. [39] The relationship between the MSD and the lag time (τ) for a particle undergoing Brownian motion in a viscoelastic liquid is delineated as

$$\left\langle \Delta r^2(\tau)\right\rangle = 2nD_t\tau^{\alpha}. \qquad (1)$$

Where D_t is the time-dependent diffusivity of the tracer particle and $0 < \alpha < 1$, n refers to the dimensionality (n =3 for a 3-dimensional analysis). For a tracer particle diffusing in a purely viscous environment, the exponent α = 1 and the diffusion coefficient D of the probe is inversely proportional to the viscosity (η) of the surrounding liquid. The viscoelastic modulus can be calculated from the MSD using the generalized Stokes-Einstein relation,[40, 41]

$$G(s) = \frac{k_B T}{\pi a s\left\langle \Delta r^2(s)\right\rangle}, \qquad (2)$$

where $G(s)$ is the Laplace transform of the viscoelastic relaxation modulus $G(t)$, $\left\langle \Delta r^2(s)\right\rangle$ is the Laplace transform of the MSD, k_B is the Boltzmann constant, T is absolute temperature, and a is the radius of the tracer particle. Replacing s with iω, we can get the complex modulus $\left(G^{*}(\omega)\right)$ and complex viscosity $\left(\eta^{*}(\omega)=G^{*}(\omega)/\omega\right)$.

3.2.4. Morphological study by AFM

Atomic force microscope - AFM (Cypher Asylum, Oxford) instrument was used for the morphological characterization. For this, mucin and mucin-treated ionic liquid samples were diluted 100 times and drop cast on a cleaned silicon wafer, and allowed to settle for 15 min. After that, excess samples were pipetted out washed with Milli-Q water, and dried overnight in a vacuum desiccator. The scan rate was kept at 1-2 Hz, and the set point was around 500 mV. The images were analyzed using Gwyddion software.

3.2.5. Bulk Rheology

For bulk rheology experiments, Anton Paar MCR 301 Rheometer was used. The measurements were carried out using a 50 mm diameter 1-degree cone and plate geometry at 37℃. All the measurements were taken in triplicates and the mean data was plotted along with the standard deviations.

3.2.6. Preparation of mucin sample isolated from pig intestine

For the collection of Porcine pig mucus samples, pig intestine was procured from a registered local butcher shop where pigs were slaughtered on a daily basis. The intestine was washed with phosphate buffer saline (PBS) and with the help of a scalpel, the intestine was segmented longitudinally. The mucus was isolated with the help of a spatula to avoid disturbance of the epithelial tissue. After that, mucin was partially purified as described in the previous reports. Briefly, mucus was diluted with 10 mM phosphate buffer with 170 mM NaCl and 0.04% (wt./v) NaN_3 with the pH adjusted to 7.4. Further, 5 mM benzamidine HCl, 1 mM 2,4-dibromo acetophenone, 1 mM phenylmethylsulphonyl fluoride, and 5 mM EDTA were added to the solution to inactivate the protease enzyme. After that, solubilized mucin was centrifuged at 8300 × g for 30 min at 4℃. The supernatant was again centrifuged at 15000 × *g* for 45 min at 4°C. The resulting supernatant was stored at −20°C for up to 1 week before being subjected to lyophilization. Prior to the experiment, mucin was reconstituted in a 10 mM PBS buffer. For the morphological analysis by FESEM, partially purified mucin was treated with CBMA 2:1 (3% v/v) before the lyophilization process.

3.2.7. Computational Methodology

In order to uncover the types of possible intermolecular interactions of IL-mucin-albumin system originating from the charge transfer (CT), short-medium range interactions, chemical stability, and a network of non-covalent interactions, we have performed a host of density functional theory (DFT) simulations and the results from the same has been summarized in the results and discussion section. This analysis provides valuable atomistic-level information for these complex systems. The simulation protocol has been executed based on the reaction mechanism of the formation of IL and that of IL-mucin complexes, as depicted in **Figure 3.2a**.

For this purpose, the CBMA (2:1) ionic liquid structure was optimized initially by placing two choline cations around one maleate (2−) anion. Bicarbonate reacts with maleic acid's (−COOH) groups to produce CO_2 gas and water. Accordingly, maleic acid turns into a maleate ion losing two H^+ ions from both ends. Thus, here, choline cation and maleate anion (2−) act as hydrogen bond acceptor (HBA) and hydrogen bond donor (HBD), respectively. Later, the optimized structures of the individual mucin components (sialic acid, N-Acetylgalactosamine, and cysteine) and positively charged amino acids (arginine, histidine) are placed around the optimized IL structure in various positions to obtain the optimized geometry arrangement of IL-mucin systems using Gaussview 6 and Gaussian 16 at B3LYP- 6-311+G(d,p) basis set.[42–44]

The atom-pairwise correction techniques developed by Grimme and his colleagues, specifically the Becke-Johnson damping method (D3BJ), have been employed to accurately consider the long-range dispersion effects between the HBA and the HBD.[45,46] The energy minima have been determined from the resulting stationary points on the potential energy surface by vibrational frequency analysis. The most stable conformations were obtained. The counterpoise method has been employed to eliminate the basis set superposition error in the computation of the interaction energy and other quantum chemical calculations.[47]

An analysis of natural bond orbital (NBO) charges is conducted to study the distribution and transfer of charges among IL and mucin components.[48] The NBO study clarifies the charge transfer (CT) profile by analyzing the distribution of charges among the components. Additionally, frontier molecular orbital (FMO) analysis[49] has been performed to examine the electronic structure of molecules based on the overlap of frontier orbitals (HOMO & LUMO - highest occupied and lowest unoccupied molecular orbitals) and electronic transitions. In order to thoroughly examine the intermolecular interactions between the HBA and HBD, Bader's quantum theory of atoms in molecules (QTAIM) technique, along with noncovalent interaction (NCI) and reduced density gradient (RDG) analyses have been used through the MultiWFN tool. [50–53] The NCI analysis is utilized to identify distinct interaction zones within the IL-mucin complexes and to determine the electron density distribution of ILs with varying levels of density and density gradients. The comprehensive calculation procedure for the NCI analysis is outlined in the forthcoming parts of the "noncovalent interaction analysis".

3.2.8. Fabrication of microchannels

For diffusion analysis, we prepared two different types of microchannels, one is a T-type channel, and the other is a pillar-embedded microchannel. For the T-type channel, we have employed the conventional replica molding technique by using copper wires of diameter 1 mm and 0.3 mm. For the preparation of pillars embedded microchannel, initially, a design was prepared by using KLayout software which was adapted from previous reports.[54] **Figure 3.3** shows the schematic diagram for the preparation of the microchannel. The silicon (Si) wafer underwent a thorough cleaning regimen involving sequential immersions in ethanol (EtOH), isopropyl alcohol (IPA), and deionized (DI) water, each repeated four times, followed by drying with nitrogen (N_2) gas to eliminate extraneous particles. Subsequently, a soft baking process was executed on the silicon wafer to a temperature of 170°C for 10 min, followed by a controlled cooling phase. The application of negative photoresist SU-8 2075 onto the Si wafer surface involved a two-step spin-coating method at 500 rpm for 30 s and then at 2000 rpm for 90 s to get 110 µm resist thickness. Pre-exposure baking ensued at 65°C for 5 min, and at 95°C for 15 min, with interstitial cooling periods between each step. UV laser exposure at 375 nm, employing a meticulously configured design using KLayout software, was performed by a direct laser instrument (Model: Dilase 250, France), followed by post-exposure baking in two stages: 65°C for 5 min and 95°C for 8 min, with requisite cooling intervals. Subsequent development steps utilized via SU-8 developer, involving sequential immersion of the Si wafer for 40 s and subsequent immersion in IPA solution for an additional 40 s, iterated until only exposed regions remained. The final stage involved drying with N_2 gas and subjecting the wafer to a rigorous hard bake at 250°C for 30 min.

For the replica molding method, the poly-dimethylsiloxane (PDMS) and curing agent were meticulously mixed for 30 min in a 1:10 ratio, ensuring the prevention of air bubble formation during the mixing process. Subsequently, the homogenized mixture was poured into a mold situated on a silicon wafer, featuring the desired design. The mold, crafted from double-sided tapes, defined the shape of the resultant structure. After carefully pouring the PDMS solution into the mold, the assembly was placed in a hot air oven set at 80°C for 3 h. After completing the curing process, the cast was delicately extracted from the mold using acetone. To ensure optimal cleanliness and strict adherence to standard protocols, the microchannel was thoroughly cleaned. Finally, it was affixed to a microscopic cover glass through an oxygen plasma treatment. Inlets and outlets are made using a 1 mm biopsy punch and attached to a 1 mm silicon tube.

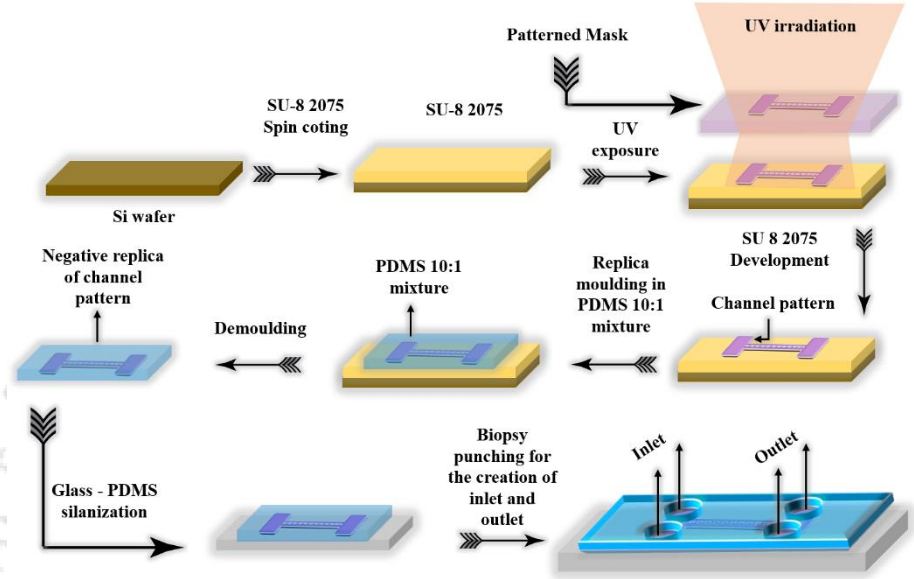

Figure 3.3. Schematic diagram of preparation of mucus-on-a-chip device by the UV-photolithographic technique.

3.3. Results and Discussion

3.3.1. Characterization of IL by 2D-NOESY NMR

The work employed 2-dimensional (2D) Nuclear Overhauser Effect Spectroscopy (NOESY) NMR to identify chemical interactions occurring through physical space. The NOESY NMR research confirms the presence of an intricate network of non-bonded interactions between the components of the ionic liquid (choline and maleate), which aligns with the structural observations made throughout the experiments. This uncovered the intermolecular dispersion and van der Waals interactions among the constituents during the creation of the IL. The interaction between the hydrogen atoms connected to the central carbon atoms of maleate (C=C) and the central carbon atoms of choline can also be observed. A detailed explanation of this interaction can be found in **Figure 3.1c**.

3.3.2. Bulk and Microrheological Experiments

In the beginning of this study, diffusing wave spectroscopy (DWS) is utilized to investigate the effects of IL, i.e., choline bicarbonate: maleic acid (CBMA), on the microrheology of mucin. For this purpose, as mentioned in the experimental section, 50 mg/mL mucin is treated with 2:1, 1:1, and 1:2 molar ratios of CBMA. The control is prepared by adding an equal volume of PBS buffer into the mucin solution. **Figure 3.4a** shows the mean squared displacement (MSD) vs. lag time (τ) plot in which MSD decreases for the treated sample compared to that of the control. Interestingly, among the three molar ratios, 2:1 has the lowest MSD followed by 1:1 and 1:2. Further analysis reveals that the power law exponent remains similar for the treated and control, as shown in **Figure 3.4b**. However, the diffusivity decreases to the lowest for the treated mucin at a 2:1 molar ratio. This observation indicates that both CBMA-treated and control show similar sub-diffusive behavior, while the overall movements of the tracer particles are restricted due to the intermolecular winding of the mucins. Furthermore, the bulk rheology analysis was performed using a rheometer, which gives the viscosity vs. shear rate plot, as shown in **Figure 3.4c**.

It is observed that at a low shear rate, there is an increase in the viscosity of treated mucins with a pronounced shear thinning behavior, as compared to the control. However, this change is absent in high shear rate conditions wherein a Newtonian behavior is observed. This signifies that at the low shear rate, the mucin molecules may tend to aggregate by the weak forces for the CBMA-treated samples. This aggregation is minimized in high shear conditions as evident from the negligible changes in viscosity. Interestingly, the molar ratio of 2:1 has the greatest influence when compared to the ratios of 1:1 and 1:2.

Thus, to visualize the impacts of IL on the mucin structure, AFM of mucin and mucin treated with 2:1 CBMA has been performed. Repeated ‘beading’ and ‘branching’ nano-

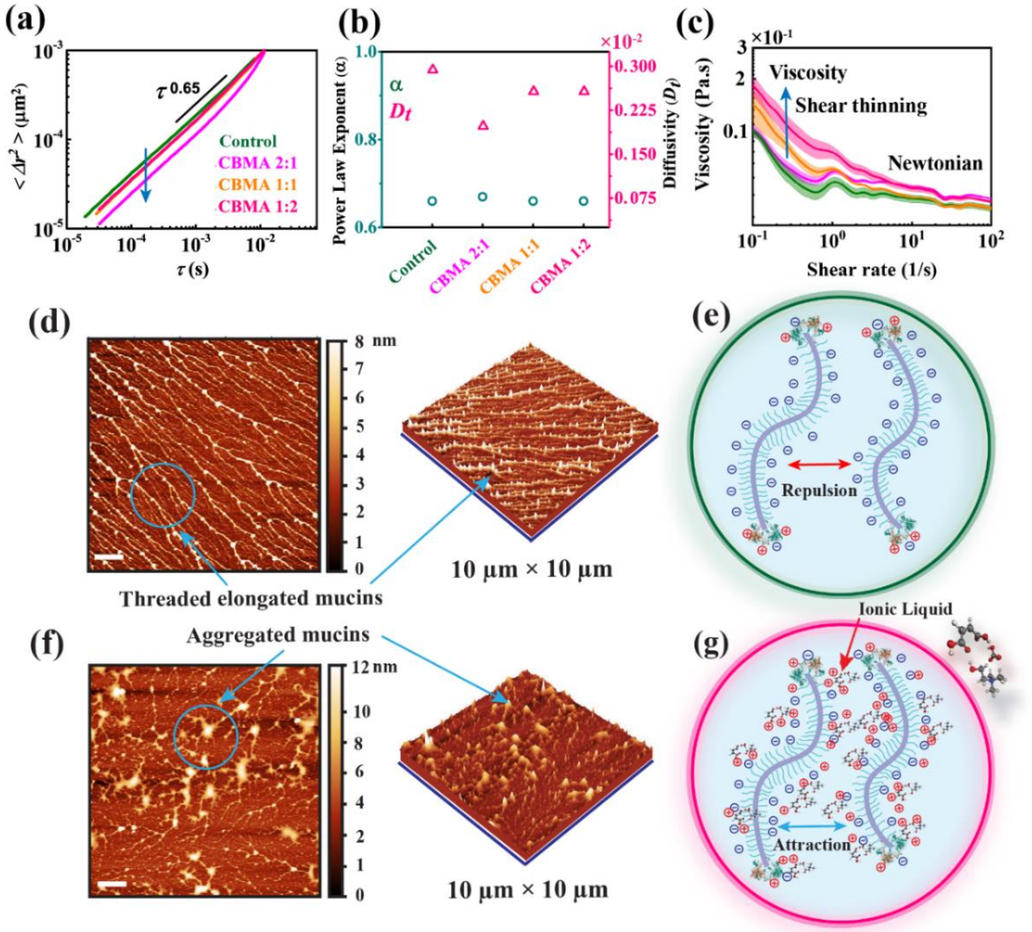

Figure 3.4. Microrheology of mucin treated with different molar ratios of choline bicarbonate-maleic acid ILs. (a) MSD vs. lag time, (b) power law exponent and diffusivity, and (c) Bulk viscosity vs. shear rate. AFM images of mucin and mucin treated with IL. (d) morphological structure of mucin. (e) illustration of repulsion between two mucin monomers due to negatively charged sialic acid residue. (f) morphological structure of mucin treated with IL. The scale bar represents 1.25 μm. (g) illustration of the absence of repulsive force between two mucin monomers due to the shielding of negatively charged sialic acid residue.

-patterns can be observed wherein the threads are joined by the ‘beads’ of height 8 nm, as displayed in **Figure 3.4d**. The thread-like structures are expected to form by the joining of mucin monomers in their cysteine domain regions while the bead-like structures indicate the presence of the cysteine region of mucin monomers where two mucin chains join. Interestingly the beads has a higher height profile this might be due to presence of trace amounts of non-mucin proteins in the cysteine domains. **Figure 3.4e** schematically shows that, due to negative charges in the sialic acid regions, two mucin monomers repel each other, which may eventually result in less aggregated but elongated thread-like structures. However, this kind of structure is majorly absent in the IL-treated mucins, as shown in **Figure 3.4f**.

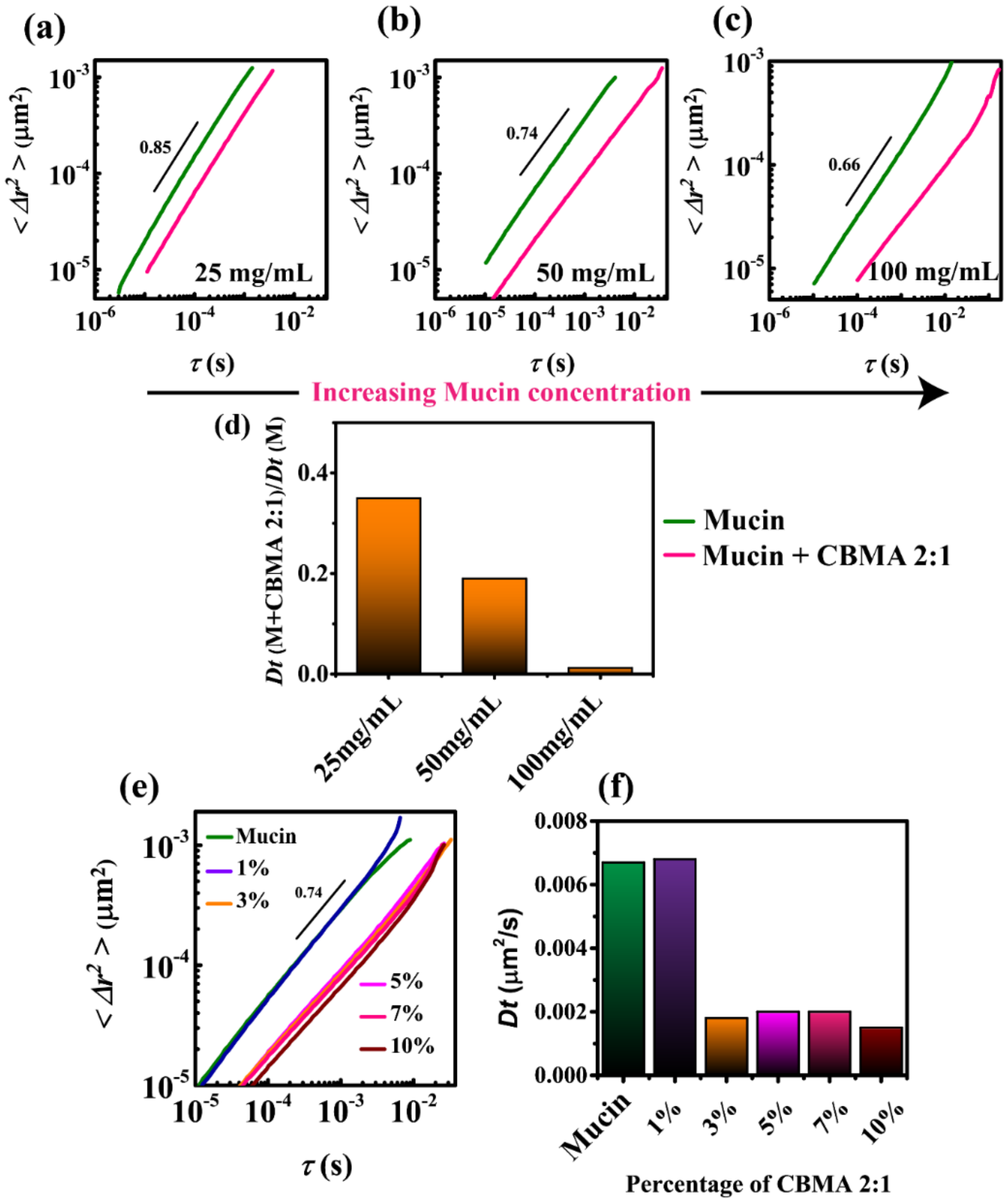

Figure 3.5. MSD at various dosages treatment options for mucin with CBMA 2:1 are (a) 25 mg/ml, (b) 50 mg/ml, and (c) 100 mg/ml mucin; (d) diffusivity ratio of CBMA 2:1 treated and un-treated mucin at varying mucin concentrations; (e) MSD vs. lag time of 50 mg/mL mucin treated with different percentages of IL; (f) diffusivity ratio of CBMA 2:1 treated and un-treated mucin at varying IL percentages.

The aggregated structures depict the interaction between two monomers in the sialic acid regions. **Figure 3.4g** schematically shows the possible reasons for the formation of the mucin aggregates due to the shielding of negative charges of sialic acid residues by the IL matrices. Previously, such structures were also observed in mucin with high salt conditions where the negatively charged sialic acid residues are shielded.[55]

Remarkably, when the concentrations of mucin increase from 25 mg/mL to 100 mg/mL, with 3% v/v IL (CBMA 2:1), the MSD decreases with the lowest at 100 mg/mL, as shown in **Figure 3.5a-c**. In a similar vein, the diffusivity ratio between the IL-treated mucin and pristine mucin shows that at 100 mg/mL mucin concentration, diffusivity reduces up to three times, as shown in **Figure 3.5d**. It may be noted here that the 3% IL concentration is enough to reduce the MSD of high concentrations (100 mg/mL) of mucin. In addition, an analysis of the diffusivity ratio between the treated and untreated mucin demonstrates a two-fold decrease in diffusivity at 50 mg/mL followed by a subsequent decrease at 100 mg/mL. Alternatively, when IL concentration is varied (1%, 3%, 5%, 7%, and 10%) for 50 mg/mL mucin, it is observed that 1% IL shows similar MSD to that of the mucin control (**Figure 3.5e**). However, after 1%, all concentrations have similar MSD values and are lowest at 3% IL. This signifies that a 3% IL concentration is enough to saturate all the interacting sites of mucin. At 10% IL, slightly reduced MSD is observed, this might be because of the viscosity effects of IL. In order to know the effects of a therapeutic protein on the microrheology of mucin, bovine serum albumin (BSA) is used, which for the sake of brevity has been named as albumin in all the experiments. This happens due to the electrostatic interactions between mucin and albumin, where mucin proteins assemble and form a higher-order mucin-albumin complex. [31] Similar evidence is observed for bulk viscosity, as shown in **Figure 3.6b**. Under low shear rate conditions, the viscosity of the mucin-albumin complex is higher, however, there is no change in viscosity under high shear rate conditions. The experiments indicate

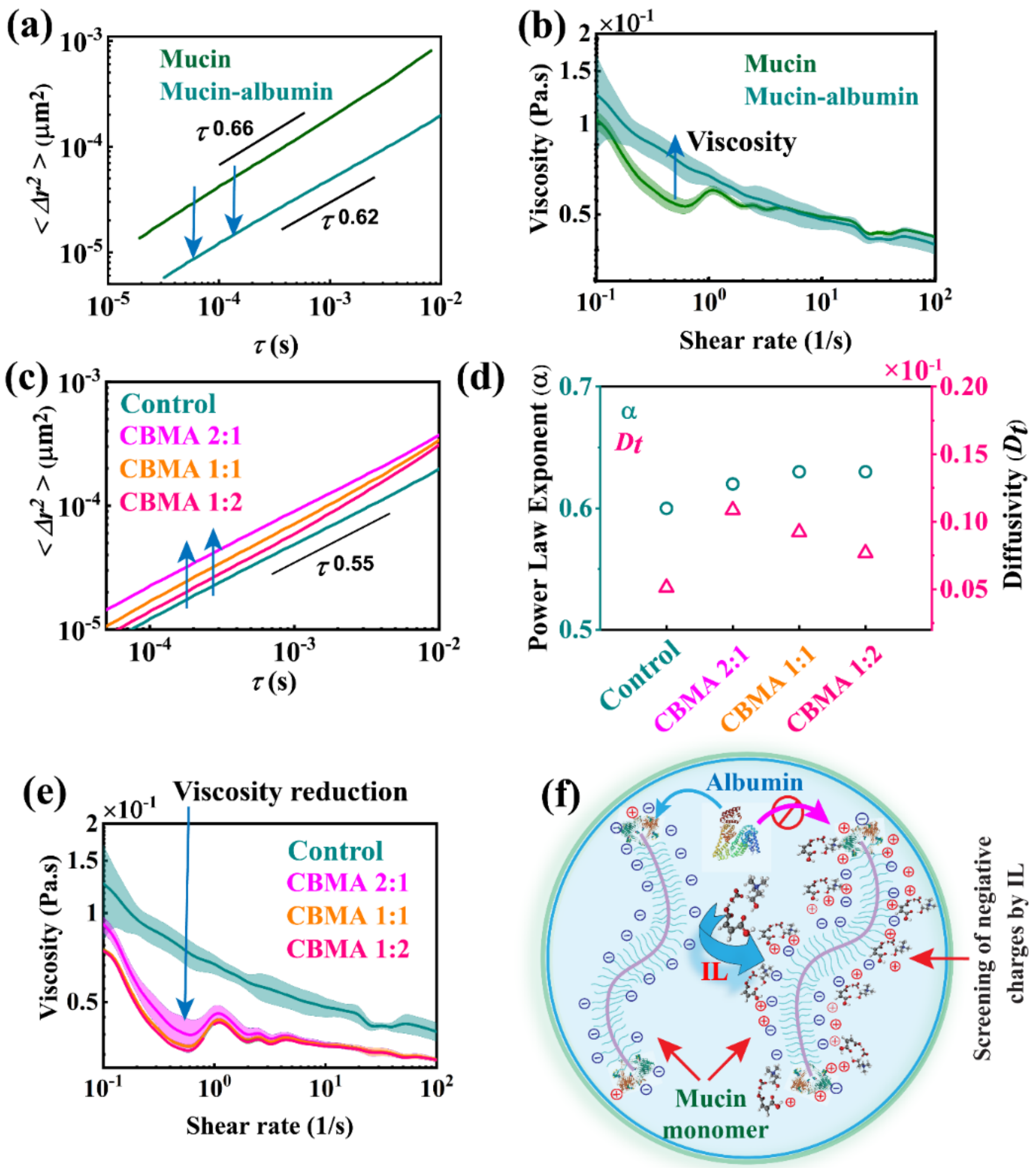

Figure 3.6. (a) Comparison of MSD vs. lag time of Mucin and Mucin-albumin, (b) comparison of Viscosity vs. shear rate of mucin and mucin-albumin, (c) MSD vs. lag time of IL-treated mucin-BSA complex, (d) Power law exponent and diffusivity of Mucin and Mucin-Albumin complex in the presence of IL at 10^{-3}s, (e) Viscosity vs. shear rate of treated and untreated mucin-BSA, (f) schematic illustration of mucin albumin interaction in presence of IL.

weak ionic interactions between mucin and albumin. **Figure 3.6c** shows the MSD vs. lag time plot for mucin-albumin treated with IL, wherein the MSD for all the treated ratios of IL shows an increased value compared to that of the control sample.

More importantly, in this scenario, in contrast to the observations made in the previous two figures, the mucin-albumin treated with 2:1 molar ratio CBMA shows the highest MSD. Further, as compared to the results reported in **Figure 3.6d** for the pristine mucin-albumin sample, the diffusivity of the tracer particle has also increased in the current scenario. This reflects a decrease in the interaction between the mucin and albumin molecules to engender a disassembled mucin hierarchy.

In addition, the bulk rheometer experiment, as shown in **Figure 3.6e**, confirms that at both the low and high shear rates, the viscosity is decreased for all the ratios of IL treatment. This may result from the disentangled mucin structures. The study further elucidates that increasing mucin-albumin concentration with the same IL treatment (3%) leads to an increase in MSD as shown in **Figure 3.7a-c**. In addition, an analysis of the diffusivity ratio between the treated and untreated mucin-albumin demonstrates a two-fold increment in diffusivity at 50 mg/mL followed by a subsequent decrease at 100 mg/mL **(Figure 3.7d)**. The IL treatment improves the diffusivity up to two times at 50 mg/mL but lowers the same at 100 mg/mL. Conversely, increasing the IL concentration (1%, 3%, 5%, 7%, and 10%) while keeping the mucin-albumin at 50 mg/mL shows that, at 3% IL, MSD is the highest as shown in **Figure 3.7e**. A very similar trend has been observed in terms of diffusivity, as shown in **Figure 3.7f**. The highest diffusivity peaks at 3% IL while decreasing at higher IL loading. The results corroborate the fact that ~3% IL is the optimal dose for the treatment of mucin-albumin, where the IL saturates all the interacting sites of mucin as evidenced in the mucin IL section. Concisely, the aforementioned bulk and microrheological studies of IL-treated mucin indicate the change in rheological properties of mucin as well as the mucin-albumin system, which can be extremely useful for the study of the transport of a protein-based drug through the mucus barrier.

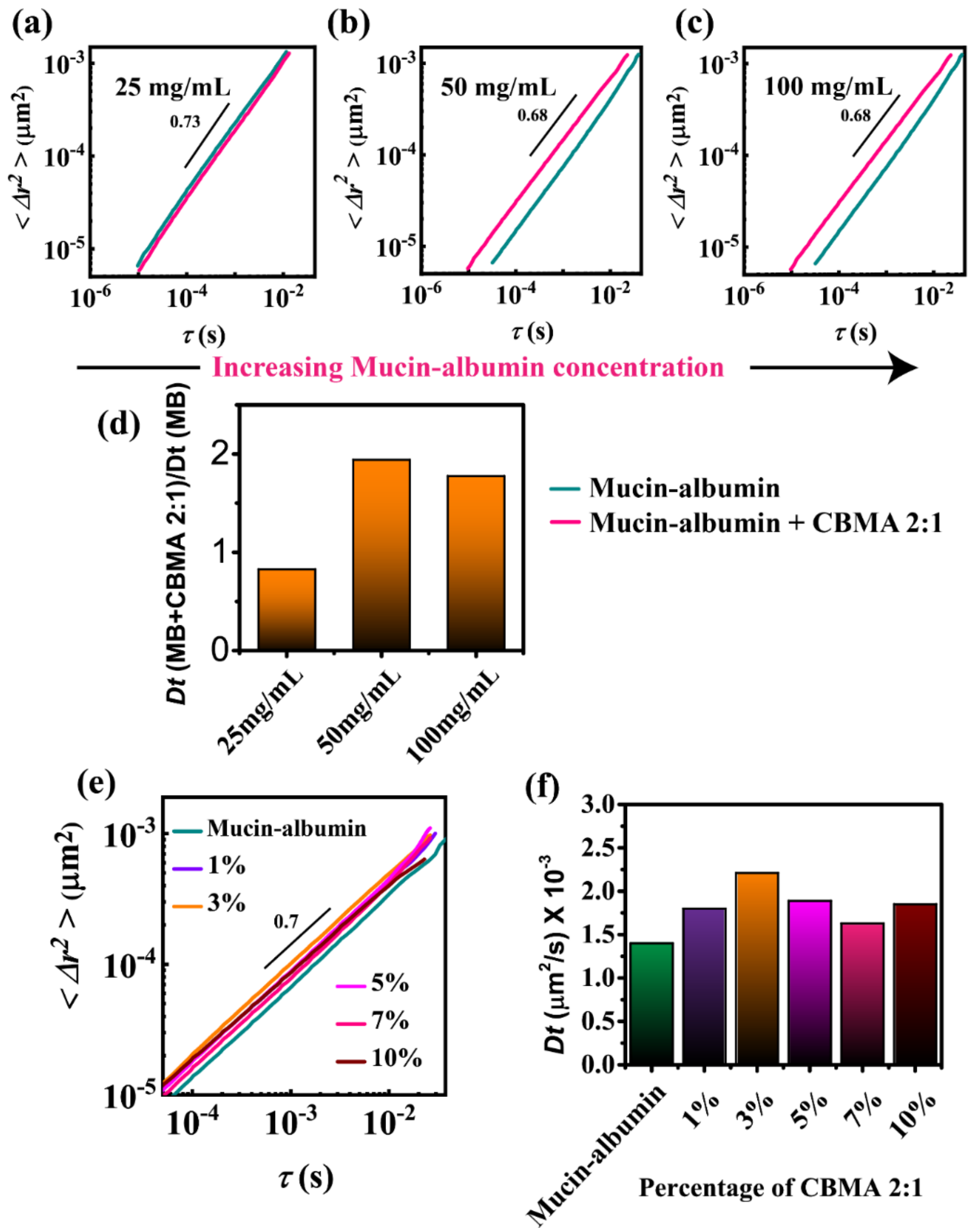

Figure 3.7. MSD at various dosages treatment options for mucin-albumin with CBMA 2:1 are (a) 25 mg/ml, (b) 50 mg/ml, and (c) 100 mg/ml mucin. (d) diffusivity ratio between treated and untreated mucin-albumin. (e) MSD vs. lag time (τ) plot of variation of percentage of CBMA 2:1 on mucin-albumin. (e) Diffusivity of mucin-albumin with different percentage CBMA 2:1 IL.

3.3.3. DFT- Geometry Optimization

Figure 3.8a illustrates the optimized geometries of CBMA (2:1) IL at B3LYP/6-311+G (d,p)-D3BJ method. All the obtained structures represent ground state geometry as confirmed by the non-existence of any imaginary frequency in vibrational 'freq' analysis. The dispersion interactions within the molecules have been accounted for by employing the D3BJ dispersion correction method in conjunction with the DFT calculation. Two choline cations and one maleate (2−) anion are the basis of the IL structure, where an extra component was included from mucin components such as cysteine, N-Acetylgalactosamine (GalNAc), and sialic acid, individually to obtain three separate IL-mucin complexes, as displayed in **Figure 3.8a(i-iii)**. A pair of charged amino acids, arginine, and histidine are also included separately for similar analysis. After examining the optimized geometries, the following important observations can be mentioned: (i) the HBA-HBD structural integrity is intact during the IL-mucin complex formation. The choline-maleate (2−) interaction distances ranged between 2.02 to 2.36 Å for the three mucin systems. In the CBMA (2:1) IL structure, one maleate (2−) ion is in the middle of two choline cations. The interaction distances between these ions (HBA-HBD) obtained a range of 2.02 to 2.09 Å on one end, whereas, on the other end, it was found to be placed at 2.15 to 2.36 Å apart (**Figure 3.8a(i-iii)**). These close interactions suggest a stable and integrated IL structure. Slight relaxation in the structural arrangements of IL components can be observed owing to accommodating the mucin components due to favorable non-bonded interactions. (ii) A significant extent of short-range interactions has been observed in all the IL-mucin systems consisting of cysteine, GalNAc, and sialic acid, respectively, as presented in **Figure 3.8a**. The closest interaction distance of 1.52 Å has been observed between cysteine (maleate 2−) in **Figure 3.8a(i)**, suggesting strong electrostatic as well as H-bonding interaction. Similarly, GalNAc (maleate 2−) and sialic acid (maleate 2−) closest interaction distances are found to be 2.2 Å and 1.71 Å, respectively, as shown in **Figure 3.8a(ii)**. It can be observed that lower electron density sites are partaking in interaction with the sites having electron density-rich groups. The carboxylate parts present in the maleate (2−) ion represent a highly nucleophilic site, whereas, the hydroxyl (−OH) groups present in the components are of electrophilic characteristics, due to the presence of partially positive hydrogen (H) atom adjacent to electronegative oxygen (O) atom. Thus, favorably, H-bonding and electrostatic interactions are observed throughout these systems. The optimized structures provide confirmation of the structural integrity and stability of all the IL-mucin complexes.

In the cysteine domain of the mucus layer, the presence of different charged amino acids can be observed. Further, arginine and histidine are two positively charged amino acids that are found in abundance in the cysteine domain. The presence of such positively charged amino acids can effectively interact with the targeted drug molecules or other incoming proteins, which can affect the mobility or smooth transport of the drug or protein molecules through the mucus layer. To ensure enhanced mobility of the drug molecules in the mucus layer, the ILs are expected to prevent these positively charged amino acids (arginine and histidine) from interacting with the targeted drug molecules.

It can only be achieved through the favorable interaction of arginine and histidine with the IL components before their (arginine and histidine) interaction with the targeted drug molecules. In other words, if the IL components can block the charged amino acids from interacting with the targeted drug molecules, it will enhance the drug transport properties. In order to examine IL's effective interactive properties towards the positively charged amino acids, we have carried out a DFT simulation of CBMA (2:1)-arginine, and CBMA (2:1)-histidine complexes using the same method and basis sets as discussed in this section. The optimized geometries are presented in **Figure 3.8a(i–v)**. The choline cation and maleate (2−) anion interacted with arginine at a distance of 2.08 Å and 1.90 Å, respectively, whereas, in the case of histidine, the respective interaction distances are 1.86 Å and 1.66 Å. The simulations confirm the existence of short-range interaction of a non-covalent nature within the IL-mucin and IL-amino acid systems.

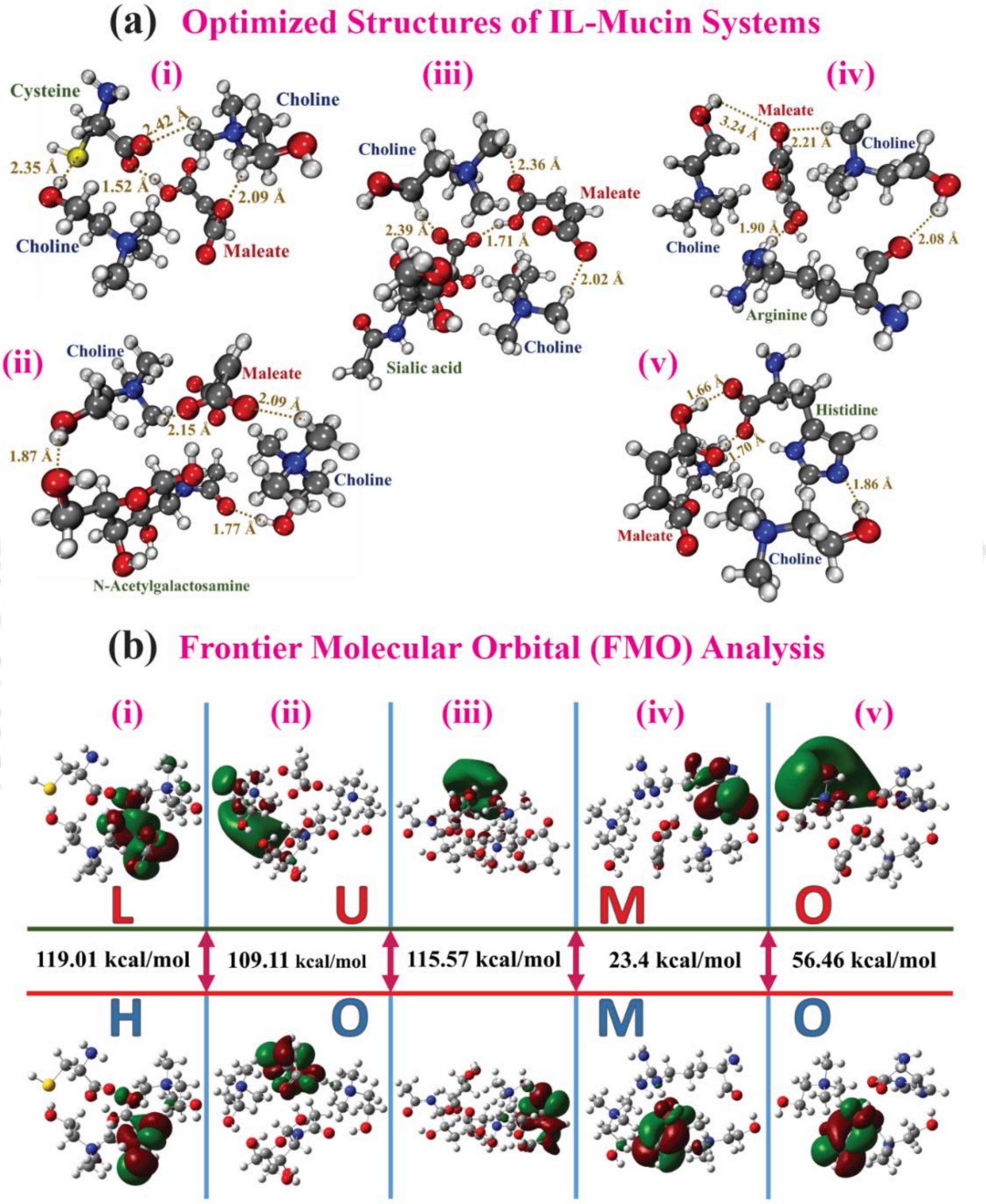

Figure 3.8. (a) Optimized Structures of IL-Mucin Systems, (i) CBMA (2:1)-Cysteine, (ii) CBMA (2:1)-N-Acetylgalactosamine, (iii) CBMA (2:1)-Sialic acid, (iv) CBMA (2:1)-Arginine, and (v) CBMA (2:1)-Histidine at the B3LYP/6-311+G (d,p) level of theory with D3BJ dispersion correction. (Color code: gray- carbon, blue- nitrogen, red- oxygen, and white- hydrogen atom). (b) HOMO−LUMO Energy Gap and iso-surfaces of IL-Mucin Systems, (i) CBMA (2:1)-Cysteine, (ii) CBMA (2:1)-GalNAc, (iii) CBMA (2:1)-Sialic Acid, (iv) CBMA (2:1)-Arginine, and (v) CBMA (2:1)-Histidine. (Lower Structures Display HOMOs and Upper Structures Display LUMOs).

3.3.4. Frontier Molecular Orbital (FMO) Analysis

The chemical stability of all the complexes can be evaluated by the frontier molecular orbital (FMO) analysis, which has been conducted as an effective method to determine acceptor−donor interaction, chemical stability, and reactivity by evaluating the HOMO−LUMO orbital analysis.[49] This section focuses on analyzing the interaction between the HOMO and LUMO species of the IL-mucin complexes and the IL-amino acid systems. HOMO is considered nucleophilic and electron-donating, whereas, the LUMO is electrophilic. The HOMO−LUMO energy gap of a molecule can determine the energy needed to add or remove electrons from the molecule. A higher HOMO−LUMO energy gap corresponds to increased molecular kinetic stability and decreased molecular reactivity.

Figure 3.8b displays the FMO diagrams of the IL-mucin complexes and IL-amino acids, as well as their ground- and excited-state molecular orbitals. The iso-surfaces are displayed using green and red contours to emphasize the positive and negative lobes of the HOMO and LUMO, respectively. The theoretically obtained HOMO-LUMO energy gaps corresponding to different IL-mucin systems are found to be 119.01, 109.11, and 115.57 kcal/mol, respectively, for cysteine, GalNAc, and sialic acid systems, as presented in **Figure 3.8b(i-iii)**. Relatively high HOMO-LUMO gaps confirm the stable nature of the IL-mucin complexes. The smaller size of molecular cysteine associated with a higher degree of HBD and HBA group counts results in denser donor-acceptor interactions compared to sialic acid and GalNAc. Hence, the HOMO-LUMO gap is highest in the case of cysteine suggesting the requirement of higher energy to transit to an excited electronic state. In contrast, GalNAc, though having relatively higher donor-acceptor counts obtained lower charge density due to its larger size. **Figure 3.8b** also shows that IL-cysteine and IL-GalNAc systems present the highest and lowest HOMO-LUMO energy gap values, respectively. In the case of sialic acid, the presence of bulky groups and their large size hinder the orbital overlap interactions. Comparatively lower HOMO-LUMO gap than the other two mucin components suggest relatively weaker donor-acceptor interactions and accordingly lower chemical stability. The chemical stability for the IL-mucin components in terms of the HOMO-LUMO energy gap is in order of CBMA (2:1)-cysteine > CBMA (2:1)-sialic acid > CBMA (2:1)-GalNAc.

As the present study involves two positively charged amino acids (arginine and histidine), the FMO orbitals for the same have been presented in **Figure 3.8b (iv) and (v)**. Relatively low HOMO-LUMO energy gaps have been obtained for arginine (23.4 kcal/mol) and histidine (56.46 kcal/mol) suggesting lower chemical stability as compared to that of IL-mucin systems. This result amplifies that the IL components formulate stronger IL-mucin complexes due to the charge transfer (CT) process and non-covalent interactions, which is the major objective for the selection of this type of IL. The FMO study substantiates the higher selectivity of the IL towards the mucin components as compared to other charged amino acids present in the cysteine domain of the mucus layer. The CT process has been discussed in the upcoming section.

3.3.5. Charge Transfer and Interaction Energy Analysis

In order to have a deeper understanding of the charge transfer (CT) process and delocalization of charge in the IL-mucin systems, the NBO charge has been obtained using the same B3LYP- 6-311+G(d,p) basis set with D3BJ dispersion correction method, as presented in **Figure 3.9a**. The significance of implementing the NBO charge calculation protocol in IL/DES systems in evaluating the localized charge transfer interaction can be validated by some of the previous research works.[32–34] Choline cation obtained partial positive charge (ranging from +1.59e to +1.68e) acting as an HBA, whereas, maleate (2−) acts as HBD attaining negative charge (ranging from −1.29e to −1.6e), as shown in **Figure 3.9a**. This development of charges has been measured after the evolution of CO_2 and H_2O

from the system, keeping only choline cation, maleic acid, and mucin components in the complex system as can be referred to in **Figure 3.9a**. The degree of charge transfer in these IL-mucin complexes is higher as compared to other naturally obtained IL/DES systems due to the superior ionic nature of the IL components and the presence of charged mucin components.

The mucin components cysteine, GalNAc, and sialic acid, acquired partial negative charges in the IL-mucin complex, contrasting with their neutral charge state prior to complex formation. The negative partial charges on mucin components are in the order of GalNAc (−0.084 e) < sialic acid (−0.263 e) < cysteine (−0.3 e). Sialic acid, usually found in the terminal ends of glycoproteins and glycolipids, is present in the carbohydrate side chains of mucin. It is charged in nature due to polar carboxyl and amide functional groups, acting as binding sites for various pathogens and toxins. N-acetylgalactosamine (GalNAc) is another component of the carbohydrate side chain. These two, linked with other components, constitute the carbohydrate side chains attached to the P-T-S backbone of mucin. The side chains being negatively charged as found in the present study, ranging from −0.084 e to −0.263 e, repel each other due to the same-charge repulsion effect to maintain a stable and ordered formation of the mucus layer with complex branching. Thus, it acts as a barrier for external pathogens and toxins, and even for any targeted drug molecule to pass through the layer. However, upon the introduction of the CBMA (2:1) IL, interaction occurs among the IL and mucin components due to favorable charge transfer properties of choline cation and maleic acid moiety.

The choline cation and the active sites of maleic acid align towards the favorable active parts of sialic acid and other mucin component groups present in the carbohydrate side chains, resulting in a complex network of charge interaction. These interactions affect the ordered formation of the side chains as neutralization of the negative charge takes place. As the concentration of the IL increases, the extent of the CT process increases, which gives rise to rapid charge-neutralization of the carbohydrate side chains. As the charge-neutralization occurs, the general structural order of the mucin network gets affected and the formation of small clusters within the mucin network can be observed. This has already been confirmed by the AFM images, as presented previously in **Figure 3.4**. Because of this structural modification of mucin after the IL introduction, the targeted protein molecules face lower resistance to cross through the mucus layer as many sialic acid and GalNAc active sites have already been blocked by the IL components.

Similar phenomena occur in the cysteine domain present at the ends of the P-T-S backbone chain. The cysteine moieties get involved in charged interactions with IL components, as presented in **Figure 3.9a**. The carboxyl group (COOH) and an amine group (NH_2) along with the thiol group ($-CH_2-SH$) present in cysteine favor higher charge interactions with choline and maleate ions. Due to its relatively linear molecular arrangement and greater charge density, cysteine exhibited the strongest charge transfer interaction (−0.3 e) with the ionic liquid (IL) compared to other mucin components. A much lower steric hindrance with higher polarity provides favorable CT interactions, which is evident from the short-range interactions among the molecules in **Figure 3.9a**. Cysteine is found at the end-line of the P-T-S backbone chain of mucin. Higher CT interaction among these components results in the reduction of available binding sites for cysteine toward the targeted drug or protein molecules. Further, as cysteine moieties are involved in cysteine-IL interactions, this results in reduced interaction of cysteine with other mucin components, and collectively, these are responsible for structural disruption of mucin-mucin chains, eventually, making a path for the targeted drugs to move freely through the mucus layer. Mostly, electrostatic and H-bonding interactions are primarily responsible for all these CT interactions.

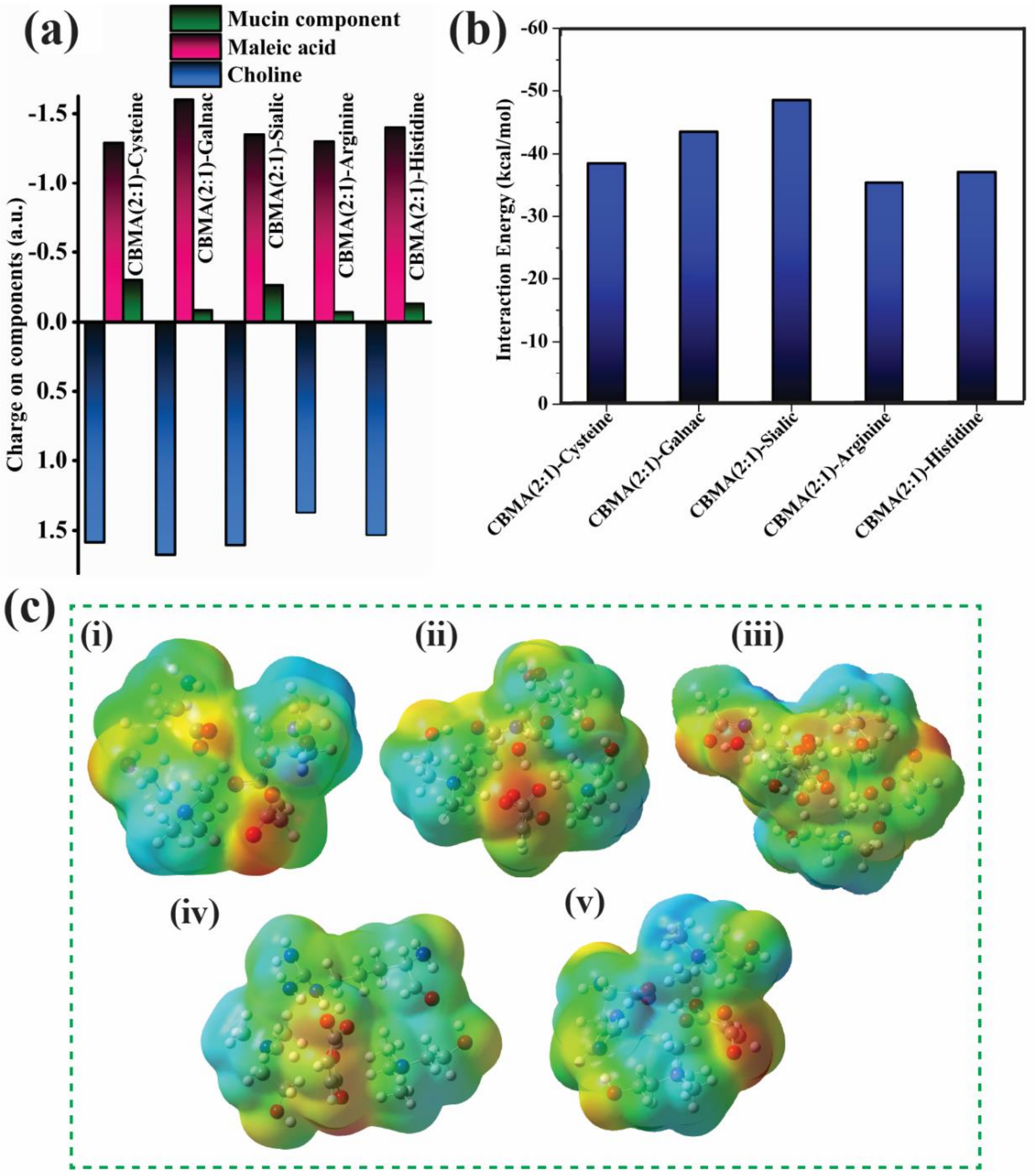

Figure 3.9. (a) Calculated NBO Charges on the Mucin Components (Cysteine, N-acetylgalactosamine, Sialic acid, Arginine, and Histidine) and the DES Components (Choline cation and Maleic acid) for Choline Bicarbonate: Maleic Acid (2:1)-Mucin Systems; (b) Interaction energies for IL-Mucin Systems; CBMA(2:1)-Cysteine, CBMA(2:1)-N-Acetylgalactosamine, CBMA(2:1)-Sialic acid, CBMA(2:1)-Arginine, and CBMA(2:1)-Histidine at the B3LYP/6-311+G (d,p) level of theory with D3BJ dispersion correction. (c) Electrostatic Potential (ESP) Charges for IL-Mucin Systems; (i) CBMA (2:1)-Cysteine, (ii) CBMA (2:1)-N-Acetylgalactosamine, (iii) CBMA (2:1)-Sialic acid, (iv) CBMA (2:1)-Arginine, and (v) CBMA (2:1)-Histidine at the B3LYP/6-311+G (d,p) level of theory with D3BJ dispersion correction.

In order to observe the effect of this IL on other charged amino acids and proteins present in the mucus layer, we have performed similar CT studies for arginine and histidine, which are positively charged entities present in the cysteine domain. For arginine and histidine, the charges are +0.05 e, and +0.07 e, respectively. Arginine and histidine, being positively charged amino acids, interacted with IL components, but to a lesser extent than that of the mucin components as explained earlier. This suggests that the choline bicarbonate: maleic acid (2:1) ionic liquid is extremely effective in having CT interactions with different groups of carbohydrate moieties, proteins, and amino acids to configure a complex network of intermolecular interactions among the constituents. Thus, it can be confirmed that the CT process plays a very crucial role in the formation of stable IL-mucin complexes and in modulating the structural arrangement of the mucus layer for enhanced drug transport.

The term "interaction energy" describes the decrease in system energy that occurs when two or more molecules interact with each other to form a complex.[56] It is possible to compute the interaction energy of IL-mucin complexes using the following equation:

$$\Delta E_{IL-mucin} = E_{IL-mucin} - (E_{IL} + E_{mucin}) + E_{BSSE}. \qquad (3)$$

The variable $E_{IL\text{-}mucin}$ represents the combined energy of the IL-mucin complex. E_{IL} and E_{mucin}, on the other hand, refer to the energies of the individual IL and mucin components, respectively. E_{BSSE} is the Basis Set Superposition Error (BSSE) rectified using the counterpoise approach.[57] **Figure 3.9b** highlights all the computed interaction energy values for IL-mucin systems. Interaction energy offers information on the strength of interactions of the molecules participating in the interaction and the proximity of the atoms engaged in the molecules. The negative interaction energies signify a reduction in the total energies of the final entities created from the original components in the IL-mucin complex formation. The decrease in energy can be attributed to the occurrence of non-bonded contacts, including electrostatic interactions, hydrogen bonding, and van der Waals interactions, among the active chemical groups present in the relevant components.

Interaction energies of IL-mucin complexes are higher for sialic acid (−48.52 kcal/mol), GalNAc (−43.51 kcal/mol), and cysteine (−38.49 kcal/mol), as presented in **Figure 3.9b**. The results also suggest that arginine (−35.45 kcal/mol) and histidine (−37.12 kcal/mol) have slightly lower energies. Multiple close-range interactions are responsible for the larger negative value of interaction energy. The sialic acid showed higher compactness of the structural arrangement despite being a bulkier group because of the favorable binding site affinity in terms of non-bonded interactions within a range of 1.71 to 2.39 Å. The integrity of the complexes depends upon the strength of the interactions. A possible hydrogen bonding interaction length is found to be 1.77 Å in the case of GalNAc, whereas it is 2.09 Å in the case of cysteine. That can explain the order of the interaction strength as obtained in our study. On the other hand, arginine and histidine further confirm favorable interaction between IL and mucin components.

Following this, electrostatic potential (ESP) charges are plotted along the surface of the molecules for the visualization of the surface charge densities of the different regions in the IL-mucin systems, as displayed in **Figure 3.9c**. The red-colored surface contours illustrate higher electron density regions or the presence of negative potential charged active functional groups, whereas, blue regions are viewed as having positive partial charges or lower electron densities. The green-colored contours demonstrate neutral parts. From the contour plots, the charge delocalization can be witnessed clearly around the components of ILs and mucin. Any external molecule, e.g. active drugs or proteins, approaching the IL-mucin complexes can have charged interactions with specific active sites based on the effective partial charges developed in the molecule. **Figures 3.9c (i-iii)** indicate various active regions in mucin components that are associated with charged interactions with the complementary regions in the mucin components (cysteine, GalNAc, and sialic acid). This result can be clubbed with the findings of charge transfer (CT) analysis with NBO charges. The results confirm that the CT process is very crucial in this type of IL system as they are involved in intermolecular non-bonded interactions with mucin as well as other amino acid systems.

3.3.6. Noncovalent Interaction Analysis

Apart from the CT analysis, to gain further insight into the system, we also have performed the noncovalent interaction (NCI) analysis. For this purpose, Contreras-Garci´a and Johnson's [51,58,59] framework has been put into practice, which follows the following equation for the "reduced density gradient" (RDG) analysis,

$$\mathrm{RDG} = \frac{1}{2(3\pi^2)^{1/3}} \frac{|\nabla\rho|}{\rho^{4/3}}. \qquad (4)$$

The method relies on examining the distribution of electron densities in regions with low gradient values and low electron densities. The RDG scatter graph is constructed based on the product of electron density (ρ) and the sign of the electron density Hessian second eigenvalue [sign(λ_2)ρ]. Such NCI analysis may detect and quantify several types of weak interactions, including hydrogen bonding, van der Waals, and dispersion interactions. **Figure 3.10** shows the different NCI plots along with the respective RDG graph for the IL-mucin systems as well as IL-amino acid systems. Distinctly colored spikes in RDG plot correspond to particular types of interactions: blue represents H-bonds or halogen bonds (λ_2 < 0), green represents van der Waals (vdW) or dispersion interactions (λ_2 > 0), and red represents steric effects resulting from ring or cage formation (λ_2 > 0).

In the NCI plot, blue-colored regions represent strong, attractive hydrogen/halogen bonds and electrostatic interactions, red-colored regions represent a strong repulsion effect due to

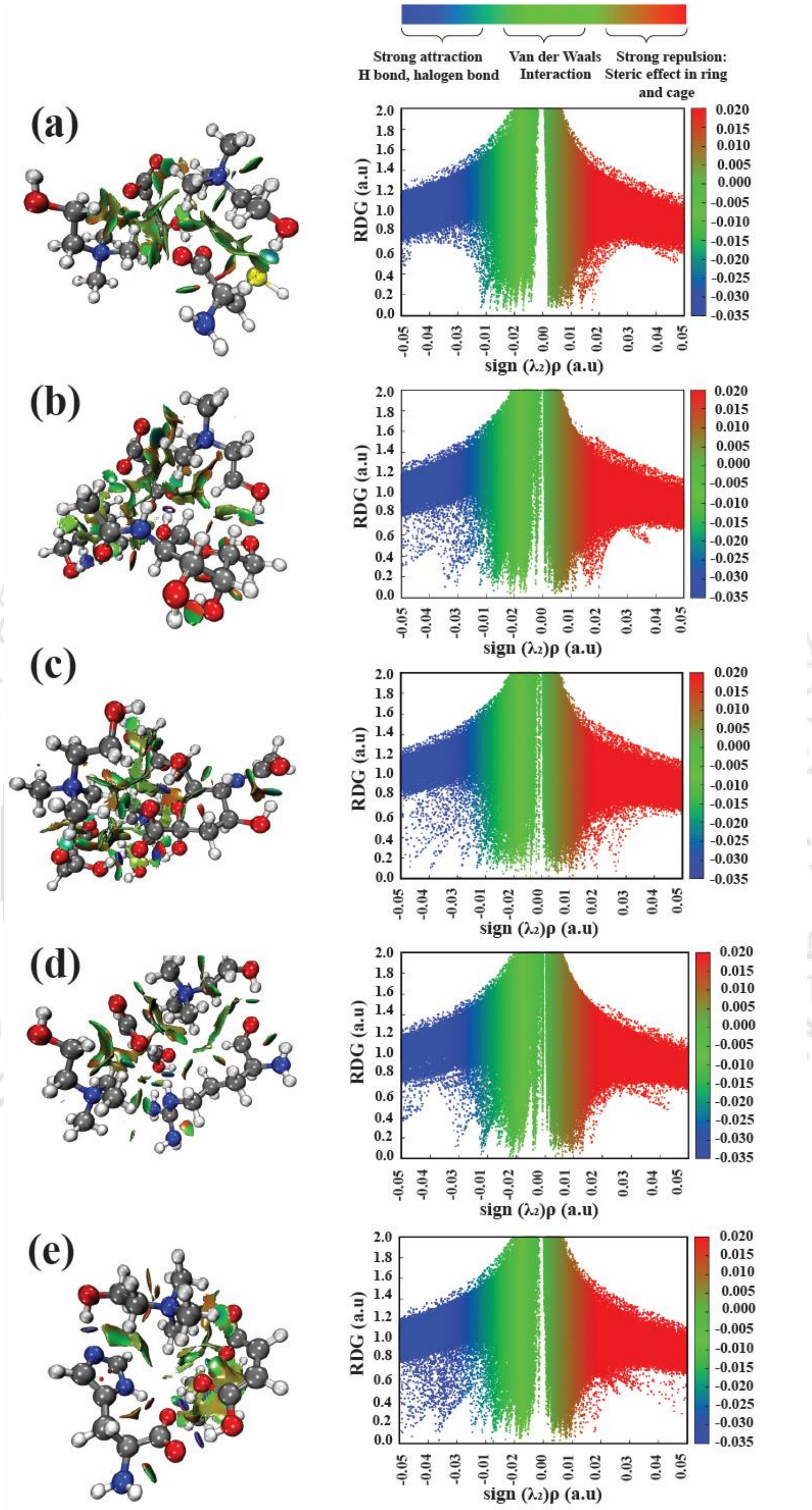

Figure 3.10. RDG isosurfaces and scatter graphs of RDG for (a) CBMA (2:1)-Cysteine, (b) CBMA (2:1)-GalNAc, (c) CBMA (2:1)-Sialic Acid, (d) CBMA (2:1)-Arginine, and (e) CBMA (2:1)-Histidine at the B3LYP/6-311+G (d,p) level of theory with D3BJ dispersion correction.

non-bonded overlap, and green or transition regions represent vdW interactions, dispersion interaction, dipole−dipole interaction, etc. **Figure 3.10a-c** shows the presence of hydrogen bonding and dispersion interactions in the form of vdW interactions observed for all the IL-mucin systems. In the case of CBMA (2:1)-cysteine NCI/RDG plots, one can observe a greater number of RDG spikes present between −0.01 and −0.025 a.u. This corroborates the electrostatic interactions developed in cysteine and IL molecules. Along with electrostatic, dispersion interactions are also found to be dominant in the cysteine system. No significant spikes in the region between −0.03 and −0.05 a.u. can be observed suggesting a lack of hydrogen bonding. A similar result can be observed from the lack of blue flakes in the NCI plot in **Figure 3.10a**. The reason for this lack of hydrogen bonding in the IL-cysteine system could be explained by the lesser electronegativity of the thiol (−SH) group in cysteine moiety.

However, the presence of other active groups in cysteine ensures effective dispersion and vdW interactions. The green flakes present in the left side diagram of **Figure 3.10a** indicate the same. The figure indicates that multiple hydroxyl (−OH) and carboxyl (−COOH) groups present in GalNAc as well as sialic acid play a crucial role in obtaining hydrogen bonding and electrostatic interactions as evident from the RDG spikes present between −0.02 and −0.05 a.u., as shown in **Figure 3.10b-c**. In contrast, the presence of large bulky groups in these two systems (GalNAc and sialic acid) have developed multiple red spikes due to steric effect in the region between +0.01 and +0.03 a.u., which is absent in the case of cysteine system due to its linear structural arrangement. The contribution from the IL structure (HBA-HBD interaction) in the form of hydrogen bonding, electrostatic, and vdW interactions are also associated with the present NCI/RDG interaction regions. Overall, IL-mucin non-covalent interactions play a significant role in the formulation of strong IL-mucin complexes. similar involvement of different non-covalent interactions has been observed for the systems containing the charged amino acids (arginine and histidine), as presented in **Figure 3.10d-e**, which confirmed increased closed-shell interaction between the components. Histidine exhibits multiple blue spikes in the RDG plot between −0.03 and −0.05 a.u. suggesting the presence of hydrogen bonding due to electronegative elements within the system.

3.3.7. Model Mucus-on-a-Chip

In order to assess the effects of IL on the diffusion of therapeutic protein-based drugs, we conducted a diffusion experiment using two distinct microfluidic channels. The first setup has been a T-shaped channel with a pair of inlets and one outlet, which has been fabricated using conventional replica molding, as mentioned in the experimental section and shown in **Figure 3.11a**.

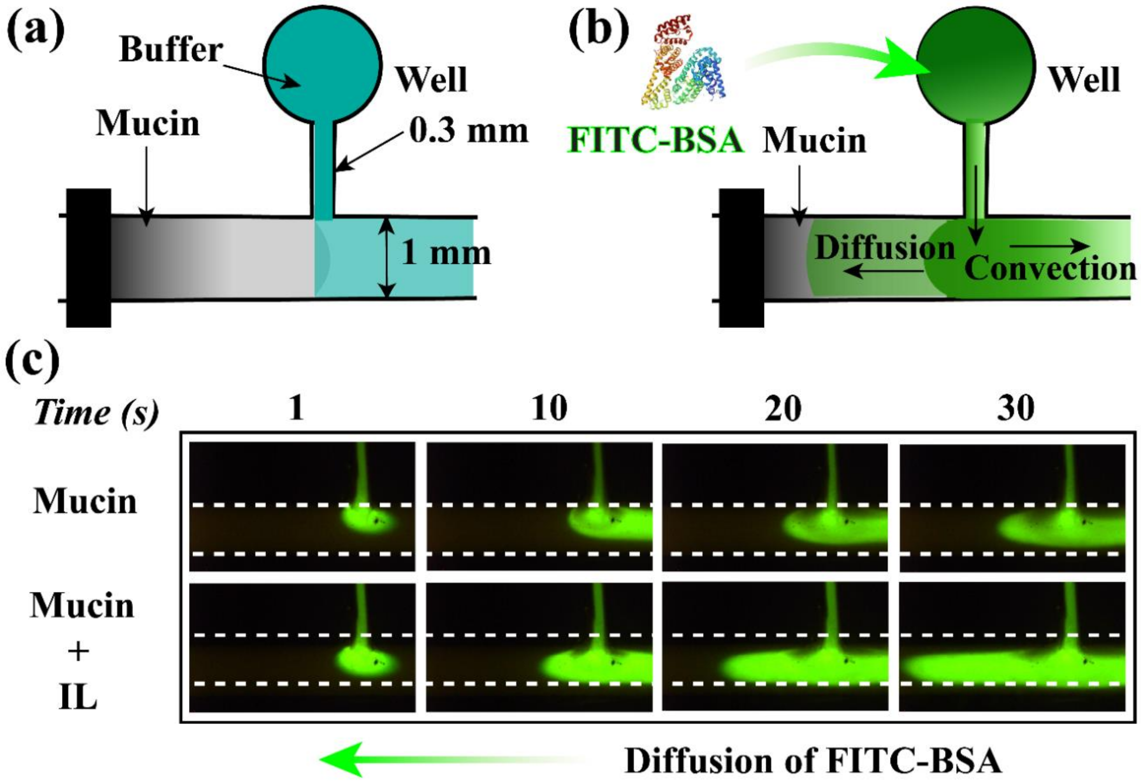

Figure 3.11. (a) Top view of mucin-filled T microchannel, (b) Top view of FITC-BSA filled well which flows to the main channel, (c) diffusion of FITC-BSA through the mucin-filled main channel over the period.

In order to know the diffusion of a model therapeutic protein in a mucus layer, BSA has been considered as a model therapeutic drug. For this purpose, initially, BSA has been labeled with FITC dye to make it visible under a fluorescent microscope.

Initially, the mucin solution has been filled in the main (1 mm) channel in such a manner that it only fills up to the side channel (0.3 mm), while 10 mM phosphate buffer is filled in the remaining part as shown in **Figure 3.11a**. following this, 20 µl of BSA solution is added to the well (diameter of 2 mm) and observed for a few minutes. As a result of capillary action and gravity, the BSA solution (green) passes through the void region of the main channel while a part diffuses in the mucin-filled region, as shown in **Figure 3.11b.** The same experiments have been repeated for IL-treated mucin also. The spatiotemporal microscopic images shown in **Figure 3.11c** suggest that the IL-treated mucin shows a faster diffusion as compared to the untreated one. Interestingly, it has been observed that the the diffusion of FITC-BSA in the IL treated mucin is up to a distance of ~ 3 mm (measure from the start of the side channel to the left of the main channel) compared to control mucin which is about 1 mm after 30 minutes.

Following this, to emulate the exact intestinal conditions, a mucus-on-a-chip (MOAC) prototype has been fabricated using photolithography and replica molding techniques, as discussed previously in the experimental section and illustrated in **Figure 3.12a-b**. For this experiment, a partially purified mucin is extracted directly from the pig intestine. Thereafter, γ-globulin is used as a model antibody, which is labeled with the FITC dye to track the diffusion under the fluorescence microscope. The FITC-labelled antibody has been treated with IL with a ratio of 1:5 v/v and the untreated antibody is taken as control.

Figure 3.12c shows the instrumental setup of mucus on a chip device under a fluorescence microscope with an excitation wavelength of 495 nm (blue light). Before the experiment, the partially purified native mucin is reconstituted with 10 mM PBS buffer and injected into the mucus channel with a flow rate of 0.5 µL/min with the help of a syringe pump. Subsequently, once it is filled, the pump is stopped and both the inlet and outlet of the mucus channel are blocked by a stopper and allowed to settle the mucins for 15 min, as shown in **Figure 3.12d** (observed under brightfield).

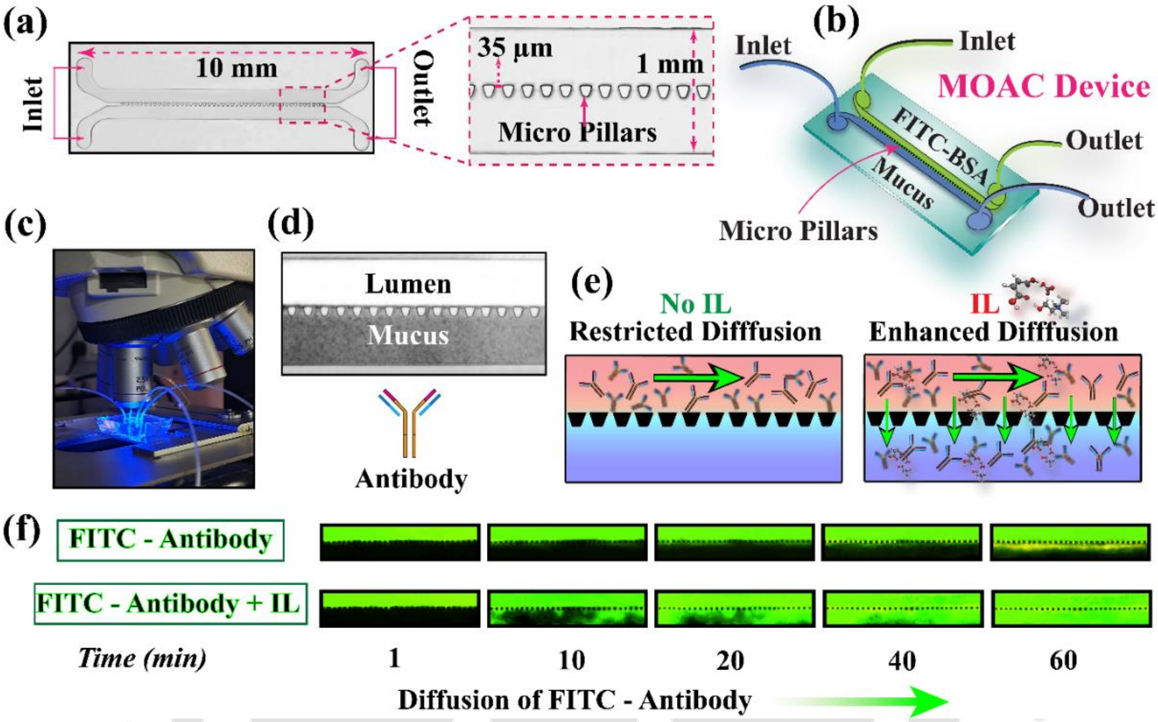

Figure 3.12. (a) Top view of a pillars-embedded microchannel, (b) Schematic diagram of a Mucus-on-a-Chip device, (c) experimental setup of the microchannel, (d) mucin-filled microchannel in the mucus channel with schematics, (e) schematic diagram of diffusion of antibodies in the absence or presence of CBMA 2:1 IL through mucus channel. (f) spatiotemporal evaluation of antibody diffusion in the absence or presence of CBMA 2:1 through the mucus channel.

The image also shows how this prototype emulates a lumen/mucus thin-layer assemblage separated by an array of micropillars. After that, the FITC- antibody passes through the lumen channel with a flow rate of 5 µL/min maintained by a syringe pump, and images are taken every 2 s in a time series mode for 60 min.

Figure 3.12f shows that for untreated antibodies, the diffusion has been restricted only to the pillars even after 40 min, resulting in a restricted diffusion owing to the binding of antibodies with mucin molecules.[31] In comparison, in the case of antibodies treated with IL, there is the diffusion of antibodies into the mucus channel just after 1 min, and over a certain period of time, it completely diffuses to the mucus channel. This indicates that IL interferes with the binding of antibodies to the mucin molecules to increase the diffusivity of antibodies. Overall, the diffusion experiments establish that the diffusion of both albumin and antibody is enhanced in the presence of IL. Furthermore, to see the morphological changes of extracted mucin in the presence of CBMA 2:1, FESEM is utilized. The mucin obtained from the native source has a network-like arrangement, as depicted in **Figure 3.13a-b**. Conversely, when exposed to CBMA 2:1, the mucin undergoes structural degradation and forms aggregates (**Figure 3.13c-d**). This observation aligns with the morphological analysis of commercially pure mucin using Atomic Force Microscopy (AFM) as mentioned in section A of this chapter.

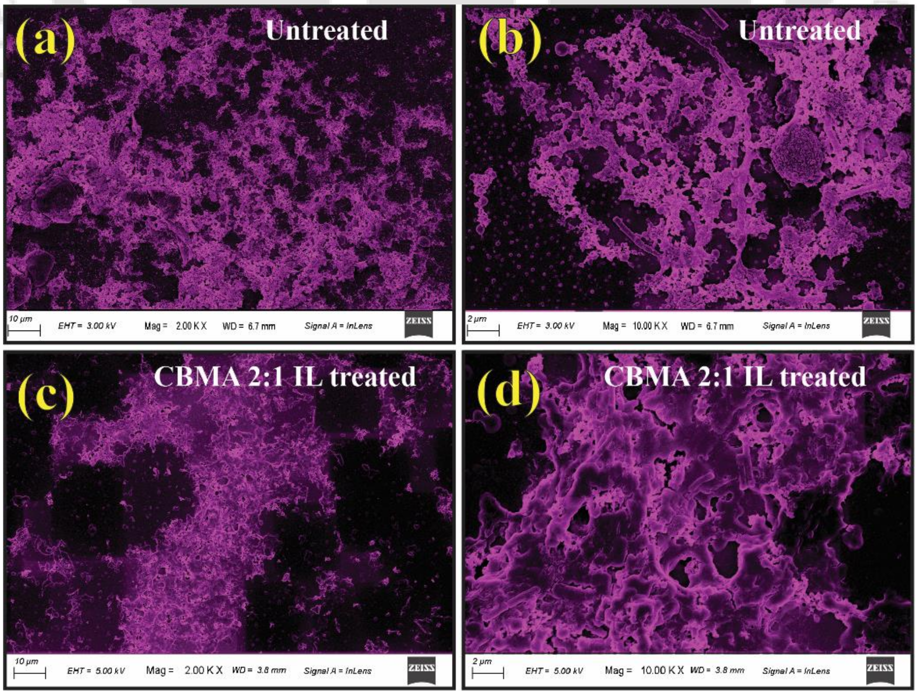

Figure 3.13. FESEM images of partially purified pig mucin untreated (a,b) and CBMA 2:1 treated (c,d). The false magenta color is used using ImageJ software.

3.3.8. Mechanism of IL-treated Mucin Arrangement

All the experiments and computations reported so far uncover some striking observations, which have been summarized in this section with the help of the schematic diagram in **Figure 3.14**. Firstly, within the mucus layer, the P-T-S backbones of mucin align themselves in a homogeneous structural arrangement, as shown in **Figure 3.14a**. The side chains in the P-T-S backbone consisting of sialic acid, GalNAc, galactose, etc., also align themselves around the same while the side chains from two adjacent P-T-S backbones remain stable because of electrostatic repulsion. On the other hand, the cysteine domain present at the end of each P-T-S backbone contributes to the adhesive and swellable properties of the mucin with subsequent polymerization to form long linear oligomers via intra-disulfide bonds. The cysteine domain provides a linear connection between the P-T-S backbone through polymerization whereas the charged amino acids such as arginine or histidine help in charge transfer. Importantly, the water molecules are present throughout the mucus layer to form a homogeneous dispersed phase that imparts mobility to the system. The mucin constitutes an ordered structural formation due to all these components and their interactions to form the aforementioned interconnected networks. However, in the case of CBMA (2:1) IL-treated mucin, the uniformity in the presence of water molecules is disrupted due to the development of IL-mucin complexes within the P-T-S backbone in the mucus layer (**Figure 3.14b**). As a result of these complexes, water molecules present within the regions between two adjacent P-T-S branches transport out due to the ‘salting out’ effect, resulting in the P-T-S branches coming closer to each other. Additionally, in the cysteine domain, IL-cysteine complexes are formed, along with the interaction of IL with other charged amino acids (**Figure 3.14c**). This enhanced IL-cysteine interaction disrupts the connectivity between the cysteine domains of two individual mucin monomers. With the introduction of CBMA 2:1, the IL moiety places itself within the carboxylic side chains of two adjacent P-T-S backbones and forms IL-sialic acid, IL-GalNAc complex at both the ends of IL due to, (i) superior charge transfer behavior, and (ii) presence of suitable active polar groups within the mucin components. The QC structural analysis confirms that these IL-mucin interactions take place at a short-range potential (~1.5 to 2.2 Å), which yields ‘charge shielding’ by blocking the repulsive forces acting among the carboxylic side chains which in turn helps in effectively pulling the P-T-S backbones along with it, thus reduction of the inter-branch distances between the adjacent P-T-S backbones is witnessed, as shown in **Figure 3.14d-e**.

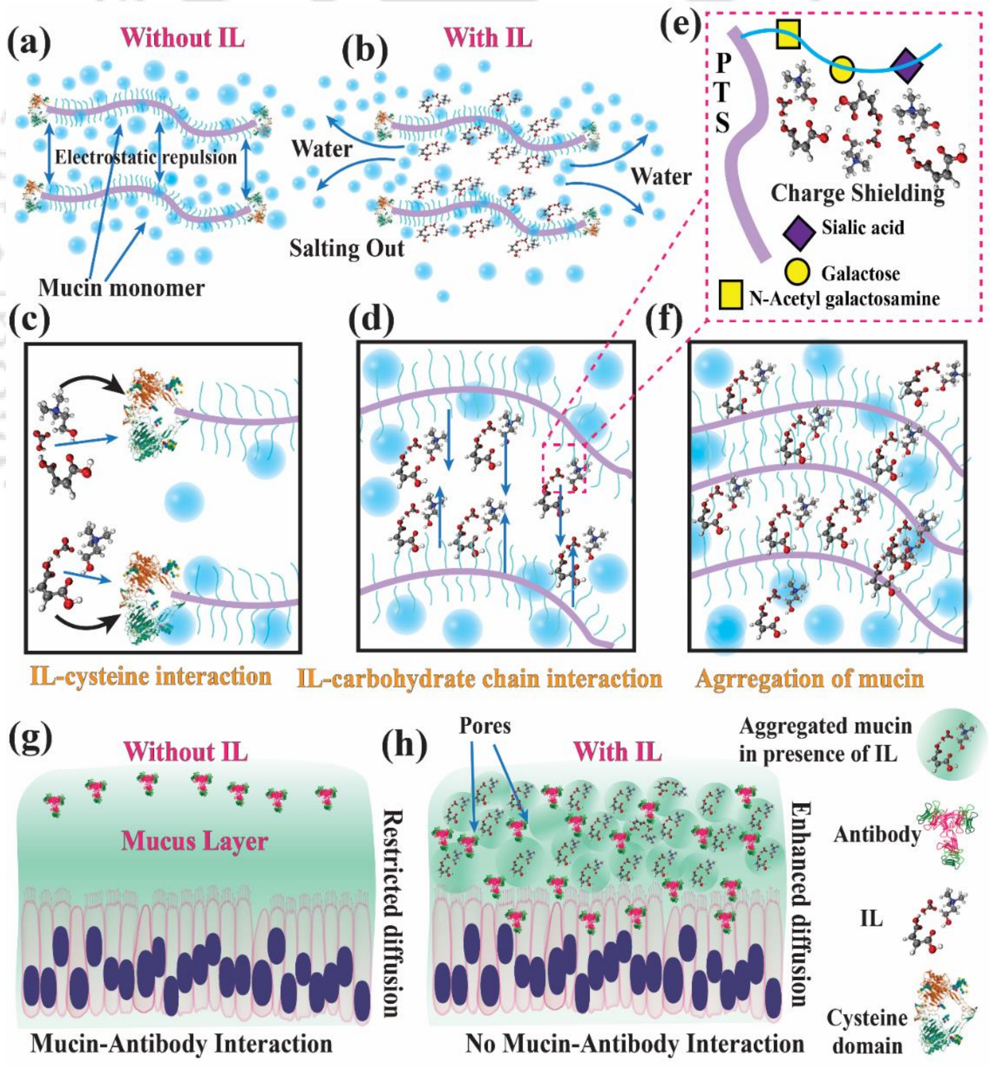

Figure 3.14. A schematic diagram of IL-mucin interaction resulted in enhanced diffusion of antibodies. (a) the homogenous structural arrangement of mucin monomers, (b) disruption of water mucin interaction in presence of IL, (c) IL complexation with cysteine

domain of mucin resulted in disruption of chain elongation as well as mucin-nonmucin protein interaction, (d) Charge shielding of carbohydrate chains by IL, (e) Enlarged view of IL complexation with the carbohydrate chain components, (f) The overall interaction resulted in aggregation of mucin, (g) Restricted diffusion of antibodies through mucus layer without IL, and (h) Enhanced diffusion of antibodies through mucus layer in presence of IL.

The introduction of IL in the system leads to the aggregation of mucin chains at different patches across the mucus layer, due to the combined effects of 'charge shielding', 'salting out of water molecules', and dissociation of P-T-S backbone chains. (**Figure 3.14f**). It may be noted here that, due to the aggregation in the mucus layer while dewatering the aggregated IL-treated mucus layer, a small but definite proportion of pathways is expected to emerge in the interstitial spaces around the aggregates, which is not present in the case of pure mucus layer where no IL is introduced (**Figure 3.14g**). These pathways allow and enhance the diffusion and transport of targeted proteins, antibodies, and drugs through the mucus layer to achieve enhanced effective drug delivery (**Figure 3.14h**).

3.4. Conclusions

The chapter demonstrates the fundamental process by which the CBMA-based IL interacts with mucin, as revealed by both experimental and simulation investigations. The study suggests that mucin interacts and binds electrostatically with the proteins due to the presence of multiple charged groups, forming a compact hierarchical structure. When albumin is considered a model protein-based drug, upon the incorporation of albumin into the mucin solution, mucin interacts with albumin, increasing the viscosity due to favorable electrostatic interactions. In this context, the incorporation of CBMA-based ionic liquid has increased the diffusivity of the probed particles due to the unwinding of mucin assembly tailored by albumin. Conversely, in the case of pristine mucin solution, the incorporation of

IL leads to mucin aggregation, as evident from the microrheological analysis. As a result of mucin aggregates, the probed particles' MSD as well as diffusivity has drastically decreased.

A similar trend has been observed from the rheometer study, where the viscosity is increased in the entire range of frequency, which indicates the aggregation of mucin. Furthermore, AFM analysis confirms the alteration of native mucin structures. This can be understood that increased localized aggregation also helps in forming void pores which is beneficial for the diffusion of small molecules. The QC analysis substantiates the influence of charge transfer among the IL-mucin components where interactions take place at a short-range potential (~1.5 to 2.2 Å). Rapid charge neutralization of the mucin side chains (charge shielding) can be observed with the increase in IL concentration. The strongly formed complexes, having interaction energies ranging from −38.49 to −48.52 kcal/mol, confirm the superior IL-mucin non-bonded interactions (range: 1.71 to 2.36 Å). These interactions in the form of hydrogen bonding, electrostatic, and dispersion, have been confirmed through NCI analysis for the IL-cysteine, IL-sialic acid, and IL-GalNAc complexes. The ‘charge shielding’, dissociation of P-T-S backbone chains, enhanced IL-mucin interaction, and overall stability of the systems have been substantiated through the QC investigation and experimental findings.

Furthermore, in order to correlate the results obtained by both microrheological and computational investigations with the actual intestine conditions, we fabricated a T-shaped microchannel and studied the diffusion of FITC-labeled albumin in the simulated mucus layer. It has been confirmed that ionic liquid has altered the networks of mucin polymer in the cysteine and sialic acid regions and hence less affinity of mucins for the model therapeutic drug i.e. albumin has been observed, which resulted in increased diffusivity. Interestingly, the mucus-on-chip device aids in elucidating the diffusion behavior of FITC-labeled antibodies within partially purified mucin, demonstrating the enhanced diffusive properties of antibodies in the presence of ionic liquid (IL). This experimental setup serves to mimic the intestinal mucus barrier and monitor the diffusion of FITC-labeled antibodies. The amplified diffusion of antibodies facilitated by the IL environment substantiates the findings. Concisely, the investigation sheds light on the interaction between choline bicarbonate-maleic acid-based ionic liquid and mucin polymer, offering valuable molecular-level insights for the development of oral and site-specific therapeutic drugs.

References

(1) Ensign, L. M.; Cone, R.; Hanes, J. Oral Drug Delivery with Polymeric Nanoparticles: The Gastrointestinal Mucus Barriers. *Adv. Drug Deliv. Rev.* **2012**, *64* (6), 557–570. https://doi.org/10.1016/j.addr.2011.12.009.

(2) Maisel, K.; Ensign, L.; Reddy, M.; Cone, R.; Hanes, J. Effect of Surface Chemistry on Nanoparticle Interaction with Gastrointestinal Mucus and Distribution in the Gastrointestinal Tract Following Oral and Rectal Administration in the Mouse. *J. Control. release Off. J. Control. Release Soc.* **2015**, *197*, 48–57. https://doi.org/10.1016/j.jconrel.2014.10.026.

(3) Shah, R. B.; Patel, M.; Maahs, D. M.; Shah, V. N. Insulin Delivery Methods: Past, Present and Future. *Int. J. Pharm. Investig.* **2016**, *6* (1), 1–9. https://doi.org/10.4103/2230-973X.176456.

(4) Mowat, C.; Cole, A.; Windsor, A.; Ahmad, T.; Arnott, I.; Driscoll, R.; Mitton, S.; Orchard, T.; Rutter, M.; Younge, L.; Lees, C.; Ho, G.-T.; Satsangi, J.; Bloom, S. Guidelines for the Management of Inflammatory Bowel Disease in Adults. *Gut* **2011**, *60* (5), 571–607. https://doi.org/10.1136/gut.2010.224154.

(5) Chiu, M. L.; Gilliland, G. L. Engineering Antibody Therapeutics. *Curr. Opin. Struct. Biol.* **2016**, *38*, 163–173. https://doi.org/10.1016/j.sbi.2016.07.012.

(6) Buckley, S. T.; Bækdal, T. A.; Vegge, A.; Maarbjerg, S. J.; Pyke, C.; Ahnfelt-Rønne, J.; Madsen, K. G.; Schéele, S. G.; Alanentalo, T.; Kirk, R. K.; Pedersen, B. L.; Skyggebjerg, R. B.; Benie, A. J.; Strauss, H. M.; Wahlund, P.-O.; Bjerregaard, S.; Farkas, E.; Fekete, C.; Søndergaard, F. L.; Borregaard, J.; Hartoft-Nielsen, M.-L.; Knudsen, L. B. Transcellular Stomach Absorption of a Derivatized Glucagon-like Peptide-1 Receptor Agonist. *Sci. Transl. Med.* **2018**, *10* (467). https://doi.org/10.1126/scitranslmed.aar7047.

(7) Durán-Lobato, M.; Niu, Z.; Alonso, M. J. Oral Delivery of Biologics for Precision Medicine. *Adv. Mater.* **2020**, *32* (13), e1901935. https://doi.org/10.1002/adma.201901935.

(8) Bansil, R.; Stanley, E.; Thomas LaMont, J. Mucin Biophysics. *Annu. Rev. Physiol.* **1995**, *57* (February), 635–657. https://doi.org/10.1146/annurev.ph.57.030195.003223.

(9) Bansil, R.; Turner, B. S. The Biology of Mucus: Composition, Synthesis and Organization. *Adv. Drug Deliv. Rev.* **2018**, *124,* 3–15. https://doi.org/10.1016/j.addr.2017.09.023.

(10) Celli, J. P.; Turner, B. S.; Afdhal, N. H.; Ewoldt, R. H.; McKinley, G. H.; Bansil, R.; Erramilli, S.; Erramilli, S. Rheology of Gastric Mucin Exhibits a PH-Dependent Sol-Gel Transition. *Biomacromolecules* **2007**, *8* (5), 1580–1586. https://doi.org/10.1021/bm0609691.

(11) Leal, J.; Smyth, H. D. C.; Ghosh, D. Physicochemical Properties of Mucus and Their Impact on Transmucosal Drug Delivery. *International Journal of Pharmaceutics*. Elsevier B.V. October 30, 2017, pp 555–572. https://doi.org/10.1016/j.ijpharm.2017.09.018.

(12) Linden, S. K.; Sutton, P.; Karlsson, N. G.; Korolik, V.; McGuckin, M. A. Mucins in the Mucosal Barrier to Infection. *Mucosal Immunol.* **2008**, *1* (3), 183–197. https://doi.org/10.1038/mi.2008.5.

(13) Parlato, R. M.; Greco, F.; Maffettone, P. L.; Larobina, D. Effect of PH on the Viscoelastic Properties of Pig Gastric Mucus. *J. Mech. Behav. Biomed. Mater.* **2019**, *98* (June), 195–199. https://doi.org/10.1016/j.jmbbm.2019.06.008.

(14) Wagner, C. E.; Krupkin, M.; Smith-Dupont, K. B.; Wu, C. M.; Bustos, N. A.; Witten, J.; Ribbeck, K. Comparison of Physicochemical Properties of Native Mucus and Reconstituted Mucin Gels. *Biomacromolecules* **2023**, *24* (2), 628–639. https://doi.org/10.1021/acs.biomac.2c01016.

(15) Lieleg, O.; Ribbeck, K. Biological Hydrogels as Selective Diffusion Barriers. *Trends Cell Biol.* **2011**, *21* (9), 543–551. https://doi.org/10.1016/j.tcb.2011.06.002.

(16) Smith-Dupont, K. B.; Wagner, C. E.; Witten, J.; Conroy, K.; Rudoltz, H.; Pagidas, K.; Snegovskikh, V.; House, M.; Ribbeck, K. Probing the Potential of Mucus Permeability to Signify Preterm Birth Risk. *Sci. Rep.* **2017**, *7* (1), 10302. https://doi.org/10.1038/s41598-017-08057-z.

(17) Sun, X.; Abioye, R. O.; Okagu, O. D.; Udenigwe, C. C. Peptide-Mucin Binding and Biosimilar Mucus-Permeating Properties. *Gels (Basel, Switzerland)* **2021**, *8* (1). https://doi.org/10.3390/gels8010001.

(18) Li, L. D.; Crouzier, T.; Sarkar, A.; Dunphy, L.; Han, J.; Ribbeck, K. Spatial Configuration and Composition of Charge Modulates Transport into a Mucin Hydrogel Barrier. *Biophys. J.* **2013**, *105* (6), 1357–1365. https://doi.org/10.1016/j.bpj.2013.07.050.

(19) Shi, Y.; Zhao, Z.; Gao, Y.; Pan, D. C.; Salinas, A. K.; Tanner, E. E. L.; Guo, J.; Mitragotri, S. Oral Delivery of Sorafenib through Spontaneous Formation of Ionic Liquid Nanocomplexes. *J. Control. release Off. J. Control. Release Soc.* **2020**, *322,* 602–609. https://doi.org/10.1016/j.jconrel.2020.03.018.

(20) Vaidya, A.; Mitragotri, S. Ionic Liquid-Mediated Delivery of Insulin to Buccal Mucosa. *J. Control. Release* **2020**, *327,* 26—34. https://doi.org/10.1016/j.jconrel.2020.07.037.

(21) Tanner, E. E. L.; Ibsen, K. N.; Mitragotri, S. Transdermal Insulin Delivery Using Choline-Based Ionic Liquids (CAGE). *J. Control. release Off. J. Control. Release*

Soc. **2018**, *286*, 137–144. https://doi.org/10.1016/j.jconrel.2018.07.029.

(22) Introduction: Ionic Liquids. *Chem. Rev.* **2017**, *117* (10), 6633–6635. https://doi.org/10.1021/acs.chemrev.7b00246.

(23) Banerjee, A.; Ibsen, K.; Brown, T.; Chen, R.; Agatemor, C.; Mitragotri, S. Ionic Liquids for Oral Insulin Delivery. *Proc. Natl. Acad. Sci.* **2018**, *115* (28), 7296–7301. https://doi.org/10.1073/pnas.1722338115.

(24) Qi, Q. M.; Mitragotri, S. Mechanistic Study of Transdermal Delivery of Macromolecules Assisted by Ionic Liquids. *J. Control. release Off. J. Control. Release Soc.* **2019**, *311–312*, 162–169. https://doi.org/10.1016/j.jconrel.2019.08.029.

(25) Angsantikul, P.; Peng, K.; Curreri, A. M.; Chua, Y.; Chen, K. Z.; Ehondor, J.; Mitragotri, S. Ionic Liquids and Deep Eutectic Solvents for Enhanced Delivery of Antibodies in the Gastrointestinal Tract. *Adv. Funct. Mater.* **2021**, *31* (44), 2002912. https://doi.org/https://doi.org/10.1002/adfm.202002912.

(26) Libao-Mercado, A. J.; de Lange, C. F. M. Refined Methodology to Purify Mucins from Pig Colonic Mucosa. *Livest. Sci.* **2007**, *109* (1–3), 141–144. https://doi.org/10.1016/j.livsci.2007.01.125.

(27) Perez-Vilar, J.; Eckhardt, A. E.; DeLuca, A.; Hill, R. L. Porcine Submaxillary Mucin Forms Disulfide-Linked Multimers through Its Amino-Terminal D-Domains. *J. Biol. Chem.* **1998**, *273* (23), 14442–14449. https://doi.org/10.1074/jbc.273.23.14442.

(28) De Lisle, R. C.; Borowitz, D. The Cystic Fibrosis Intestine. *Cold Spring Harb. Perspect. Med.* **2013**, *3* (9), 1–18. https://doi.org/10.1101/cshperspect.a009753.

(29) Su, C.; Padra, M.; Constantino, M. A.; Sharba, S.; Thorell, A.; Lindén, S. K.; Bansil, R. Influence of the Viscosity of Healthy and Diseased Human Mucins on the Motility of Helicobacter Pylori. *Sci. Rep.* **2018**, *8* (1), 1–13. https://doi.org/10.1038/s41598-018-27732-3.

(30) Meldrum, O. W.; Yakubov, G. E.; Bonilla, M. R.; Deshmukh, O.; McGuckin, M. A.; Gidley, M. J. Mucin Gel Assembly Is Controlled by a Collective Action of Non-Mucin Proteins, Disulfide Bridges, Ca2+ -Mediated Links, and Hydrogen Bonding. *Sci. Rep.* **2018**, *8* (1), 1–16. https://doi.org/10.1038/s41598-018-24223-3.

(31) Kakati, N.; Parashar, C. K.; Thakur, S.; Deshmukh, O. S.; Bandyopadhyay, D. Microrheology of Mucin–Albumin Assembly Using Diffusing Wave Spectroscopy. *ACS Appl. Bio Mater.* **2022**, *5* (9), 4118–4127. https://doi.org/10.1021/acsabm.2c00098.

(32) Paul, N.; Harish, G.; Banerjee, T. Decontamination of Enoxacin Containing Aqueous Phase through Hydrophobic Deep Eutectic Solvents: Solvent Regeneration and Quantum Chemical Insights. *J. Mol. Liq.* **2023**, *374*, 121254. https://doi.org/https://doi.org/10.1016/j.molliq.2023.121254.

(33) Paul, N.; Harish, G.; Banerjee, T. Stability Mechanism of Menthol and Fatty Acid Based Hydrophobic Eutectic Solvents: Insights from Nonbonded Interactions. *ACS Sustain. Chem. Eng.* **2023**, *11* (8), 3539–3556. https://doi.org/10.1021/acssuschemeng.2c06137.

(34) Paul, N.; Banerjee, T. Study on the Extraction of Acetamiprid and Imidacloprid from

an Aqueous Environment Using Menthol-Based Hydrophobic Eutectic Solvents: Quantum Chemical and Molecular Dynamics Insights. *ACS Sustain. Chem. Eng.* **2022**, *10* (13), 4227–4246. https://doi.org/10.1021/acssuschemeng.2c00023.

(35) Paul, N.; Naik, P. K.; Ribeiro, B. D.; Gooh Pattader, P. S.; Marrucho, I. M.; Banerjee, T. Molecular Dynamics Insights and Water Stability of Hydrophobic Deep Eutectic Solvents Aided Extraction of Nitenpyram from an Aqueous Environment. *J. Phys. Chem. B* **2020**, *124* (34), 7405–7420. https://doi.org/10.1021/acs.jpcb.0c03647.

(36) Du, X.; Dubin, P. L.; Hoagland, D. A.; Sun, L. Protein-Selective Coacervation with Hyaluronic Acid. *Biomacromolecules* **2014**, *15* (3), 726–734. https://doi.org/10.1021/bm500041a.

(37) Kakati, N.; Ahari, D.; Parmar, P. R.; Deshmukh, O. S.; Bandyopadhyay, D. Lactic Acid-Induced Colloidal Microrheology of Synovial Fluids. *ACS Biomater. Sci. Eng.* **2024**. https://doi.org/10.1021/acsbiomaterials.3c01846.

(38) Waigh, T. A. Advances in the Microrheology of Complex Fluids. *Rep. Prog. Phys.* **2016**, *79* (7), 74601. https://doi.org/10.1088/0034-4885/79/7/074601.

(39) Weitz, D.; Brown, D. P.-W.; Ed, undefined; 1993, undefined. Dynamic Light Scattering.

(40) Mason, T. G.; Weitz, D. A. Optical Measurements of Frequency-Dependent Linear Viscoelastic Moduli of Complex Fluids. *Phys. Rev. Lett.* **1995**, *74* (7), 1250–1253. https://doi.org/10.1103/PhysRevLett.74.1250.

(41) Mason, T. G.; Gang, H.; Weitz, D. A. Diffusing-Wave-Spectroscopy Measurements of Viscoelasticity of Complex Fluids. *J. Opt. Soc. Am. A* **1997**, *14* (1), 139. https://doi.org/10.1364/josaa.14.000139.

(42) Lee, C.; Yang, W.; Parr, R. G. Development of the Colle-Salvetti Correlation-Energy Formula into a Functional of the Electron Density. *Phys. Rev. B* **1988**, *37* (2), 785–789. https://doi.org/10.1103/PhysRevB.37.785.

(43) Becke, A. D. Density-Functional Exchange-Energy Approximation with Correct Asymptotic Behavior. *Phys. Rev. A* **1988**, *38* (6), 3098–3100. https://doi.org/10.1103/PhysRevA.38.3098.

(44) Becke, A. D. Density-functional Thermochemistry. III. The Role of Exact Exchange. *J. Chem. Phys.* **1993**, *98* (7), 5648–5652. https://doi.org/10.1063/1.464913.

(45) Grimme, S.; Antony, J.; Ehrlich, S.; Krieg, H. A Consistent and Accurate Ab Initio Parametrization of Density Functional Dispersion Correction (DFT-D) for the 94 Elements H-Pu. *J. Chem. Phys.* **2010**, *132* (15), 154104. https://doi.org/10.1063/1.3382344.

(46) Grimme, S.; Ehrlich, S.; Goerigk, L. Effect of the Damping Function in Dispersion Corrected Density Functional Theory. *J. Comput. Chem.* **2011**, *32* (7), 1456–1465. https://doi.org/10.1002/jcc.21759.

(47) Boys, S. F.; Bernardi, F. . The Calculation of Small Molecular Interactions by the Differences of Separate Total Energies. Some Procedures with Reduced Errors. *Mol. Phys.* **2002**, *19*, 553–566. https://doi.org/10.1080/00268977000101561.

(48) Glendening, E. D.; Landis, C. R.; Weinhold, F. NBO 6.0: Natural Bond Orbital Analysis Program. *J. Comput. Chem.* **2013**, *34* (16), 1429–1437.

https://doi.org/10.1002/jcc.23266.

(49) Fukui, K. The Theory of Orientation and Stereoselection. In *Fortschr. Chem. Forsch.*; 2006; Vol. 15, pp 1–85. https://doi.org/10.1007/BFb0051113.

(50) Bader, R. F. W.; Bader, R. F. *Atoms in Molecules: A Quantum Theory*; International series of monographs on chemistry; Clarendon Press, 1990.

(51) Johnson, E. R.; Keinan, S.; Mori-Sánchez, P.; Contreras-García, J.; Cohen, A. J.; Yang, W. Revealing Noncovalent Interactions. *J. Am. Chem. Soc.* **2010**, *132* (18), 6498–6506. https://doi.org/10.1021/ja100936w.

(52) Marekha, B.; Kalugin, O.; Abdenacer, I. Non-Covalent Interactions in Ionic Liquid Ion Pairs and Ion Pair Dimers: A Quantum Chemical Calculation Analysis. *Phys. Chem. Chem. Phys.* **2015**, *17*. https://doi.org/10.1039/c5cp02197a.

(53) Lu, T.; Chen, F. Multiwfn: A Multifunctional Wavefunction Analyzer. *J. Comput. Chem.* **2012**, *33*, 580–592. https://doi.org/10.1002/jcc.22885.

(54) Jia, Z.; Guo, Z.; Yang, C.-T.; Prestidge, C.; Thierry, B. “Mucus-on-Chip”: A New Tool to Study the Dynamic Penetration of Nanoparticulate Drug Carriers into Mucus. *Int. J. Pharm.* **2021**, *598*, 120391. https://doi.org/https://doi.org/10.1016/j.ijpharm.2021.120391.

(55) Deacon, M. P.; McGurk, S.; Roberts, C. J.; Williams, P. M.; Tendler, S. J.; Davies, M. C.; Davis, S. S.; Harding, S. E. Atomic Force Microscopy of Gastric Mucin and Chitosan Mucoadhesive Systems. *Biochem. J.* **2000**, *348 Pt 3* (Pt 3), 557–563.

(56) Hizaddin, H. F.; Hashim, M. A.; Anantharaj, R. Evaluation of Molecular Interaction in Binary Mixture of Ionic Liquids + Heterocyclic Nitrogen Compounds: Ab Initio Method and COSMO-RS Model. *Ind. Eng. Chem. Res.* **2013**, *52* (50), 18043–18058. https://doi.org/10.1021/ie403032t.

(57) Simon, S.; Duran, M.; Dannenberg, J. J. How Does Basis Set Superposition Error Change the Potential Surfaces for Hydrogen-bonded Dimers? *J. Chem. Phys.* **1996**, *105* (24), 11024–11031. https://doi.org/10.1063/1.472902.

(58) Contreras-García, J.; Johnson, E. R.; Keinan, S.; Chaudret, R.; Piquemal, J.-P.; Beratan, D. N.; Yang, W. NCIPLOT: A Program for Plotting Noncovalent Interaction Regions. *J. Chem. Theory Comput.* **2011**, *7* (3), 625–632. https://doi.org/10.1021/ct100641a.

(59) Contreras-García, J.; Calatayud, M.; Piquemal, J.-P.; Recio, J. M. Ionic Interactions: Comparative Topological Approach. *Comput. Theor. Chem.* **2012**, *998*, 193–201. https://doi.org/https://doi.org/10.1016/j.comptc.2012.07.043.

CHAPTER 4

Lactic Acid-Induced Colloidal Microrheology of Synovial Fluids

Contents

ABSTRACT

Presence of colloidal scaffolds composed of proteins and hyaluronic acid engender unique viscous and elastic properties to the synovial fluid (SF). While the elastic resistance of SF due to the presence of such nanoscale structures provides the load-bearing capacity, the viscous nature enables fluidity of the joints during the movements to minimize the wear and tear of the adjacent muscle or cartilage or bone tissues. It is well known that the hypoxic conditions at the bone-joints often increase the lactic acid (LA) concentration due to the occurrence of excess anaerobic respiration during either hyperactivity or arthritic conditions. The present chapter uncovers that, in such a scenario beyond a critical loading of LA, the colloidal nano-scaffolds of SF break down to precipitate higher molecular weight (MW) proteins and hyaluronic acid (HA). Subsequently, the viscosity and elasticity of SF reduce drastically to manifest a fluid that has reduced load bearing and wear and tear resistance capacity. Interestingly, the study also suggests that a heathy SF is a viscoelastic fluid with a mild Hookean elasticity and Non-Newtonian fluidity, which eventually transforms into a viscous watery liquid in presence of a higher loading of LA. We employ this knowledge to biosynthesize an artificial SF that emulates the characteristics of the real one. Remarkably, the spatiotemporal microscopic images uncover that even for the artificial SF, a dynamic crosslinking of the high MW proteins and HA takes place before precipitating out of the same from the artificial SF matrix, emulating the real one. Control experiments suggest that this phenomenon is absent in the case when LA is mixed with either pure HA or proteins. The experiments unfold the specific role of LA in the destruction of colloidal nano-scaffolds of synovia, which is an extremely important requirement for the biosynthesis and translation of artificial synovial fluid.

4.1. Introduction

Natural processes utilize diverse rheological properties of complex fluids e.g. viscosity, elasticity, and relaxation time to their advantage, which can be one of the very interesting areas of biomimetic research targeting a wide range of modern-day applications.[1–3] For example, the physiologic synovial fluids (SF) are a class of biomaterials with a very unique rheology, which is omnipresent at the joints of bones/cartilages in the entire animal kingdom. The SF can also be termed as a smart biofluid because its tailormade microrheology helps in maximizing the load-bearing capacity of the bones at the joints alongside minimizing the wear and tear due to the significant reduction of the contact friction between the moving joints[4]. Importantly, the natural SF tends to dry up or denature due to the pathophysiological conditions of the arthritic patients or age-related issues.[5] In such a scenario, the biomimetic artificial prototypes of the SF with similar viscous, elastic, and relaxation properties have been employed as therapeutic agents to mitigate friction, wear, and lubrication at the interface of the joints, especially in the advanced stages of arthritis.[6,7]

Certainly, it is of fundamental importance that the microrheological properties of such complex biological fluids need to be known before translating the artificial therapeutic alternatives of the same.[4,8] Further, the biosynthesis of such materials can have significant potential to translate into an array of contemporary tribological applications. In this direction, the prior-art suggests that the key components of SF have been 70 – 80% water mixed with various biomaterials such as hyaluronic acid (HA), lubricin, proteinase, collagenases, albumin, γ-globulin, and prostaglandin, which are responsible for manifesting the unique rheology to this material.[9,10] The viscoelasticity of the mixture allows non-Newtonian liquid like fluidity (e.g. a shear thinning behavior) during the movement of joints under minimal stress while providing high viscous resistance under severe stress (e.g. a shear thickening behavior) to minimize friction between the joints. For example, among the other components, while albumin and γ-globulin have a role in imparting interfacial viscosity to SF,[11] lubricin is a glycoprotein that imparts the boundary lubrication properties to SF. Lubricin also helps in creating a weakly connected network of HA chains that manifests the shear thinning behavior of SF.[4]

Importantly, HA is one major building block of SF that is essentially a linear polysaccharide consisting of repetitive units of N-acetylglucosamine and glucuronic acid linked via β-(1-4) and β-(1-3) glycosidic bonds.[12–14] The rheological property of SF is heavily dependent on the concentration and molecular weight of HA.[15] The molecular weight and concentrations of HA change drastically resulting in decreased viscoelasticity under various diseased conditions, e.g., during the freezing of joints or arthritis[15,16]. The prior-art suggests that a low concentration of HA has more impact on the viscoelastic behavior of SF[17] while a low molecular weight of HA has less binding affinity to cartilage surfaces, facilitating their degradation to cause osteoarthritis.[18]

It is also important to note here that, when the physical workload of a healthy human increases beyond a critical limit, the mobility of various joints like the knee, shoulder, neck, ankle, or groin ‘freeze’ owing to the accumulation of lactic acid (LA) due to the increase in the anaerobic respiration in the synovium. On the other hand, pathologically there are different types of arthritic conditions such as osteoarthritis, rheumatoid arthritis, and gouty arthritis.[19] Osteoarthritis is majorly found in elderly people when cartilage tissue around the joints itself degrades with age.[20,21] In the case of rheumatoid arthritis the immune system of a human self-depreciates the synovium.[22] Regardless of the type of arthritic condition, each of these conditions leads to abnormal levels of LA in the synovial fluids.[23] **Figure 4.1a** schematically shows a typical flow chart of LA production inside the synovium in an arthritic state. Specially in the case of rheumatoid arthritis, synovial lactate levels are found to be elevated[23] due to anaerobic respiration of glucose where pyruvate is converted to lactate by lactate dehydrogenase enzyme (LDH). The reason behind this metabolic change is due to the hypoxic environment where the expression of a transcription factor – namely the hypoxia inducible factor (HIF-1α) regulates the expression of glucose transporter GLUT 1 and 3 for an increased glucose uptake. The concentration of HIF-1α also regulates the expression of lactate dehydrogenase enzyme, which produces lactate from pyruvate as an end product of anaerobic glycolysis process.[24]

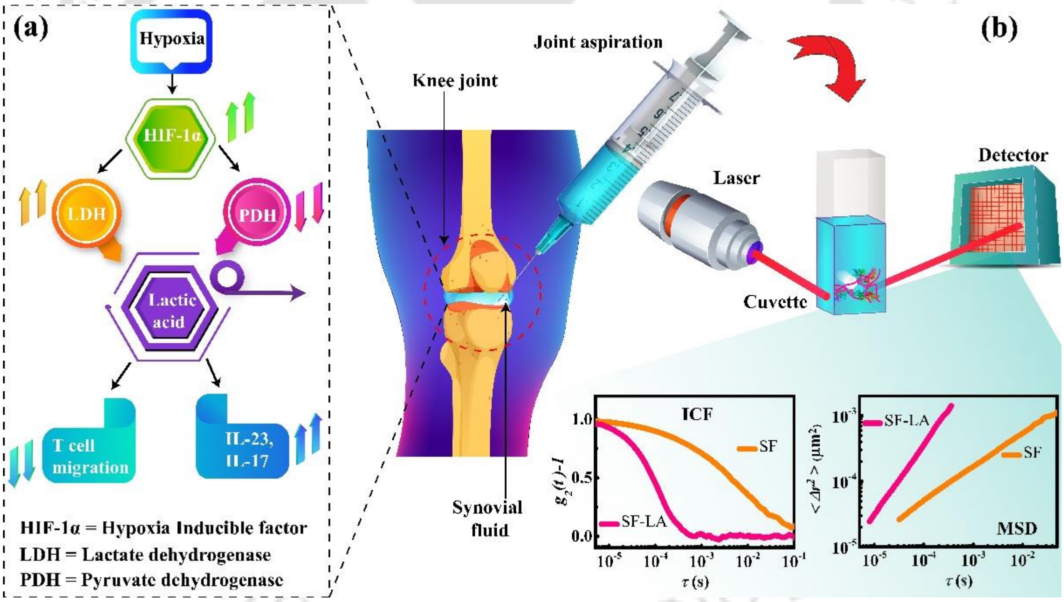

Figure 4.1. (a) Flow chart of lactic acid (LA) production inside the synovium in an arthritic state. (b) Schematic illustration of DWS instrument, which displays the intensity autocorrelation function (ICF) and mean squared displacement (MSD) data.

Previous studies indicate that the origin of this hypoxic environment manifest due to the increased cell proliferation or increased intra-articular pressure from either synovial fluid effusion or hyperplasia.[25] In a way, the increased glucose uptake for glycolysis results in the elevated lactate levels, which subsequently dysfunctions the fibroblast-like synoviocyte

(FLS).[26,27] At this juncture, it may also be noted here that LA concentration in the various body fluids plays an important role as an immune modulatory signal to produce cytokines. For example, increase in LA concentration enhances the IL-23 and IL-17 pathways and acts as a pro-inflammatory signal.[28,29] LA also suppresses the T-cell effector function and stops the migration of T-cells, which eventually results in a chronic inflammatory condition.[29–31] Again, in such a scenario, the dominance of anaerobic respiration leads to the accumulation of LA in the joints filled with synovial fluid to cause the immobilization or freezing of the joints.[31]

In particular, an elevated LA concentration not only reduces the pH of a synovial fluid but also has significant influence on the rheology of the SF. Even for a healthy human, the accumulation of LA in SF during the anaerobic respiration and subsequent regeneration of fluidity of SF during the aerobic respiration through the removal of LA has been found to be a routine activity.[32,33] However, for the patients with various types or stages of arthritis, the regeneration of SF progressively becomes difficult and require the usage of artificial SF to recover the mobility.[34–36] Surprisingly, the loss of fluidity and the subsequent regeneration of the same of SF in presence or absence of LA is one such mystery that has not been explored so far in detail especially from the microrheological point of view. The fundamentals related to the variations in the microrheology of SF with the variation in the pH and LA loading is expected to provide much deeper insight into the pathology of diverse joint related diseases including the various form of arthritis.

In this Chapter, we perform a detailed microrheological investigations on the effects of the LA on the porcine SF. In order to determine the microrheology we have used diffusing wave spectroscopy (DWS) which provides the intensity autocorrelation function (ICF) and mean squared displacement (MSD) of the probed particles. **Figure 4.1b** shows the schematic diagram of DWS. The study has been performed directly under the microscope to uncover a unique cross-linking phenomena of high MW proteins and HA in the SF in presence of LA. The study also uncovers the nature of the interaction between HA, LA, and albumin in SF with the help of a detailed ζ-potential, Circular Dichroism (CD), and fluorescence spectra analyses. All these characterization helps to connect the cross-linking of the SF phenomenon to the folding of albumin with increasing LA concentration in an SF, which can be a simple but major finding in the future studies related to the microrheology of SF. The aforesaid phenomenon elucidates the interaction between albumin and HA in LA environments to simulate the real-life arthritic conditions. Subsequently, this information helps us in the biosynthesis of a novel biomimetic therapeutic SF, which has properties similar to the real SF and can be suitable for the arthritic treatments. The proposed artificial SF formulation consists HA mixed with bovine Serum albumin (BSA) and γ-globulin, to engender microrheological properties such as viscosity, elasticity, and relaxation time resembling the natural SF. Overall, the results reported here will not only enable a much deeper insight in understanding the reasons behind the special properties of synovial fluid but also help in the synthesis of artificial SFs for future commercial use.

4.2. Experimental Section

4.2.1. Materials

Hyaluronic acid sodium salt, γ-globulin, and L-lactic acid were purchased from Sigma-Aldrich Pvt. Ltd. BSA (98% pure) were purchased from Sisco Research Laboratories Pvt. Ltd (SRL). The polystyrene tracer particle diameter of 510 nm (10%) was purchased from LS Instruments AG, Switzerland. All the chemicals were used without further purification. Milli-Q water was used in all experiments for preparing solutions.

4.2.2. Preparation of HA and Model Synovial Fluid Solution

Hyaluronic acid solution was prepared by mixing hyaluronic acid in 10 mM phosphate buffer at pH 7.4. For the preparation of model synovial fluid, a previously reported method was followed, where 10 mg/mL BSA and 0.5 mg/mL were allowed to mix with 3.4 mg/mL HA solution in a rocker overnight. [11,37] Prior to microrheology measurement, 80 µL of polystyrene tracer particles were added in 920 µL of the prepared sample. The tracer particle concentration was 0.8% in all microrheological experiments and did not affect the overall experimental results. All the measurements were performed thrice for the precision and reproducibility of the data.

4.2.3. Microscopic observation of model SF in the presence of LA

For microscopic observations, prior to the preparation of model SF, BSA is labelled with FITC dye as described in the previous literature and observed under 2.5X objective with an excitation wavelength at 495 nm.[38] To track the diffusion of BSA under a fluorescent microscope, Fluorescein isothiocyanate (FITC) dye was utilized. The reaction took place between the isothiocyanate group (-N=C=S-) and the amine group of protein and resulted in a thiourea bond. For the synthesis of fluorescence-labeled BSA, initially, 2 g/L of BSA was dissolved in MilliQ water. Subsequently, FITC was dissolved in anhydrous DMSO at a concentration of 1g/L. After that, the BSA solution was coupled with FITC solution with a ratio of 20:1 v/v and kept in the dark for the coupling reaction for 8 hours. To eliminate the unbound dye from the reaction mixture dialysis was carried out for 48 hours in the dark at 4°C. Furthermore, the solution was freeze-dried and stored at -20°C. For the fluorescence microscopic observation, excitation and emission wavelengths were taken at 495 nm and 515 nm respectively.

4.2.4. Pig Synovial Fluid Sample

The porcine SF from a healthy joint of a white pig devoid of blood contamination was obtained from ICAR- National Research Centre on Pig situated in Guwahati, India before storing them at – 20°C. The pig SF was then diluted 10 times with 10 mM phosphate buffer saline (PBS) at pH 7.4. Subsequently, in order to separate cells, centrifuged for 20 min at 8000 rpm and pellets were discarded. In 1 mL of 10X diluted pig SF, 25 µL of LA was added and kept overnight. The LA solution was prepared in 10 mM phosphate buffer at pH 7.4.

For agarose gel electrophoresis, 0.5% agarose gel was prepared in TAE buffer. Prior to agarose gel electrophoresis, pig SF was digested with proteinase K followed by centrifugation to separate the proteins from the HA. A stock solution of 3 mg/mL proteinase K was prepared in 10 mM phosphate buffer saline. Initially, pig SF was diluted 10 times subsequently, 70 µL of proteinase K solution was added and stored at 37°C overnight. After that, centrifugation was done to separate the digested proteins. Before gel loading, 10 µL of the pig SF was mixed with 1 µL gel loading dye and mixed properly. Subsequently, 10 µL is loaded into the well and allowed to run at 55 V for 8 h. For gel staining, 0.005% stains all dye was used and kept for 14 h in a rocker in a dark environment. Stains all dye was prepared in 50% methanol. For de-staining the gel, 10% methanol was for overnight de-staining.

4.2.5. DWS microrheology

The diffusing wave spectroscopy (DWS) was used for all microrheological measurements, which is based on the light scattering technique to determine the microrheology of turbid samples.[39,40] In order to make the samples turbid, 80 µL 10% polystyrene tracer particles with a diameter of 510 nm were used. Prior to the measurement samples were taken in a 2 mm cuvette and incubated for 10 min at 37°C in the sample holder of the instrument. The microrheology measurements were performed by DWS RheoLab instrument, LS instruments AG, Switzerland. **Figure 4.1b** shows the instrument diagram of DWS where a laser light of 685 nm wavelength incident on a cuvette containing the sample. Due to the Brownian motion of tracer particles scattered, the light intensity fluctuates over time and a correlator measures the, ICF $\left[g_2(\tau)-1\right]$ to evaluate the ensemble-averaged mean squared displacements (MSD) of the tracer particles, denoted as $\left\langle \Delta r^2(\tau)\right\rangle$.[41] The relationship between the MSD and the lag time (τ) for a particle performing Brownian motion in a viscoelastic liquid is given as,

$$\left\langle \Delta r^2(\tau)\right\rangle = 2nD_t\tau^{\alpha}. \qquad (1)$$

Where D_t is the time-dependent diffusivity of the tracer particle and $0 < \alpha < 1$, n refers to the dimensionality (n =3 for a 3-dimensional analysis). For a tracer particle diffusing in a purely viscous environment, the exponent α = 1 and the diffusion coefficient D of the probe is inversely proportional to the viscosity (η) of the surrounding liquid. The viscoelastic modulus can be calculated from the MSD using the generalized Stokes-Einstein relation,[42,43]

$$G(s) = \frac{k_B T}{\pi a s\left\langle \Delta r^2(s)\right\rangle}, \qquad (2)$$

where $G(s)$ is the Laplace transform of the viscoelastic relaxation modulus $G(t)$, $\left\langle \Delta r^2(s)\right\rangle$ is the Laplace transform of the MSD, k_B is the Boltzmann constant, T is absolute temperature, and a is the radius of the tracer particle. Replacing s with iω, we can get the complex modulus and complex viscosity $\left(\eta^*(\omega) = G^*(\omega)/\omega\right)$.

4.2.6. Bulk Rheology

For bulk rheology experiments, Anton Paar MCR 301 Rheometer was used. The measurements were carried out using a 50 mm diameter 1-degree cone and plate geometry at 37°C. All the measurements are taken in triplicates and the mean data is plotted along with the standard deviations.

4.2.7. ζ-potential measurements

For ζ-potential measurements of BSA and HA in varied lactic acid concentrations, Litesizer 500 instrument from Anton Paar was used. Prior to measurements, samples were diluted 100 times. All the measurements were performed in triplicates and mean data was used for the analysis.

4.2.8. Circular Dichroism Analysis (CD)

In order to determine the effects of LA on the secondary structure of BSA, CD analysis was done using UV-CD (JASCO, J-1500) instrument. For the CD measurement, a 2 mm pathlength quartz cuvette was used containing the samples. All the measurements were done in the scanning range of 190-260 nm with an average of 5 accumulations. The scanning speed was maintained at 100 nm/min, 0.1 nm of bandwidth. In all the experiments, Baseline correction was done by using a buffer with respective lactic acid concentrations.

4.2.9. Morphology analysis by AFM

The morphological analysis of pig SF in the presence of lactic acid was analyzed by using AFM (Cypher Asylum, Oxford). For this we diluted the samples 100 times and drop cast on a freshly cut silicon wafer of size 5 mm × 8 mm. Subsequently spin-coated for 2000 rpm for 3 min. The spin-coated samples were dried under a vacuum desiccator overnight. The scan rate was kept at 0.5 to 1 Hz and the set point was around 500 mV. Comparative analysis was performed for scan areas of 2 µm^2 and 5 µm^2 for both lactic acids treated and untreated synovial fluid samples.

4.2.10. SDS-PAGE Analysis

The reducing SDS-PAGE was used as per the protocol described in Sambrook and Russel, Molecular Cloning-A laboratory manual to examine the purity of purified protein.[44] Resolving gel (10% acrylamide) was utilized for running all the purified protein samples. Protein samples were prepared for loading by mixing with the gel loading buffer in a 4:1 ratio and then allowed to boil at 95 °C for 5min. Subsequently, samples were separated on vertical Mini-PROTEAN^R Tetra Electrophoresis System (Make: Bio-Rad) at 80 V for 2.15 h. For visualization of the separated sample, gels were removed from the electrophoresis apparatus and stained with colloidal Coomassie stain for 4 h and then the gels were placed in destaining solution overnight to allow the de-staining of gel. Standard molecular markers were used to determine the approximate molecular weight of protein in the gel.

4.3. Results and Discussions

4.3.1. Effect of LA on Pig SF

In order to investigate the effects of LA on the microrheology, the real porcine SF has been treated with LA, following all the standard experimental and regulatory protocols as mentioned in the previous section. **Figure 4.2a** shows the turbid precipitation inside the pig-SF immediately after the addition of LA. Subsequently, the supernatant has been taken for analyses by SDS-PAGE and agarose gel-electrophoresis. **Figure 4.2b** suggests that the proteins with high MW bands are absent in the supernatant of the LA treated pig-SF sample, which indicates that the high MW proteins including albumin and lubricin have precipitated. Later, agarose gel electrophoresis studies reveal the complete absence of HA bands for the supernatant of the LA treated both proteinase K digested (dSF) and undigested pig-SF sample, which directs the presence of HA in the precipitate, as shown in **Figure 4.2c**. On the other hand, there is no change in bands for untreated and treated HA. The experiments point to the fact that in the presence of LA, the high MW proteins co-precipitate with HA to engender a loss of viscous and elastic properties of SF.

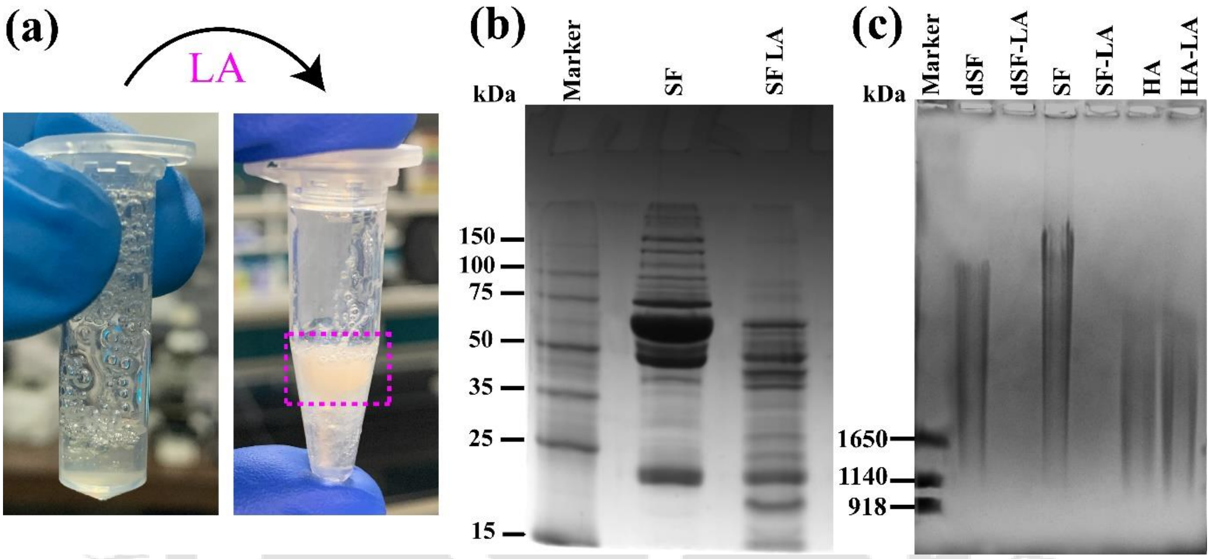

Figure 4.2. (a) Visual observation of precipitates (pink box) in pig SF after the addition of LA. (b) SDS-PAGE of the supernatant after phase separation of pig SF by the LA. (c) Agarose gel electrophoresis of the supernatant after phase separation of pig SF by the LA.

We further, performed microrheology analysis of the supernatant with the help of the DWS instrument. We diluted the SF twice before adding LA due to the shortage of the pig SF. **Figure 4.3a** shows ICF vs. τ plot that indicates a much faster decay of the LA treated pig-SF. Further, **Figure 4.3b** shows the MSD vs. τ plot, which also indicates a significant reduction in the viscosity and elasticity of the supernatant fluid in presence of LA. The plots suggest that the power law exponent changes significantly from 0.35 to 0.53 under different dilutions of pig-SF. More importantly, in case of LA treated pig-SF sample, the power law exponent became close to 1, which is similar to a buffer solution. The decrease in the elastic modulus (G') of the LA-treated SF in comparison to the untreated one is depicted in **Figure 4.3c**. Similarly, **Figure 4.3d** illustrates how the bulk viscosity of SF changes following LA treatment.

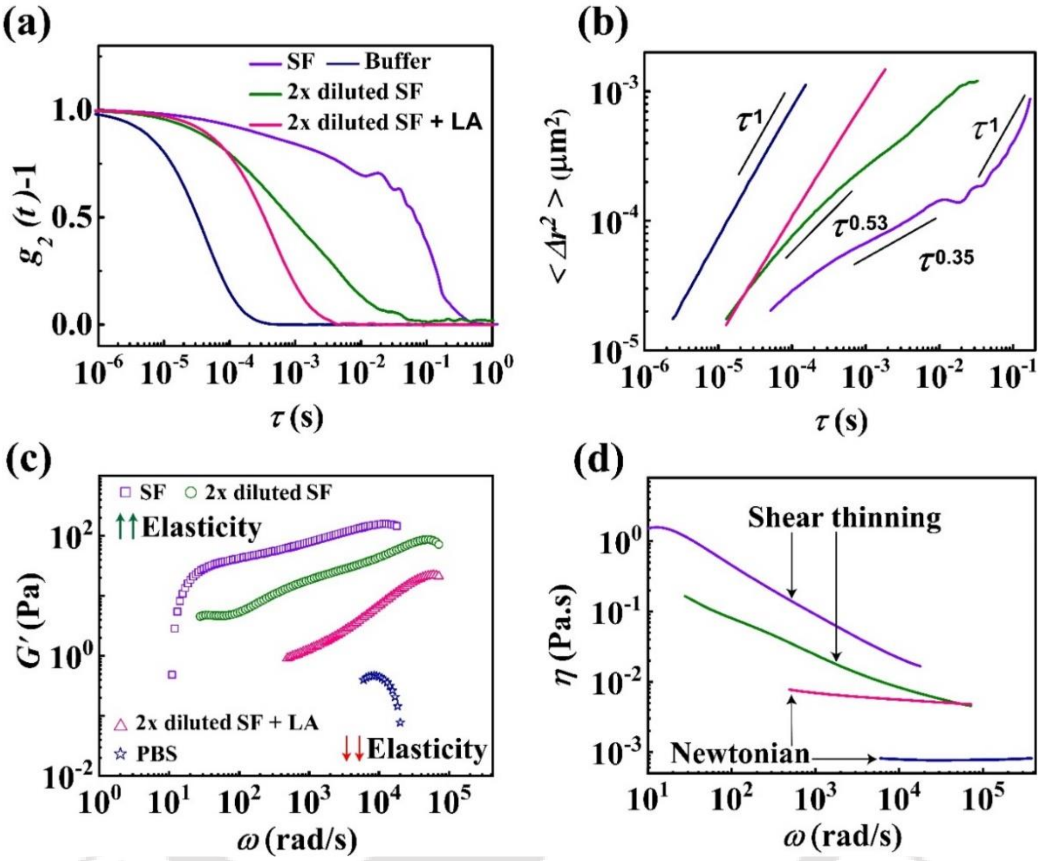

Figure 4.3. Microrheology and bulk rheology of LA-treated pig SF: (a) ICF vs. lag time and (b) MSD vs. lag time; (c) the storage modulus G ′ vs. frequency as determined by DWS data (d) The rheometer's data on bulk viscosity against frequency.

Consequently, data supports the idea that the presence of LA causes a reduction of both elastic and viscous resistance. Clearly, the plots suggest that a healthy SF is a viscoelastic fluid with a weak Hookean Elasticity and a non-Newtonian shear thinning fluidity. However, beyond a critical loading of LA, the SF behave more like a Newtonian watery liquid with a minimal elastic resistance. The experiments reported above provides a key insight into the microrheology of SF under aerobic and anaerobic conditions with the variations in the LA. In what follows, it is shown that, with the increase in the loading of LA in SF, precipitation of HA and high MW proteins take place. This eventually reduce the viscous (a kinetic factor) and elastic (a thermodynamic factor) resistances of the SF to eventually reduce load bearing capacity and increase the possibility of friction, wear and tear inside the moving bone-cartilage-muscle joints causing either freezing of joints or deterioration of the arthritic conditions.

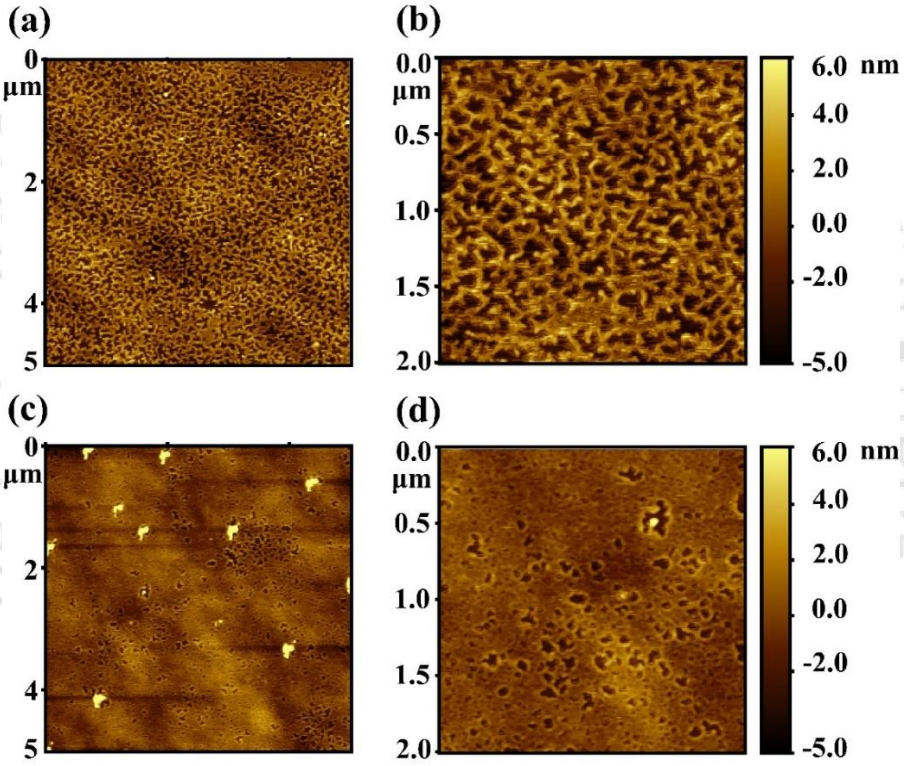

Figure 4.4. AFM images of pig-SF with and without LA. (a) 5×5 μm^2 and (b) 2×2 μm^2 showing the morphology of normal Pig SF; (c) 5×5 μm^2 and (d) 2×2 μm^2 showing the LA treated-SF after the addition of lactic acid.

The results reported in **Figure 4.3** get further support when we study the same aspect under atomic force microscopy (AFM) in **Figure 4.4**. **Figures 4.4a** (real pig-SF sample) and 4b (pig-SF treated with LA) show the morphologies in 5×5 μm^2 and 2×2 μm^2 areas through an AFM analysis. The micrographs suggest the presence of a periodic bi-continuous scaffold like nanostructures of 2 to 4 nm height in the untreated pig-SF, which can be manifested from a weak colloidal assembly of HA and other proteins. Intuitively, presence of such colloidal scaffolds is expected to provide a unique viscoelastic nature to SF, as discussed in the previous section. While the scaffolds will provide the required load-bearing capacity the fluid surrounding the same to enable fluidity during the joint movements with a minimal wear and tear. Further, **Figures 4.4c-d** show the morphology of LA treated pig-SF in 5×5 μm^2 and 2×2 μm^2 areas where an aggregated random morphology has been observed. The figures suggest a clear loss of its unique colloidal assemblage and subsequently its special micorheological characteristics, as reported in the previous section.

4.3.2. Effects of Lactic Acid on Model SF

Prior-art suggest that the real SF contains HA, variety of proteins that include but are not limited to albumin, gamma globulins, and glycoproteins like lubricin.[4] All these components play an important role in the viscoelastic behavior of real SF and thereby in its efficacy as a lubricant at the joints. In such a scenario, it is important that we study the effects of LA on the solutions of proteins-HA mixtures – commonly termed as model SF.[11] For this purpose, we initially prepare a model SF, which consists of hyaluronic acid, bovine serum albumin - BSA, and γ-globulin - GG wherein the concentrations of these components are emulated from the physiological conditions of SF, as previously reported.[11] The following **Table 4.1** shows the typical compositions used for this experiment:

Table 4.1. Components of prepared model synovial fluid

Components	**Quantity (mg/mL)**
Hyaluronic acid	3.4
Bovine serum albumin	10
γ-globulin	0.5

Remarkably enough, when LA is added to this model SF, we observe very similar phase separation, as observed for the pig-SF in the previous section. Thus, we investigate the matter further under an optical microscope with some control experiments to understand the phenomenon with more depth. **Figure 4.5** and video 1 in Appendix 1 show the spatiotemporal evolution of a droplet of BSA, HA, and model SF when treated with LA. The micrographs in rows (a) and (b) suggest that BSA and HA individually do not precipitate under the influence of LA. Interestingly, row (c) shows the progressive precipitation of the BSA and HA when treated with LA, which has also been imaged under fluorescence to understand the phenomenon better.

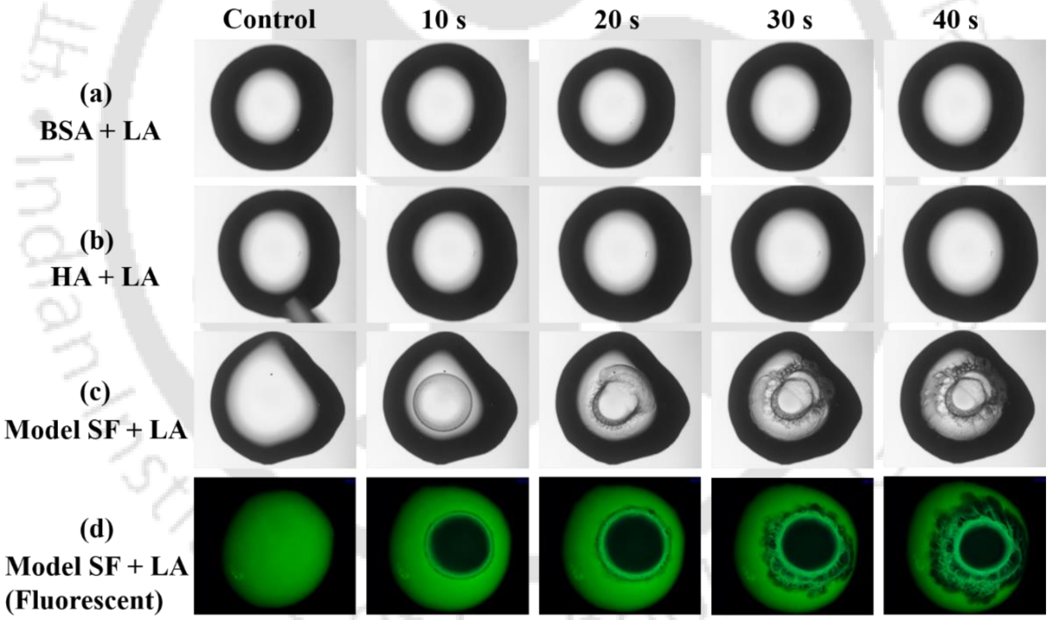

Figure 4.5. Microscopic images of BSA, HA, and model SF droplet after LA treatment with varied time scales.

The darkfield images suggest that the presence of LA phase separates the aggregates of HA-BSA complexes because in this experiment the BSA has been labelled with FITC dye, as described previously.[38] The video and the micrographs also indicate the phase separated

BSA forms aggregates with HA to leave a supernatant with much lesser viscosity and elasticity (dark field), as observed in for the pig-SF experiments.

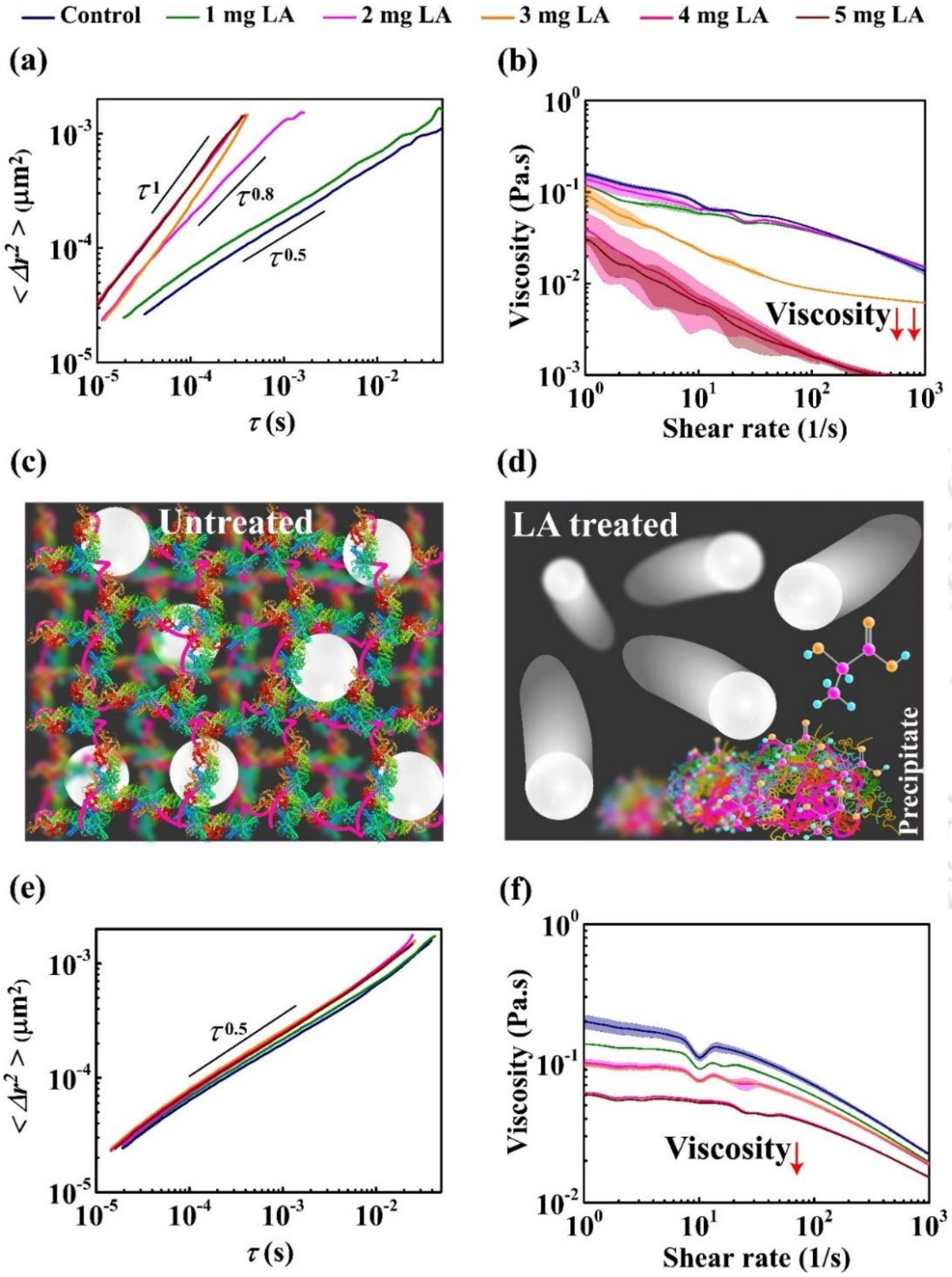

Figure 4.6. Micro and bulk rheological characterization of model SF and HA in presence of increasing LA concentration. (a) MSD vs. τ plot for model SF in presence of increasing LA. (b) Bulk rheology of model SF in the presence of LA, where viscosity reduces with increasing LA concentrations. (c) and (d) Graphical representation of SF vs. lactic acid treated SF respectively. (e) MSD ($<\Delta r^2>$) vs. τ plot indicates the increased MSD in the case of lactic acid treated HA. (f) Bulk rheology of HA with increasing LA concentrations.

Following this, the supernatant of the model SF samples is further analyzed with DWS and rheometer for micro and bulk rheology measurements. We have treated SF with different concentrations of LA ranging from 1 mg/mL to 5mg/mL based on the LA concentrations found in the arthritic conditions. [45,46] In the **Figure 4.6a**, MSD of the tracer particle as a function of the lag time τ. The, the results suggest that, at low concentrations (~1 mg/mL), the behavior is similar to that of untreated HA solutions. However, as the concentration of LA increases, we observe a significant change in the microrheology of the sample. The MSD curves go from being sub-diffusive (slope < 1) to diffusive (slope ~1). This shows the transformation from a weakly connected network-like structure showing a viscoelastic behavior (shown in **Figure 4.6c)** with a restricted tracer particle movement to a low-viscosity Newtonian liquid due to the addition of LA in the SF (shown in **Figure 4.6d**) having a much larger tracer particle movement during the DWS expeirments. This observation can also be extended to the bulk rheology measurements as seen in **Figure 4.6b** wherein we see a drastic reduction in viscosity in both the low-shear as well as the high-shear regimes after the addition of LA in the SF. In particular, beyond the critical dosage of 1 mg/mL, micro and bulk rheology undergoes significant alterations. This result corresponds with clinical reports indicating that rheumatoid arthritis patients exhibit lactic acid concentrations of 3-5 mg/mL, whereas healthy individuals exhibit levels of 1 mg/mL.

Intuitively, such changes in the micro and bulk rheological properties provides a much deeper insight into the onset of the arthritic conditions during the hypoxic or anaerobic conditions of synovial joints under the influence of LA.

Further, the experiments shown above clearly suggest that the colloidal assembly of HA and proteins is responsible for the unique microrheology of the model SF, which was previously observed for pig-SF. Further, most of the commercially available artificial SF employ only

HA solutions to mitigate arthritic or joint freezing conditions.[35] In this direction, in order to investigate the microrheological effects of lactic acid (LA) on HA solution, the DWS experiments have been performed for 3.4 mg/mL HA with varied LA concentrations. particles.

The experiments uncover that increasing LA concentration influences the decay time of probe. **Figure 4.6e** show the MSD vs. τ data, which suggests that although the movement of the probe particles is sub-diffusive and hindered by a weak network-like structure, the mobility of the probe particles marginally increases with the increase in the concentration of LA. The pH is known to influence the molecular weight distribution of HA, which consequentially affects the strength and rigidity of the HA network resulting in the observed change in MSD. [17,47] The bulk rheology measurements also reflect similar trends as seen in the microrheological measurements of lactic acid-treated HA, as shown in **Figure 4.6f**. The effect of pH on the MW of HA results in a reduction in the viscosity of the HA solutions. It can be observed that at a very low lactic acid concentration (1mg/mL) both the microrheology and bulk rheology are similar to that of untreated HA. These concentrations are similar to physiological concentrations of lactic acid which does not seem to have any influence on the rheology of HA solutions. [23,48] The results indicate that, certainly, alongside HA the presence of the proteins in optimal proportions is necessary to emulate the microrheological properties of artificial SF.

4.3.3 Molecular Insight

Following this, we further investigated the molecular mechanism of the interaction of HA with higher MW proteins in presence of LA. In order to understand this behavior of HA-BSA complexes, we first look at the ζ-potential of BSA and HA with different concentrations of LA, as shown in **Figure 4.7a**. The BSA exhibits negative ζ-potential in the absence of LA, however, it shifts to positive ζ-potential through an isoelectric point, as the concentration of LA increases. On the contrary, HA exhibits negative ζ-potential in all the LA concentrations, which establishes a basis of an electrostatic interaction between BSA and HA in the presence of higher LA concentration. In order to further elucidate the effects of LA on albumin, we carry out circular dichroism (CD) measurements. **Figure 4.7b** shows the CD spectra of BSA in the presence of increasing LA concentrations. For BSA and BSA-HA samples, negative peaks at 208 nm and 222 nm are observed, which indicates the presence of α-helix structure for the protein.[49,50] The plots indicate that BSA retains its secondary structure in the presence of HA when it is treated with 1 mg/mL LA. However, in case of higher LA concentrations, it losses its α-helix structure and transform to a random coil, which has been confirmed by the loss of peak at 222 nm and increase in negative ellipticity at around 204 nm.[51,52] The experiment confirms that LA favors the unfolding of BSA, which eventually results in making it more accessible for charged amino acids to interact with negatively charged HA. The change in the secondary structure of BSA in the presence of high LA also corroborated with steady-state fluorescence emission of BSA. For this purpose, tryptophan fluorescence emission has been monitored to investigate the local conformation and change in the local environment near the indole ring of tryptophan present in BSA. Since the fluorescence intensity of a fluorophore is sensitive to its environment,[53] any change in the protein conformation around the indole ring of tryptophan affects the local environment vis-à-vis its fluorescence. Furthermore, the change or shift in the emission maxima of the tryptophan emission is indicative of whether the tryptophan residues are buried or solvent-exposed due to the conformational changes in the protein. **Figure 4.7c** depicts the steady-state emission of BSA tryptophan excited at 295 nm. The emission maxima observed for the tryptophan in BSA alone can be seen at 342 nm whereas a blue shift in the emission maxima ~6 nm and a decrease in the fluorescence intensity has been observed in the presence of LA (1−5 mg/mL). The blue shift in tryptophan emission suggests the change in the protein conformation, which leads to an increase in a non-polar environment near the indole ring of tryptophan. It may be noted here that with the increase in LA concentration, the pH of the solution decreases from 7.4 to 4 wherein there is a possibility to form the acid expanded form in proteins with molten globule-like conformation.[54–56] The prior -art also suggest that the BSA may undergoes an acid-induced unfolding that disrupt the hydrophobic binding pocket with further lowering pH down to 3.[56]

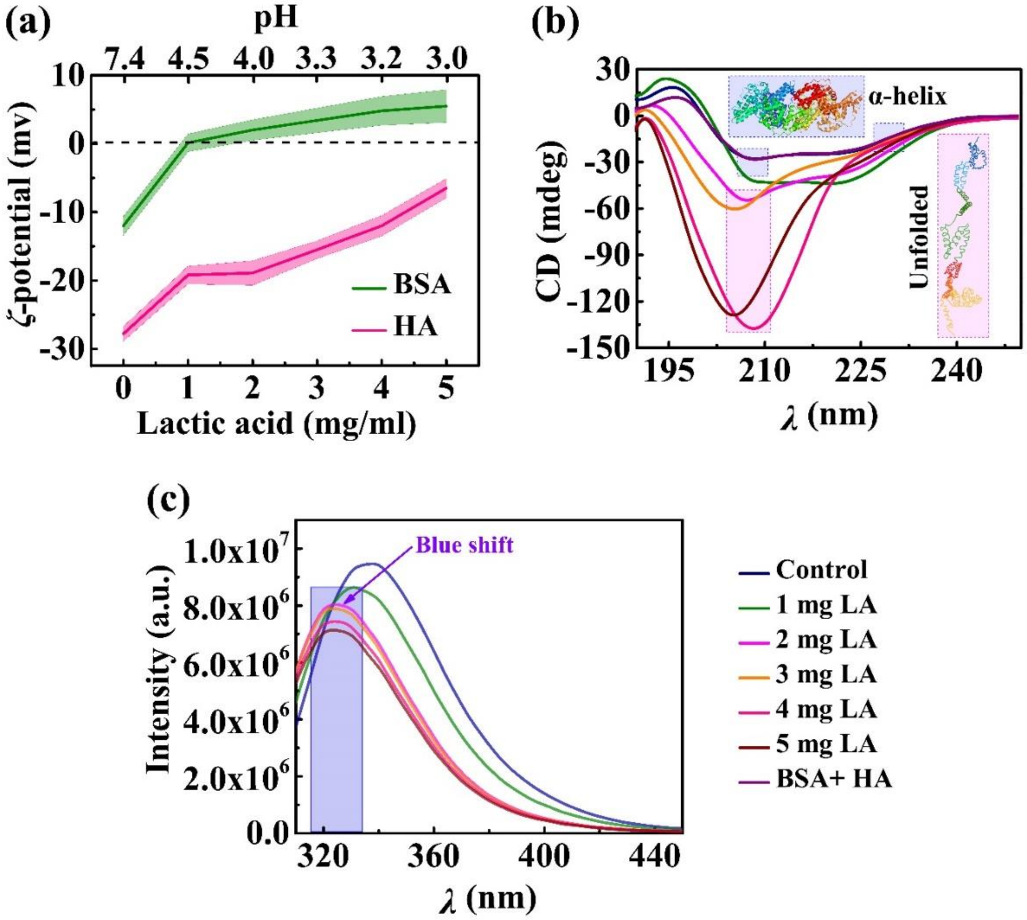

Figure 4.7. (a) ζ-potential of BSA and HA with varying concentrations of lactic acid treatment. (b) CD spectra of BSA with increasing LA. (c) Steady state fluorescence emission spectra of BSA with increasing LA.

Figure 4.8 schematically shows a summary of aforesaid event that may lead to protein-HA interaction in the presence of LA inside the synovium – (i) reduction of the pH of the SF with the increase in LA; (ii) unfolding of α-helix into a random coil and acquiring a positive ζ-potential for BSA; (iii) interaction of BSA with HA of negative ζ-potential; and (iv) co-precipitation beyond a critical mass from the SF to engender the loss of viscoelasticity.

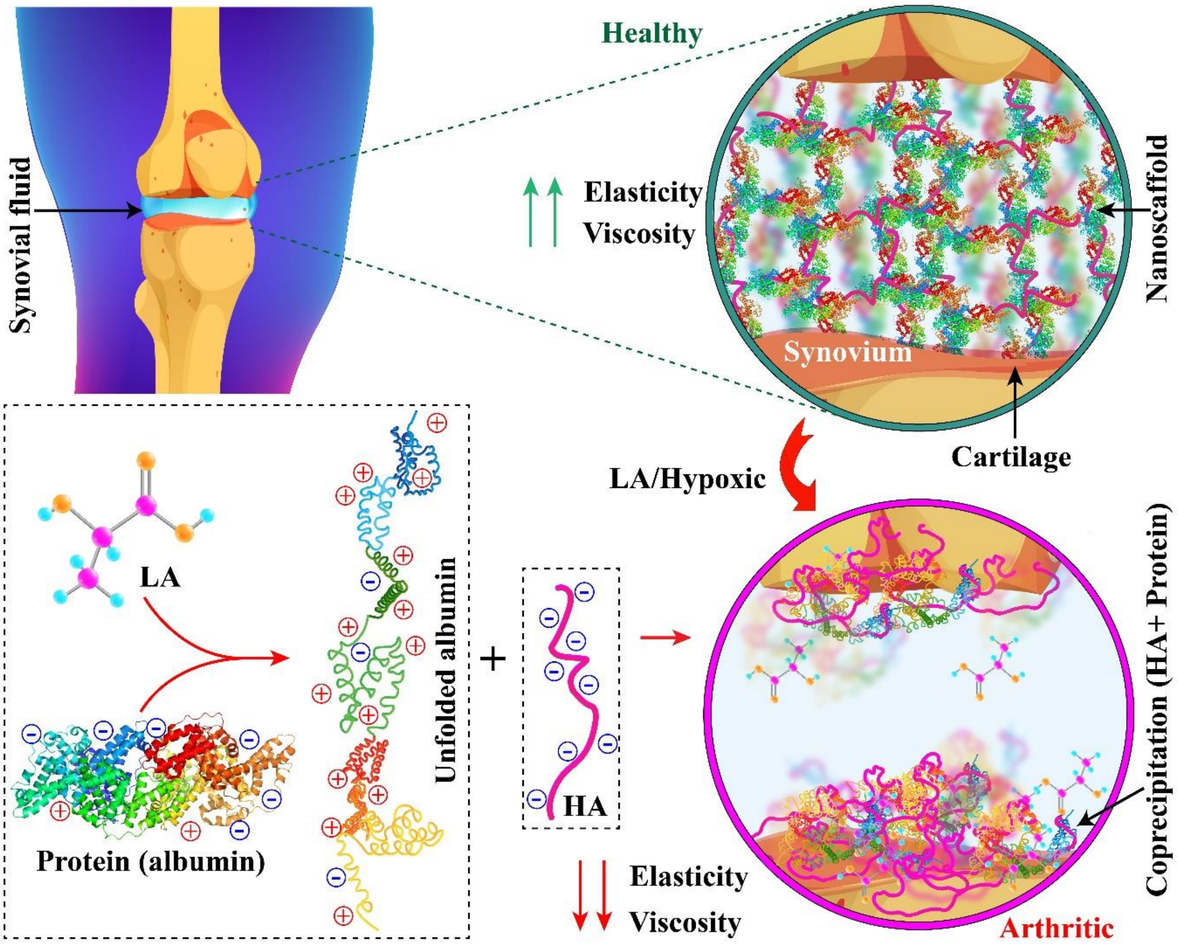

Figure 4.8. Schematic diagram of Protein-HA interaction in the presence of lactic acid inside the synovium. In the presence of LA, Protein (albumin) unfolds and possesses net positively charged patches, which interact with net negatively charged HA and coprecipitates.

4.4. Conclusions

In summary, the chapter uncovers that SF present inside the moving joints consists of an aqueous colloidal nanoscaffold composed of hyaluronic acid and proteins, which eventually provides a viscoelastic nature to the same. The weak colloidal assemblage of such biomaterials in the aqueous medium provide unique load bearing (elasticity) and resistance to wear and tear (Non-Newtonian fluidity) capacities to the SF during the joint movements. Interestingly, the experiments also uncover that SF is found to lose its viscoelastic behavior in the presence of LA. The, SDS-PAGE, gel-electrophoresis, and AFM studies together uncover that HA binds specifically with the high MW proteins of SF to co-precipitates in the presence of LA. The results are important from the perspective of anaerobic respiration in the synovium during hypoxic, arthritic, or excess workload conditions wherein LA is produced aplenty.

The control experiments suggest that such microrheological transformation is absent when pure HA or proteins are treated with LA. Subsequently, in line with the aforesaid observations, an artificial SF has been biosynthesized by mixing aqueous HA solution with albumin and γ-globulin which displays precipitates under microscope when treated with lactic acid. The micro and bulk rheology experiments uncover that the destruction of the colloidal nano-scaffolds of the pig- and artificial SFs leads to a fluid with very less elasticity (low load bearing capacity) and viscosity (fluidity of joints and resistance to wear and tear). The ζ-potential analysis reveals that BSA becomes positively charged when treated with a higher amount of LA to bind with a negatively charged HA to engender the phenomenon. Further, CD spectra of LA-treated BSA reveals that the LA induce unfolding of BSA favors the electrostatic interaction with HA due to elevated exposures of charged amino acids. Concisely, the study establishes that LA enable co-precipitation of HA and higher MW proteins can cause complete loss of viscoelasticity, leading to severe arthritic or joint freezing conditions when the anaerobic respiration rates at the joins are on the higher side. The results reported also indicates the hyaluronic acid based injections might not be effective as an articular viscosupplement for rheumatoid arthritis conditions which has an elevated lactic acid levels.

References

(1) Schurz, J.; Ribitsch, V. Rheology of Synovial Fluid. *Biorheology* **1987**, *24*, 385–399. https://doi.org/10.3233/BIR-1987-24404.

(2) Lai, S. K.; Wang, Y.-Y.; Wirtz, D.; Hanes, J. Micro- and Macrorheology of Mucus. *Adv. Drug Deliv. Rev.* **2009**, *61* (2), 86–100. https://doi.org/10.1016/j.addr.2008.09.012.

(3) Staunton, J. R.; So, W. Y.; Paul, C. D.; Tanner, K. High-Frequency Microrheology in 3D Reveals Mismatch between Cytoskeletal and Extracellular Matrix Mechanics. *Proc. Natl. Acad. Sci.* **2019**, *116* (29), 14448–14455. https://doi.org/10.1073/pnas.1814271116.

(4) Jay, G. D.; Torres, J. R.; Warman, M. L.; Laderer, M. C.; Breuer, K. S. The Role of Lubricin in the Mechanical Behavior of Synovial Fluid. *Proc. Natl. Acad. Sci.* **2007**, *104* (15), 6194–6199. https://doi.org/10.1073/pnas.0608558104.

(5) Brannan, S. R.; Jerrard, D. A. Synovial Fluid Analysis. *J. Emerg. Med.* **2006**, *30* (3), 331–339. https://doi.org/10.1016/j.jemermed.2005.05.029.

(6) Bortel, E. L.; Charbonnier, B.; Heuberger, R. Development of a Synthetic Synovial Fluid for Tribological Testing. *Lubricants* **2015**, *3* (4), 664–686. https://doi.org/10.3390/lubricants3040664.

(7) Krishna, D. V.; Sankar, M. R. Bioinspired Artificial Synovial Fluid for in Vitro Frictional Behavior of Bovine Articular Cartilage and Auxiliary Biomaterials. *J. Mol. Liq.* **2023**, *388*, 122836. https://doi.org/https://doi.org/10.1016/j.molliq.2023.122836.

(8) Yin, R.; Su, J.; Colville, M.; Paszek, M.; Reesink, H. Synovial Fluid Microrheology to Identify Potential Candidates for Viscosupplementation. *Osteoarthr. Cartil.* **2019**, *27* (2019), S481. https://doi.org/10.1016/j.joca.2019.02.530.

(9) DECKER, B.; McGUCKIN, W. F.; McKENZIE, B. F.; SLOCUMB, C. H. Concentration of Hyaluronic Acid in Synovial Fluid. *Clin. Chem.* **1959**, *5*, 465–469.

(10) Ropes, M. W.; Rossmeisl, E. C.; Bauer, W. THE ORIGIN AND NATURE OF NORMAL HUMAN SYNOVIAL FLUID. *J. Clin. Invest.* **1940**, *19* (6), 795–799. https://doi.org/10.1172/JCI101182.

(11) Zhang, Z.; Barman, S.; Christopher, G. F. The Role of Protein Content on the Steady and Oscillatory Shear Rheology of Model Synovial Fluids. *Soft Matter* **2014**, *10* (32), 5965–5973. https://doi.org/10.1039/c4sm00716f.

(12) Toole, B. P. Hyaluronan: From Extracellular Glue to Pericellular Cue. *Nat. Rev. Cancer* **2004**, *4* (7), 528–539. https://doi.org/10.1038/nrc1391.

(13) Lapcík L Jr and, L.; Lapcík, L.; De Smedt, S.; Demeester, J.; Chabrecek, P. Hyaluronan: Preparation, Structure, Properties, and Applications. *Chem. Rev.* **1998**, *98* (8), 2663–2684. https://doi.org/10.1021/cr941199z.

(14) Kim, H.; Jeong, H.; Han, S.; Beack, S.; Hwang, B. W.; Shin, M.; Oh, S. S.; Hahn, S. K. Hyaluronate and Its Derivatives for Customized Biomedical Applications. *Biomaterials* **2017**, *123*, 155–171. https://doi.org/10.1016/j.biomaterials.2017.01.029.

(15) Laurent, T. C.; Fraser, J. R. E.; Laurent, U. B. G.; Engström-Laurent, A. Hyaluronan in Inflammatory Joint Disease. *Acta Orthop.* **1995**, *66* (S266), 116–120. https://doi.org/10.3109/17453679509157665.

(16) Kirwan, J. R.; Rankin, E. Intra-Articular Therapy in Osteoarthritis. *Baillieres. Clin. Rheumatol.* **1997**, *11* (4), 769–794. https://doi.org/10.1016/s0950-3579(97)80009-x.

(17) Fam, H.; Kontopoulou, M.; Bryant, J. T. Effect of Concentration and Molecular Weight on the Rheology of Hyaluronic Acid/Bovine Calf Serum Solutions. *Biorheology* **2009**, *46* (1), 31–43. https://doi.org/10.3233/BIR-2009-0521.

(18) Liu, Z.; Lin, W.; Fan, Y.; Kampf, N.; Wang, Y.; Klein, J. Effects of Hyaluronan Molecular Weight on the Lubrication of Cartilage-Emulating Boundary Layers. *Biomacromolecules* **2020**, *21* (10), 4345–4354. https://doi.org/10.1021/acs.biomac.0c01151.

(19) Sacks, J. J.; Luo, Y.-H.; Helmick, C. G. Prevalence of Specific Types of Arthritis and Other Rheumatic Conditions in the Ambulatory Health Care System in the United States, 2001–2005. *Arthritis Care \& Res.* **2010**, *62* (4), 460–464. https://doi.org/https://doi.org/10.1002/acr.20041.

(20) Buckwalter, J. A.; Saltzman, C.; Brown, T. The Impact of Osteoarthritis: Implications for Research. *Clin. Orthop. Relat. Res.* **2004**, *427*.

(21) Bijlsma, J. W. J.; Berenbaum, F.; Lafeber, F. P. J. G. Osteoarthritis: An Update with Relevance for Clinical Practice. *Lancet* **2011**, *377* (9783), 2115–2126. https://doi.org/https://doi.org/10.1016/S0140-6736(11)60243-2.

(22) Firestein, G. S. Evolving Concepts of Rheumatoid Arthritis. *Nature* **2003**, *423* (6937), 356–361. https://doi.org/10.1038/nature01661.

(23) Gobelet, C.; Gerster, J. C. Synovial Fluid Lactate Levels in Septic and Non-Septic Arthritides. *Ann. Rheum. Dis.* **1984**, *43* (5), 742–745. https://doi.org/10.1136/ard.43.5.742.

(24) Chang, X.; Wei, C. Glycolysis and Rheumatoid Arthritis. *Int. J. Rheum. Dis.* **2011**, *14* (3), 217–222. https://doi.org/10.1111/j.1756-185X.2011.01598.x.

(25) Quiñonez-Flores, C. M.; González-Chávez, S. A.; Pacheco-Tena, C. Hypoxia and Its

Implications in Rheumatoid Arthritis. *J. Biomed. Sci.* **2016**, *23* (1), 62. https://doi.org/10.1186/s12929-016-0281-0.

(26) Garcia-Carbonell, R.; Divakaruni, A. S.; Lodi, A.; Vicente-Suarez, I.; Saha, A.; Cheroutre, H.; Boss, G. R.; Tiziani, S.; Murphy, A. N.; Guma, M. Critical Role of Glucose Metabolism in Rheumatoid Arthritis Fibroblast-like Synoviocytes. *Arthritis and Rheumatology*. 2016, pp 1614–1626. https://doi.org/10.1002/art.39608.

(27) Zou, Y.; Zeng, S.; Huang, M.; Qiu, Q.; Xiao, Y.; Shi, M.; Zhan, Z.; Liang, L.; Yang, X.; Xu, H. Inhibition of 6-Phosphofructo-2-Kinase Suppresses Fibroblast-like Synoviocytes-Mediated Synovial Inflammation and Joint Destruction in Rheumatoid Arthritis. *Br. J. Pharmacol.* **2017**, *174* (9), 893–908. https://doi.org/10.1111/bph.13762.

(28) Shime, H.; Yabu, M.; Akazawa, T.; Kodama, K.; Matsumoto, M.; Seya, T.; Inoue, N. Tumor-Secreted Lactic Acid Promotes IL-23/IL-17 Proinflammatory Pathway. *J. Immunol.* **2008**, *180* (11), 7175–7183. https://doi.org/10.4049/jimmunol.180.11.7175.

(29) Haas, R.; Smith, J.; Rocher-Ros, V.; Nadkarni, S.; Montero-Melendez, T.; D'Acquisto, F.; Bland, E. J.; Bombardieri, M.; Pitzalis, C.; Perretti, M.; Marelli-Berg, F. M.; Mauro, C. Lactate Regulates Metabolic and Pro-Inflammatory Circuits in Control of T Cell Migration and Effector Functions. *PLOS Biol.* **2015**, *13* (7), 1–24. https://doi.org/10.1371/journal.pbio.1002202.

(30) Dröge, W.; Roth, S.; Altmann, A.; Mihm, S. Regulation of T-Cell Functions by l-Lactate. *Cell. Immunol.* **1987**, *108* (2), 405–416. https://doi.org/https://doi.org/10.1016/0008-8749(87)90223-1.

(31) Pucino, V.; Certo, M.; Bulusu, V.; Cucchi, D.; Goldmann, K.; Pontarini, E.; Haas, R.; Smith, J.; Headland, S. E.; Blighe, K.; Ruscica, M.; Humby, F.; Lewis, M. J.; Kamphorst, J. J.; Bombardieri, M.; Pitzalis, C.; Mauro, C. Lactate Buildup at the Site of Chronic Inflammation Promotes Disease by Inducing CD4+ T Cell Metabolic Rewiring. *Cell Metab.* **2019**, *30* (6), 1055-1074.e8. https://doi.org/https://doi.org/10.1016/j.cmet.2019.10.004.

(32) DIMMER, K.-S.; FRIEDRICH, B.; LANG, F.; DEITMER, J. W.; BRÖER, S. The Low-Affinity Monocarboxylate Transporter MCT4 Is Adapted to the Export of Lactate in Highly Glycolytic Cells. *Biochem. J.* **2000**, *350* (1), 219–227. https://doi.org/10.1042/bj3500219.

(33) Manning Fox, J. E.; Meredith, D.; Halestrap, A. P. Characterisation of Human Monocarboxylate Transporter 4 Substantiates Its Role in Lactic Acid Efflux from Skeletal Muscle. *J. Physiol.* **2000**, *529 Pt 2* (Pt 2), 285–293. https://doi.org/10.1111/j.1469-7793.2000.00285.x.

(34) Pucino, V.; Nefla, M.; Gauthier, V.; Alsaleh, G.; Clayton, S. A.; Marshall, J.; Filer, A.; Clark, A. R.; Raza, K.; Buckley, C. D. Differential Effect of Lactate on Synovial Fibroblast and Macrophage Effector Functions. *Front. Immunol.* **2023**, *14*. https://doi.org/10.3389/fimmu.2023.1183825.

(35) Gonzales, G.; Zauscher, S.; Varghese, S. Progress in the Design and Synthesis of Viscosupplements for Articular Joint Lubrication. *Curr. Opin. Colloid Interface Sci.* **2023**, *66*, 101708. https://doi.org/https://doi.org/10.1016/j.cocis.2023.101708.

(36) Rothammer, B.; Marian, M.; Rummel, F.; Schroeder, S.; Uhler, M.; Kretzer, J. P.; Tremmel, S.; Wartzack, S. Rheological Behavior of an Artificial Synovial Fluid – Influence of Temperature, Shear Rate and Pressure. *J. Mech. Behav. Biomed. Mater.* **2021**, *115*, 104278. https://doi.org/https://doi.org/10.1016/j.jmbbm.2020.104278.

(37) Oates, K. M. N.; Krause, W. E.; Jones, R. L.; Colby, R. H. Rheopexy of Synovial Fluid and Protein Aggregation. *J. R. Soc. Interface* **2006**, *3* (6), 167–174. https://doi.org/10.1098/rsif.2005.0086.

(38) Du, X.; Dubin, P. L.; Hoagland, D. A.; Sun, L. Protein-Selective Coacervation with Hyaluronic Acid. *Biomacromolecules* **2014**, *15* (3), 726–734. https://doi.org/10.1021/bm500041a.

(39) Bansil, R.; Stanley, E.; Thomas LaMont, J. Mucin Biophysics. *Annu. Rev. Physiol.* **1995**, *57* (84), 635–657. https://doi.org/10.1146/annurev.ph.57.030195.003223.

(40) Waigh, T. A. Advances in the Microrheology of Complex Fluids. *Reports Prog. Phys.* **2016**, *79* (7). https://doi.org/10.1088/0034-4885/79/7/074601.

(41) Weitz, D.; Brown, D. P.-W.; Ed, undefined; 1993, undefined. Dynamic Light Scattering.

(42) Mason, T. G.; Weitz, D. A. Optical Measurements of Frequency-Dependent Linear Viscoelastic Moduli of Complex Fluids. *Phys. Rev. Lett.* **1995**, *74* (7), 1250–1253. https://doi.org/10.1103/PhysRevLett.74.1250.

(43) Mason, T. G.; Gang, H.; Weitz, D. A. Diffusing-Wave-Spectroscopy Measurements of Viscoelasticity of Complex Fluids. *J. Opt. Soc. Am. A* **1997**, *14* (1), 139. https://doi.org/10.1364/josaa.14.000139.

(44) Sambrook, J.; Fritsch, E. F.; Maniatis, T. *Molecular Cloning: A Laboratory Manual.*; Cold spring harbor laboratory press, 1989.

(45) Gobelet, C.; Gerster, J. C. Synovial Fluid Lactate Levels in Septic and Non-Septic Arthritides. *Ann. Rheum. Dis.* **1984**, *43* (5), 742–745. https://doi.org/10.1136/ard.43.5.742.

(46) Proot, J. L. J.; De Vicente, F.; Sheahan, D. E. Analysis of Lactate Concentrations in Canine Synovial Fluid. *Vet. Comp. Orthop. Traumatol.* **2015**, *28* (5), 301–305. https://doi.org/10.3415/VCOT-15-01-0007.

(47) Maleki, A.; Kjøniksen, A. L.; Nyström, B. Effect of PH on the Behavior of Hyaluronic Acid in Dilute and Semidilute Aqueous Solutions. *Macromol. Symp.* **2008**, *274* (1), 131–140. https://doi.org/10.1002/masy.200851418.

(48) Eugene Arthur, R.; Stern, M.; Galeazzi, M.; Baldassare, A. R.; Weiss, T. D.; Rogers, J. R.; Zuckner, J. Synovial Fluid Lactic Acid in Septic and Nonseptic Arthritis. *Arthritis Rheum.* **1983**, *26* (12), 1499–1505. https://doi.org/10.1002/art.1780261212.

(49) Li, R.; Wu, Z.; Wangb, Y.; Ding, L.; Wang, Y. Role of PH-Induced Structural Change in Protein Aggregation in Foam Fractionation of Bovine Serum Albumin. *Biotechnol.*

Reports **2016**, *9*, 46–52. https://doi.org/10.1016/j.btre.2016.01.002.

(50) El Kadi, N.; Taulier, N.; Le Huérou, J. Y.; Gindre, M.; Urbach, W.; Nwigwe, I.; Kahn, P. C.; Waks, M. Unfolding and Refolding of Bovine Serum Albumin at Acid PH: Ultrasound and Structural Studies. *Biophys. J.* **2006**, *91* (9), 3397–3404. https://doi.org/10.1529/biophysj.106.088963.

(51) Konno, T.; Tanaka, N.; Kataoka, M.; Takano, E.; Maki, M. A Circular Dichroism Study of Preferential Hydration and Alcohol Effects on a Denatured Protein, Pig Calpastatin Domain I. *Biochim. Biophys. Acta* **1997**, *1342* (1), 73–82. https://doi.org/10.1016/s0167-4838(97)00092-7.

(52) Barbero, N.; Coletti, M.; Catalano, F.; Visentin, S. Exploring Gold Nanoparticles Interaction with Mucins: A Spectroscopic-Based Study. *Int. J. Pharm.* **2018**, *535* (1–2), 438–443. https://doi.org/10.1016/j.ijpharm.2017.11.026.

(53) Lakowicz, J. Instrumentation for Fluorescence Spectroscopy. In *Principles of Fluorescence Spectroscopy*; Lakowicz, J. R., Ed.; Springer US: Boston, MA, 2006; pp 27–61. https://doi.org/10.1007/978-0-387-46312-4_2.

(54) Dockal, M.; Carter, D. C.; Rüker, F. Conformational Transitions of the Three Recombinant Domains of Human Serum Albumin Depending on PH*. *J. Biol. Chem.* **2000**, *275* (5), 3042–3050. https://doi.org/https://doi.org/10.1074/jbc.275.5.3042.

(55) Semisotnov, G. V; Rodionova, N. A.; Razgulyaev, O. I.; Uversky, V. N.; Gripas', A. F.; Gilmanshin, R. I. Study of the "Molten Globule" Intermediate State in Protein Folding by a Hydrophobic Fluorescent Probe. *Biopolymers* **1991**, *31* (1), 119–128. https://doi.org/https://doi.org/10.1002/bip.360310111.

(56) Bhattacharya, M.; Jain, N.; Bhasne, K.; Kumari, V.; Mukhopadhyay, S. PH-Induced Conformational Isomerization of Bovine Serum Albumin Studied by Extrinsic and Intrinsic Protein Fluorescence. *J. Fluoresc.* **2011**, *21* (3), 1083–1090. https://doi.org/10.1007/s10895-010-0781-3.

CHAPTER 5

Designing an Articular Viscosupplement for Rheumatoid Arthritis Using Microrheological Analysis

Contents

ABSTRACT

Rheumatoid arthritis (RA) is a prevalent joint disease that affects people across a wide range of ages. In RA, the viscoelastic properties of synovial fluid (SF) are significantly compromised, reducing its ability to protect cartilage surfaces during joint movements. Due to hypoxia and anaerobic respiration, elevated lactic acid levels severely damage the native nanostructures of synovial fluid. Unlike osteoarthritis, hyaluronic acid (HA) viscosupplements are unsuitable for RA treatment as they are prone to degradation in the acidic environment of RA-affected joints. Therefore, there is a need to develop viscosupplements that can maintain their viscoelastic properties in elevated lactic acid conditions. This chapter investigates the microrheology of mucin-blended HA in a simulated RA environment. Atomic force microscopy (AFM) studies reveal that the addition of mucin to HA creates a fiber bundle-like structure, which resists deformation under shear stress, in contrast to the fiber-like structure of pure HA, which deforms more readily. Additionally, interfacial microrheology using a confocal laser scanning microscope shows that mucin-blended HA enhances boundary lubrication and joint mobility by reducing the interaction between HA and the cartilage surface.

5.1. Introduction

The Human body is an interconnected network of various systems amongst which the most important is the musculoskeletal system which consists mainly of bones and connective tissue. The main function of the musculoskeletal system is to provide a definite internal shapeand structure.[1] Bones are organs constructed from dense connective tissues, primarily collagen,which is a durable protein.[2] The movement of any bone in the body is facilitated through different types of joints. One such junction joint cavity is formed of skeletal elements surrounded by synovial tissues on the periphery of the cavity where a semi-gelled material, known as synovial fluid, is present which is secreted by the synovial membrane.[3] Synovial fluid (SF) is a bio-lubricant with unique viscoelastic properties crucial to maintaining joint health and absorbing shocks during movement.[4] For instance, it demonstrates shear thinning under low stress, allowing for fluid-like movement of the joints. Conversely, it offers high viscous resistance under high stress, displaying shear thickening behavior, which helps reduce friction between the joints.[5,6] The key component of synovial fluid is a high molecular weight glycosaminoglycan hyaluronic acid (HA), which is responsible for these characteristics.[5,7,8] Apart from this SF also contains albumin, immunoglobulin, and lubricin, which impart elastic as well as boundary lubrication properties.[9,10] The distinctive viscoelastic properties of the synovial fluid arise from its complex microstructure, which is formed by a synergistic interplay of all its constituents. Alteration of this complex viscoelasticity leads to various disease conditions like osteoarthritis (OA), and rheumatoid arthritis (RA).[4] Interestingly, OA is a degenerative disease where the synovial fluid and the cartilage are degraded at the late stage of life which results in increased bone-bone contact and severe pain. This often necessitates surgeries like total knee replacements.[11] Another emerging therapeutic intervention is the administration of HA-based injections to bolster joint lubrication.[12,13] HA cushions the cartilage tissue and promotes its regeneration. Unlike osteoarthritis, RA is an autoimmune disease and can happen at any stage of life, causing inflammation of joints and the loss of viscoelasticity of synovial fluid.[14,15] Treatment options are primarily based on the administration of anti-inflammatory drugs and in severe cases, joint replacement is required.[16,17] In this case, HA-based injections are not used as the inflamed joints accelerate the degradation of HA, rendering the treatment ineffective.[18,19] Interestingly, RA-affected joints have elevated lactic acid concentrations which results from the increased upregulation of lactate dehydrogenase and downregulation of pyruvate dehydrogenase.[20–22] The elevated lactic acid also acts as a proinflammatory signal and enhances IL-17 and IL-23 pathways.[23,24] Additionally, due to the rise in acidic environment, HA precipitates with the protein components of the synovial fluid.[25–29] This renders HA-based injections ineffective in RA patients. The emergence of microrheology can aid in the development of artificial SF, generally known as articular viscosupplements, which can restore normal joint physiology in arthritic patients.[30] Clinical evidence supports the efficacy of viscosupplements, where administration of a hyaluronic acid viscosupplement helped in the restoration of joint mobility as well as lowered inflammatory cytokines such as IL-1β, and TNF-α.[31] Integration of anti-inflammatory drugs with the viscosupplement such as diclofenac sodium (DF) can further reduce inflammation-induced discomfort and improve overall joint physiology.[32] The combination therapy of biotin, vitamin C, and hyaluronic acid also resulted in decreased inflammation as well and restored joint mobility.[33] The generation of free radicals can be deleterious to the long-term efficacy of viscosupplements in osteoarthritic patients. The introduction of HA with a free radical scavenger, sorbitol, reveals that the viscosupplement formulation is protected from the attack of free radicals, and it has better lubricating capabilities resembling those of the

SF because of the high concentration of HA.[34] However, these viscosupplements are ineffective in RA patients due to acidic synovial joints.[19] Therefore, there is an urgent need to develop new viscosupplements that can preserve their viscoelastic properties in the changed biochemical environment of rheumatoid arthritic joints, hence increasing the efficacy of treatments aimed at restoring joint function.

In this chapter, we utilize diffusing wave spectroscopy (DWS) to examine the microrheology of prepared viscosupplements. We study both the microrheological and bulk rheological properties of hyaluronic acid (HA) over four pH settings relevant to the clinical pH ranges found in rheumatoid arthritis (RA) patients. Subsequently, HA is blended with proteoglycan mucin, and the microrheology of this mixture. We then conducted microrheological tests using mucin-blended HA and ionic liquid-blended HA in simulated RA joint settings. Atomic force microscopy (AFM) was applied to visualize the microstructure of the mixed hyaluronic acids. Finally, the interfacial microrheology is performed between collagen and viscosupplements using confocal laser scanning microscopy which helps in understanding the boundary lubrication properties. These findings add to a better understanding of the obstacles in maintaining synovial fluid functionality in diseased states and promote the development of more effective therapy methods for RA patients.

5.2. Experimental Section

5.2.1. Materials

The sodium salt of hyaluronic acid, γ-globulin, mucin (type2), and L-lactic acid was purchased from Sigma-Aldrich Pvt. Ltd. Bovine serum albumin (98% pure) was acquired from Sisco Research Laboratories Pvt. Ltd (SRL). The 510 nm (10%) polystyrene tracer particle diameter sample was acquired from LS Instruments AG, Switzerland. 510 nm and 1 µm fluosphere particles were obtained from Thermo Fisher Scientific. Collagen 1 solution was obtained from ibidi. All the compounds were used without any additional purification. The preparation of solutions in all tests was done using Milli-Q water.

5.2.2. Formulation of Mucin Blended Hyaluronic acid

Initially, a hyaluronic acid solution was prepared in 10 mM phosphate buffer at a pH of 7.4. Model synovial fluid was prepared using a previously described technique, in which 10 mg/mL BSA and 0.5 mg/mL were mixed with 3.4 mg/mL HA solution in a rocker overnight.[9] To prepare HA-Muc and SF-Muc solution was prepared by mixing 10mg/mL mucin in either HA or model SF solution. For the pH experiments, 10 mM phosphate buffer was used. To investigate the microrheology of the lactic acid treated viscosupplemnts 3 mg/mL, lactic acid is added to the HA, HA-Muc, SF, and SF-Muc solutions. Prior to microrheology measurement, 80 µL of polystyrene tracer particles were placed in 920 µL of the prepared sample. The tracer particle concentration was 0.8% in all microrheological studies and did not impact the overall experimental outcomes. All the measurements were conducted thrice for the precision and reproducibility of the data.

5.2.3. Synovial Fluid Sample from Pig Joint

The porcine SF from a healthy joint of a pig was obtained from ICAR- National Research Centre on Pig situated in Guwahati, India. For the aspiration of pig SF 18-gauge needle was used and avoided any blood contamination. As the sample volume was minimal, the pig SF was then diluted 2 times with 10 mM phosphate buffer saline (PBS) at pH 7.4. To investigate the effects of LA on pig SF, LA was added to it with a final concentration of 5mg/mL. For the Field Emission Scanning Electron microscopy (FESEM) analysis, lactic acid treated and untreated pig SF was kept at -20°C for 1 week followed by lyophilization. Prior to FESEM imaging samples were sputter coated with gold to make the sample surface conductive.

5.2.4. DWS Microrheology

Diffusing wave spectroscopy (DWS) was utilized for all microrheological measurements, employing a light scattering technique to analyze the microrheology of turbid samples. In order to make the sample turbid, 80 µL of 10% polystyrene tracer particles with a diameter of 510 nm were added. Before measurements, the samples were placed in a 2 mm cuvette and incubated for 10 min at 37°C in the instrument's sample holder. The microrheology measurements were conducted using the DWS RheoLab instrument from LS Instruments AG, Switzerland. In the DWS instrument, a laser with a 685 nm wavelength is directed at the cuvette containing the sample. Due to the Brownian motion of the tracer particles, the scattered light fluctuates in intensity over time. A correlator measures the intensity correlation function (ICF) $\left[g_2(\tau)-1\right]$, which is used to calculate the ensemble-averaged mean squared displacement (MSD) of the tracer particles, represented as $\left\langle \Delta r^2(\tau)\right\rangle$. The relationship between the MSD and the lag time (τ) for particles undergoing Brownian motion in a viscoelastic fluid is expressed as follows—

$$\left\langle \Delta r^2(\tau)\right\rangle = 2nD_t\tau^{\alpha}. \tag{1}$$

Where D_t represents the time-dependent diffusivity of the tracer particle, and $0 < \alpha < 1$, n refers to the dimensionality (n =3 for a 3-dimensional analysis). For a tracer particle diffusing in a purely viscous environment, the exponent $\alpha = 1$, and the diffusion coefficient D of the probe is inversely related to the viscosity (η) of the surrounding liquid. The viscoelastic modulus can be determined from the mean square displacement (MSD) using the generalized Stokes-Einstein equation—

$$G(s)=\frac{k_B T}{\pi a s\left\langle \Delta r^2(s)\right\rangle}. \qquad (2)$$

Here, $G(s)$ represents the Laplace transform of the viscoelastic relaxation modulus $G(t)$, while $\left\langle \Delta r^2(s)\right\rangle$, corresponds to the Laplace transform of the mean square displacement (MSD). In this equation, k_B is the Boltzmann constant, T is the absolute temperature, and a is the radius of the tracer particle. By substituting s with $i\omega$, the complex modulus $\left(G^*(\omega)\right)$ and the complex viscosity $\left(\eta^*(\omega)=G^*(\omega)/\omega\right)$ can be derived.

5.2.5. Morphology analysis via AFM

The morphological examination of HA and HA-Muc was investigated by employing AFM (Cypher Asylum, Oxford). For this, we diluted the samples 100 times and drop cast on a freshly cleaved silicon wafer of size 5 mm × 8 mm and allowed to settle for 15 min. Subsequently, samples were dried under a vacuum desiccator overnight. The scan rate was kept at 0.5 to 1 Hz and the set point was around 500 mV. Comparative analysis was performed for scan areas of 2 μm^2 and 5 μm^2 for both HA and HA-Muc samples.

5.2.6. Bulk Rheology

For bulk rheology investigations, Anton Paar MCR 301 Rheometer was employed. The measurements were conducted using a 50 mm diameter 1-degree cone and plate geometry at 37°C. All the measurements are conducted in triplicates and the mean data is presented along with standard deviations.

5.2.7 Interfacial Microrheology

Interfacial microrheology between the collagen surface and the prepared HA and HA-Mucin solutions was conducted using a confocal laser scanning microscope. Before the experiment, a thin layer of collagen was prepared on a 15-μ slide ibidi (bioinert) plate with a glass bottom and incubated for 15 min. Following this, the HA or HA-Mucin solution was added to the collagen surface. Prior to collagen gelation, 1 µm fluorescent particles were added, and 500 nm fluorescent particles were incorporated into the HA or HA-Mucin solution. The confocal microscope, equipped with a pinhole aperture, enabled precise focus on a specific plane. Fluorescence signals from the green particles embedded in the collagen and the red particles in the viscosupplement (either HA or HA-Muc) solution allowed visualization of the collagen-viscosupplement interface. The excitation and emission of green and red particles were 505/515 and 580/605 respectively. Temperature was maintained at 37°C using a Peltier unit. Particle tracking measurements over time were conducted for both HA and HA-Mucin solutions at the near interface and the upper interface. Subsequently, time series images were used to calculate the mean squared displacements using a freely available MATLAB code. All the measurements were taken three times and mean data was presented with standard deviations.

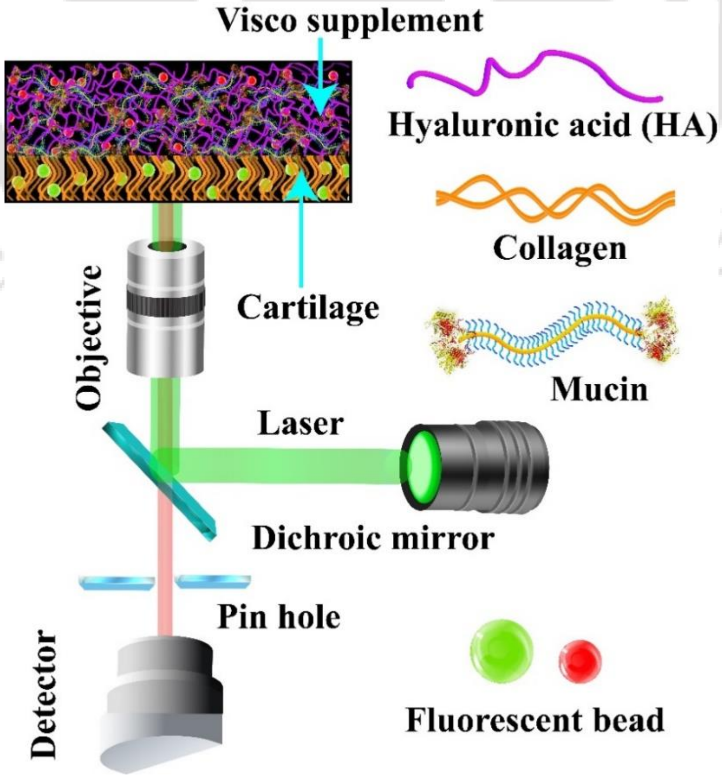

Figure 5.1. Instrumental measurement setup of multiple particle tracking microrheology at the collagen and HA-Muc viscosupplement interface.

5.2.8. Computational Model

A computational model was developed to simulate the experimental system. In this direction, a single-phase multicomponent laminar flow system was considered. Here, high-viscous and low-viscous fluids were taken as incompressible, Newtonian, and miscible fluids. The governing continuity and Navier-Stokes equations are described as,

$$\nabla \cdot \mathbf{u}_i = 0, \tag{3}$$

$$\rho_i \left(\dot{\mathbf{u}}_i + \mathbf{u}_i \cdot \nabla \mathbf{u}_i \right) = -\nabla p + \nabla \cdot \left(\mu_i \left(\nabla \mathbf{u}_i + \left(\nabla \mathbf{u}_i \right)^T \right) \right) + \mathbf{F}, \tag{4}$$

where, the subscript '*i*' denotes high viscosity fluid (*i*=1) near wall or low viscosity fluid (*i* =2) at the centre and over dot denotes the time derivative. Eq (3) is the continuity equation, whereas eq(4) is the momentum balance equation. The symbols $\mathbf{u}_i, p_i, \rho_i, \mu_i, \mathbf{F}$, t, and ∇ denote the velocity vector, pressure, density, dynamic viscosity, body force, time, and gradient operator respectively. Eq(4) can be simplified to the following equation,

$$\rho_i \left(\dot{\mathbf{u}}_i + \mathbf{u}_i \cdot \nabla \mathbf{u}_i \right) = -\nabla p_i + \mu_i \nabla^2 \mathbf{u}_i . \tag{5}$$

In the left-hand side of eq(5), the first term represents the local temporal acceleration and the second term represents convective acceleration. The right-hand side expresses the pressure gradient of the fluid flow and the viscous diffusion term. Here, the body force term is neglected as the fluid is flowing in the horizontal direction. A finite-element-based COMSOL 6.0 Multiphysics was used to solve the two-dimensional (2D) governing equations. The computational domain for this system was divided into ~3678 triangular meshes to obtain grid-independent solutions. The time step was set to be 10^{-9} s. No velocity was given at the inlet and outlet, and zero pressure gauge boundary conditions were enforced. The microchannel walls on both sides were given a slip velocity and sliding with similar positive x-directional velocities.

We examine lubrication and velocity profiles under two distinct scenarios, referred to as Case A and Case B. Here, μ_{ij} denotes high viscosity fluid (i =1, j =A, B) near wall, and μ_{ij} low viscosity fluid (i =2, j =A, B) at the centre as explained in case A and case B respectively. Both scenarios are examined in detail in the results and discussion section. For the high-low viscous fluid system, the values for the flow parameters were considered to be as follows: $\rho_i = 1000 \text{ kg/m}^3$, μ_{r1} = the viscosity ratio of high viscous fluid to low viscous one $= \mu_{1A}/\mu_{2A} = 1/0.01 = 100$, for the first case (case A), when the sliding velocities of the walls were $V_{r1} = 5 \text{ μm/s}$, and in the second case (case B), where $\mu_{r2} = \mu_{1B}/\mu_{2B} = 0.4/0.04 = 10$, the sliding velocities of the walls were considered to be $V_{r2} = 0.2 \text{ m/s}$. The viscosity values are adopted from the approximate MSD values of the corresponding fluids from the particle tracking microrheology.

5.3. Results and Discussion

5.3.1 Effects of Lactic acid on Pig synovial Fluid

To investigate the microrheology of synovial fluid in elevated lactic acid conditions, pig synovial fluid is treated with lactic acid prior to the DWS measurements. **Figure 5.2a** shows the MSD vs. τ plot, where the 2x diluted pig SF shows a sub-diffusive behavior in contrast to the LA-treated pig SF which shows a purely diffusive behavior This is due to the phase separation of HA with the protein contents of the pig SF. Similar result is observed in the case of elastic modulus (G') and loss modulus (G'') as shown in **Figure 5.2b**. The 2x diluted pig SF shows a viscoelastic behavior while the lactic acid treatment shows a more fluidic behavior. Additionally, the FESEM image of untreated and treated pig SF reveals that pig SF possesses a nanoscaffold-like pattern (**Figure 5.2c**) with an average pore size of 500 nm. However, the lactic acid-treated one shows an aggregated scaffold-like pattern with minimal porosity (**Figure 5.2d**). This signifies that the lactic acid treatment leads to distortion of native nanoscaffolds of synovial fluid.

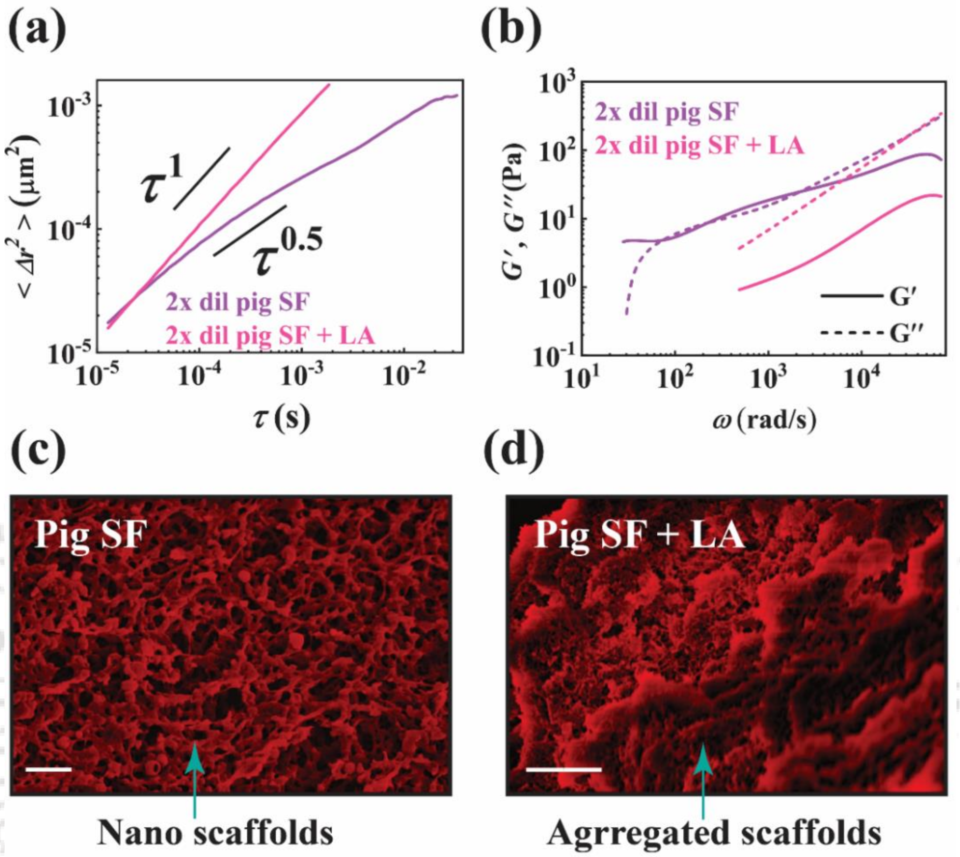

Figure 5.2. Effects of lactic acid on pig SF. (a) MSD vs. τ plot of 2x diluted pig SF in the presence or absence of lactic acid. (b) Elastic modulus and Loss modulus vs. frequency plot of 2x diluted pig SF in the presence or absence of lactic acid. (c) FESEM image of pig SF. (d) FESEM image of pig SF in the presence of lactic acid. The scale bar represents 1 µm, and the false color (red) is used in the images.

5.3.2. Effects of pH on the Microrheology and Bulk-rheology of HA and HA-Muc

Clinical studies report that the pH levels in synovial fluid (SF) shift from 7.6 in healthy individuals to 6.6 in RA patients due to elevated lactic acid concentration.[28,35,36] Several studies have reported a drastic alterations in the rheological properties of SF in RA, with one study attributing this to the lower molecular weight of hyaluronic acid (HA).[37] To better understand synovial fluid rheology under RA conditions in these pH conditions, we investigated the microrheology of HA and model SF at four different pH levels (7.4, 7.0, 6.6, and 6.2) relevant to the disease state.

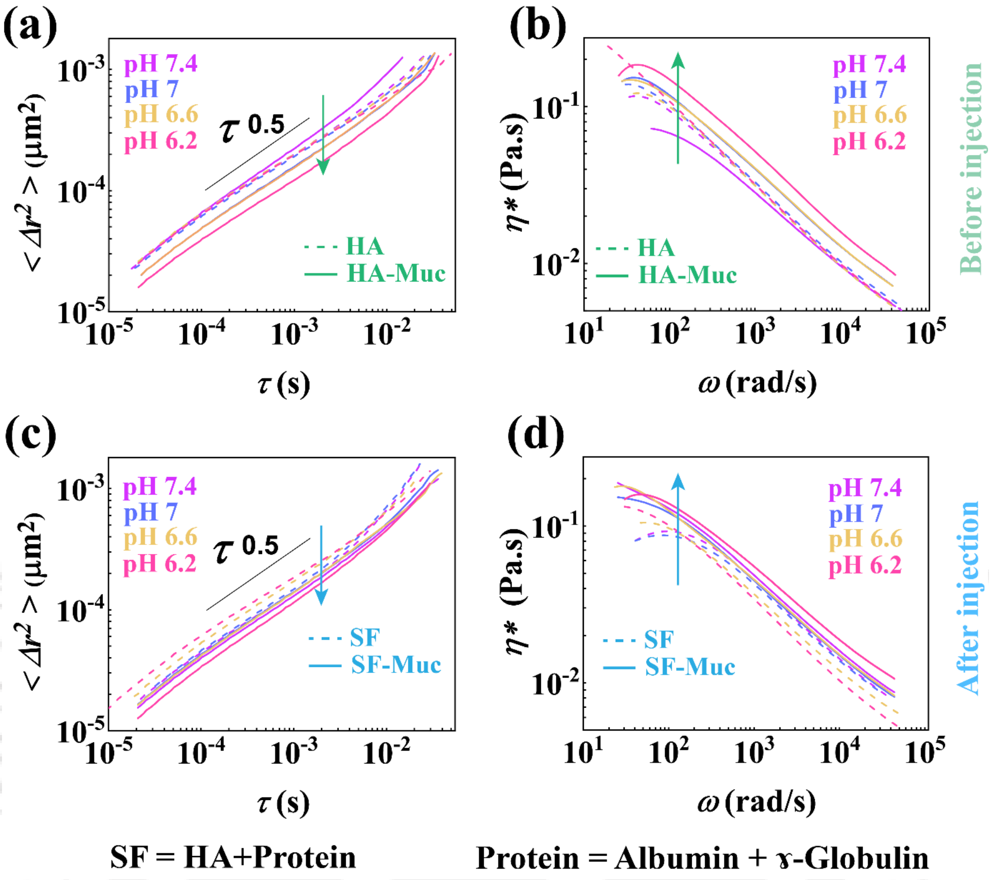

Figure 5.3. Microrheology of HA and model SF with varying pH conditions. (a) MSD vs. lag time (τ) of HA and HA-Muc. (b) Complex viscosity vs. shear rate plot of HA and HA-Muc. (c) MSD vs. lag time (τ) plot of model SF and SF-Muc. (d) Complex viscosity vs. shear rate plot of SF and SF-Muc.

Figure 5.3a shows the MSD vs. τ plot, where the MSD of HA remains constant across a range of physiological pH levels. In contrast, HA-Muc shows a pH-dependent behavior, with a decrease in MSD as the pH is lowered from 7.4 to 6.2. This result/observation is also reflected in **Figure 5.3b**, where the complex viscosity of HA remains largely unchanged, while that of HA-Muc increases as the pH decreases. These findings suggest that within this pH range, the viscoelastic properties of HA remain unaffected. However, the HA-Muc complex exhibits enhanced viscoelastic behavior due to interactions between HA and mucin.

Synovial fluid comprises distinct proteins including albumin, gamma globulin, lysozymes, and proteoglycans such as lubricin. In order to investigate the impact of mucin on synthetic synovial fluid within the synovium, we synthesized a model synovial fluid by incorporating HA, γ- globulin, and albumin as described in prior literature. Subsequently, we examined the microrheological properties of the fluid under a series of clinically relevant pH conditions. It can be observed in **Figure 5.3c** that the MSD of model SF tends to increase with decreasing pH. However, blended SF-muc exhibits a decreasing pattern of MSD with decreasing pH. A similar result is observed in the complex viscosity plot depicted in **Figure 5.3d** where the model SF shows a decreasing complex viscosity with decreasing pH and the mucin blended SF (SF-Muc) shows increasing complex viscosity. This may be attributed to the decreased interaction between HA and proteins at low pH conditions. However, in the presence of mucin, the interaction has been regained which resulted in higher complex viscosity.

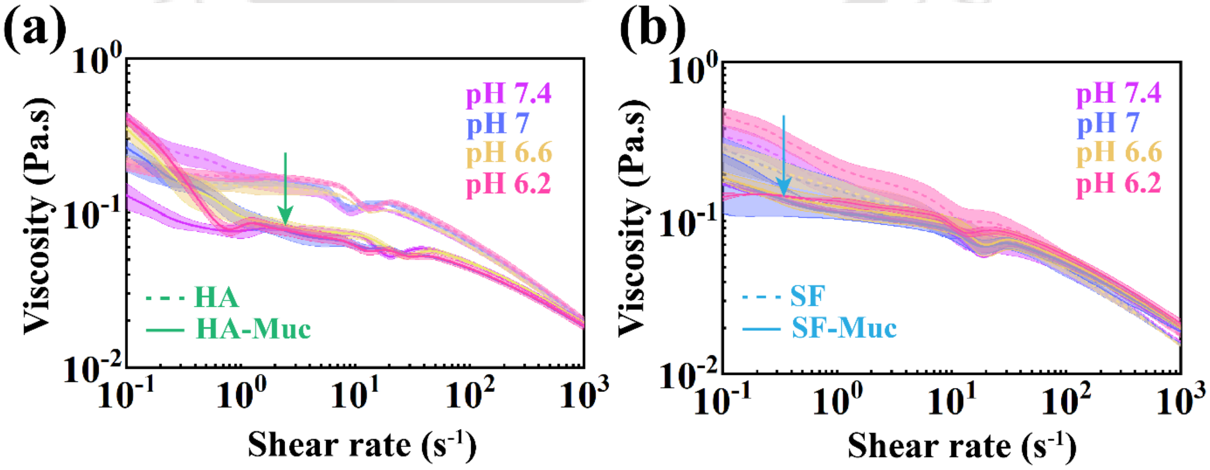

Figure 5.4. Bulk rheology of HA and model SF in the presence or absence of mucin. (a) Viscosity vs. Shear rate of HA and HA treated with Mucin at different pH conditions. (b) Viscosity vs. Shear rate of model SF and model SF treated with Mucin at different pH conditions.

Furthermore, the bulk rheology experiment reveals that the zero-shear viscosity of HA is the highest at pH 7.4 as shown in **Figure 5.4a,** while at lower pH settings there is no change in zero-shear viscosity of HA. Conversely, at a higher shear rate, changes in pH do not have any effects on HA viscosity.

Therefore, under physiologically relevant pH levels, HA viscosity is constant. This suggests that shift in pH within this range is not responsible for the breakdown of HA. In the case of mucin-treated HA, zero shear viscosity at pH 7.4 is the lowest. At decreasing pH, zero shear viscosity slightly increases, attaining a maxima at pH 6.2. This suggests that the in presence of mucin, zero shear viscosity changes with pH conditions. Interestingly, HA possesses a rapid shear thinning behavior compared to HA-Muc. A possible reason behind this may be noncovalent interactions between HA and Mucin. Additionally, in the case of model SF, the zero-shear viscosity of SF depends on the pH environment, as can be seen in **Figure 5.4b**. However, this pH dependency is not observed for the Mucin blended SF (SF-Muc), which shows a reduced zero shear viscosity compared to SF alone. The reduction of zero shear viscosity signifies the interaction between the HA and mucin. Interestingly, when drawing a comparison between the behaviors of the mucin-treated HA and mucin-treated SF, it is observed that SF-Muc has higher viscosity than the HA-Muc and exhibits a Newtonian behavior in low shear rate conditions. This could be due to the presence of albumin and gamma globulins in prepared model SF which might interact with mucin and impart some firm structures and resist the change in shear rate.

5.3.4. Morphological study of HA and HA-Muc by AFM

Furthermore, the morphological examination of HA and HA-Muc reveals distinct differences between HA and HA-Muc. HA showing a fibrous structure as shown in **Figure 5.5a-b** while HA-Muc showing a fibre bundle like structure as shown in **Figure 5.5c-d.** The height distance plot of HA suggests a maximum height of around 5.5 nm with a sharp peak distribution. However, HA-Muc shows a height of around 7.5 nm with broad peak distributions. This indicates the interaction between mucin and HA results in the formation of fiber bundles that resist the deformation at low shear rate conditions which might also help in boundary lubrication.

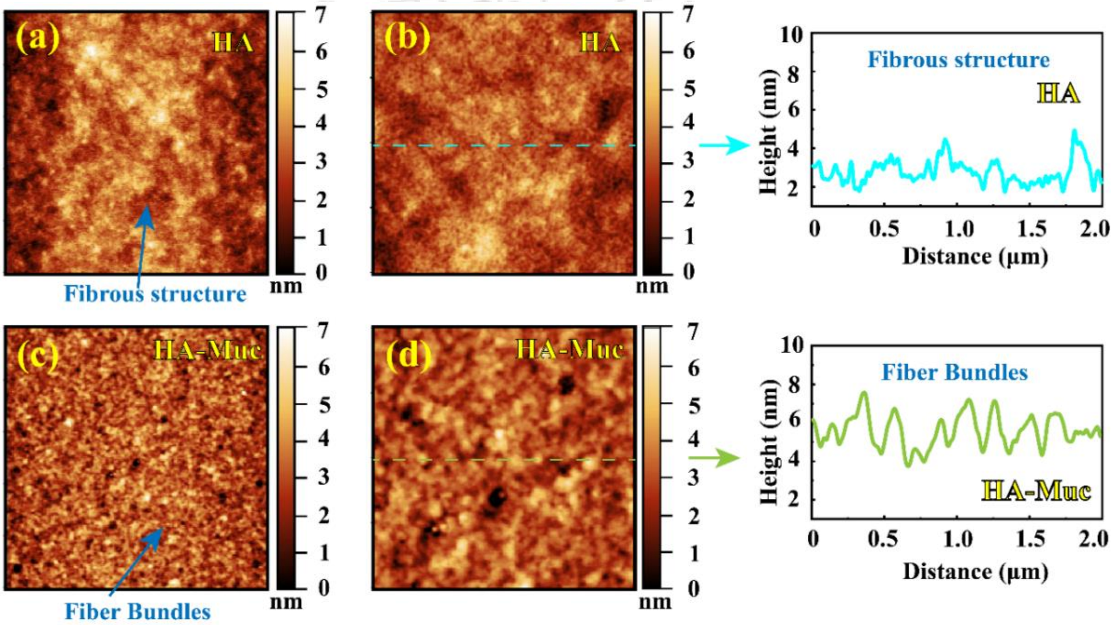

Figure 5.5. Morphological investigation of HA and HA-Muc using AFM. (a) 5×5 µm^2 of HA. (b) 2×2 µm^2 of HA with height distance profile. (c) 5×5 µm^2 of HA-Muc. (d) 2×2 µm^2 of HA-Muc with height distance profile.

5.3.5. Microrheology of HA and HA-Muc in a simulated RA joint

In the clinical study, elevated levels of lactic acid were found in the joints of patients with rheumatoid arthritis (RA).[36,38–40] To simulate an RA joint, two scenarios were considered: the pre-injection phase, where the microrheology of hyaluronic acid (HA) and the HA-mucin complex were studied in the presence of lactic acid, and the post-injection phase, where synovial proteins were added to the elevated lactic acid environment, referred to as the "after injection" scenario. As shown in **Figure 5.6a**, the mean square displacement (MSD) of the HA-mucin complex decreased compared to the HA control, likely due to noncovalent interactions between HA and mucin. In the presence of lactic acid, the MSD of HA increased slightly, potentially indicating HA fragmentation.[41,42] A significant reduction in MSD was observed in the presence of lactic acid for the HA-mucin complex, although this effect diminished at longer lag times. This behavior may result from a pH reduction due to the presence of lactic acid, as mucin viscosity increases under low pH conditions.[43,44]

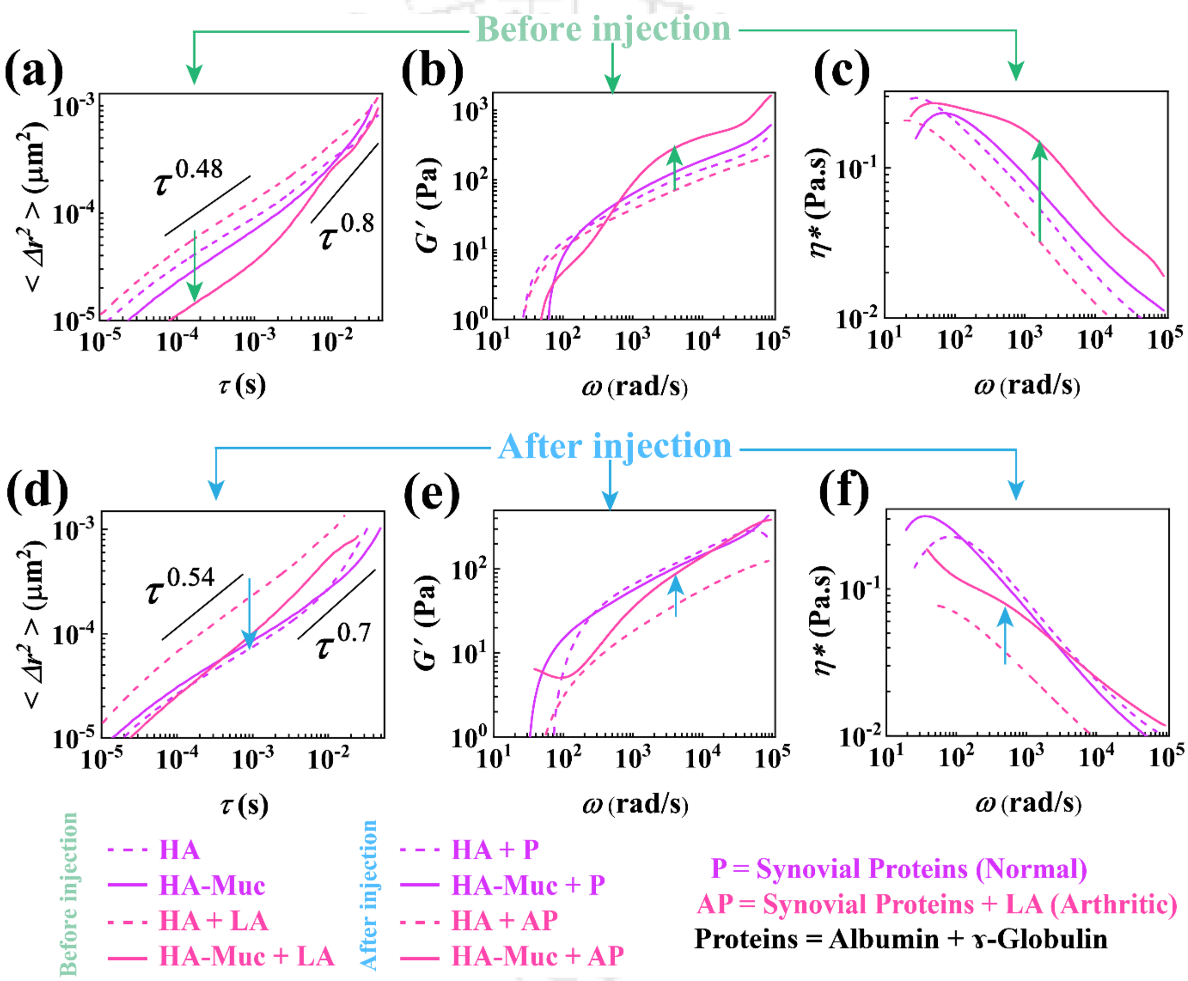

Figure 5.6. Microrheology of HA and HA-Muc in presence of protein and lactic acid environment. (a) MSD vs. τ plot of HA, and HA-Muc in presence or absence of LA. (b) Elastic modulus (G') and loss modulus (G'') vs. frequency (ω) plot of HA, and HA-Muc in presence or absence of LA. (c) Complex viscosity (η^*) vs. frequency (ω) of HA, and HA-Muc in presence or absence of LA. (d) MSD vs. τ plot of HA+P, and HA+P-Muc in presence or absence of LA. (e) Elastic modulus (G') and loss modulus (G'') vs. frequency (ω) plot of HA+P, and HA+P-Muc in presence or absence of LA. (f) Complex viscosity (η^*) vs. frequency (ω) of HA+P, and HA+P-Muc in presence or absence of LA.

Further analysis using the generalized Stokes-Einstein equation converted the MSD data into elastic moduli and complex viscosity. **Figure 5.6b** shows that the HA-mucin-lactic acid mixture exhibited the highest elastic modulus at high frequencies, suggesting increased stiffness in the presence of lactic acid. A similar phenomenon was observed in the complex viscosity vs. frequency plot in **Figure 5.6c**, where the HA-mucin complex displayed higher viscosity than HA alone, with lactic acid treatment further increasing the viscosity.

In the post-injection scenario, where proteins are present in the synovium, there is a significant increase in MSD for the lactic acid-treated HA-protein (HA+P) solution, seen in **Figure 5.6d**, which was not observed in the pristine HA sample, as discussed earlier. However, this MSD increase was absent in the HA-mucin-protein complex, suggesting that mucin stabilizes the viscoelastic properties of HA-protein in the presence of lactic acid. As seen in Figure 1e, the elastic modulus of the HA+P sample decreased in the presence of lactic acid, while the HA-mucin complex retained its elastic modulus, consistent with the MSD results. A similar pattern was observed in the complex viscosity vs. frequency plot in Figure 1f. This suggests that mucin preserves the viscoelastic properties of synovial fluid in the presence of lactic acid, highlighting the potential of the HA-mucin complex as a promising viscosupplement for arthritic patients.

Overall the experiment, it is observed that HA injection in the normal joint resulted in a nano scaffold-like pattern (**Figure 5.7a**), however in the RA joint due to elevated acidity, HA coprecipitates with the proteins present in the synovium. Conversely, HA-Muc injection also possesses a similar nano-scaffold-like pattern in the normal joints and RA joints (**Figure 5.7b**). The collective interaction between mucin and protein HA hinders the coprecipitation reaction at elevated lactic acid concentrations.

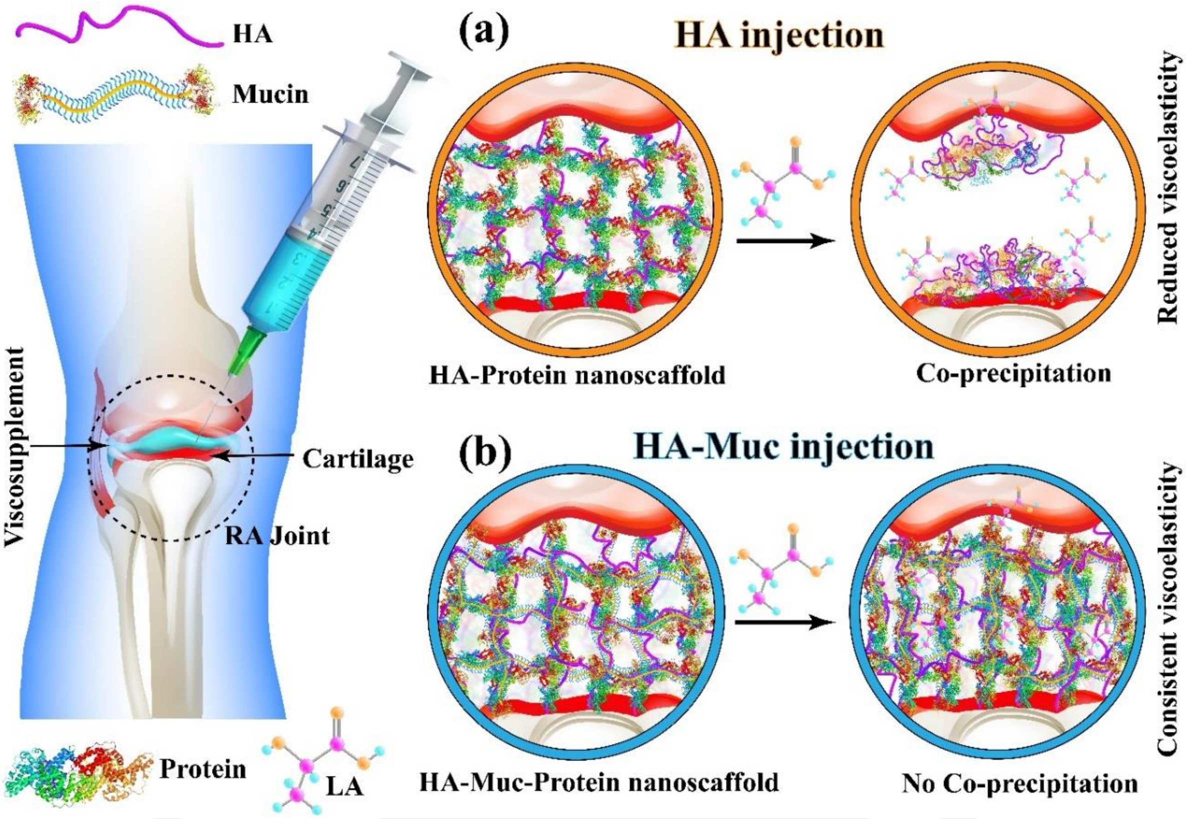

Figure 5.7. A schematic representation that depicts the behavior of the prepared HA and HA-Muc viscosupplements in a simulated rheumatoid arthritis (RA) joint. (a) In the presence of lactic acid, pristine HA co-precipitates with synovial proteins, compromising its function. (b) HA-Muc complex does not co-precipitate and retains its viscoelastic properties.

5.3.6. Interfacial microrheology of HA and HA-Muc on a collagen surface

In order to understand the viscoelastic behavior of HA and HA-Muc on the cartilage surface, there is a need to measure the microrheology at the interface between cartilage and the viscosupplement (either HA or HA-Muc). To achieve this, multiple particle tracking (MPT) microrheology is employed by using a confocal laser scanning microscope. A detailed description is provided in the materials and method section. The 3D image as shown in **Figure 5.8a** shows a two fluid-fluid interface between collagen and viscosupplement (either HA or HA-Muc). **Figure 5.8b** shows that the MSD of HA at the near interface possesses more than 10 times reduced MSD compared to at the upper interface. However, for the HA-Muc, the reduction is minimized as shown in **Figure 5.8c**. Interestingly, the power law exponent of HA and HA-Muc at the interfaces are 0.5 and 0.84 at low lag time.

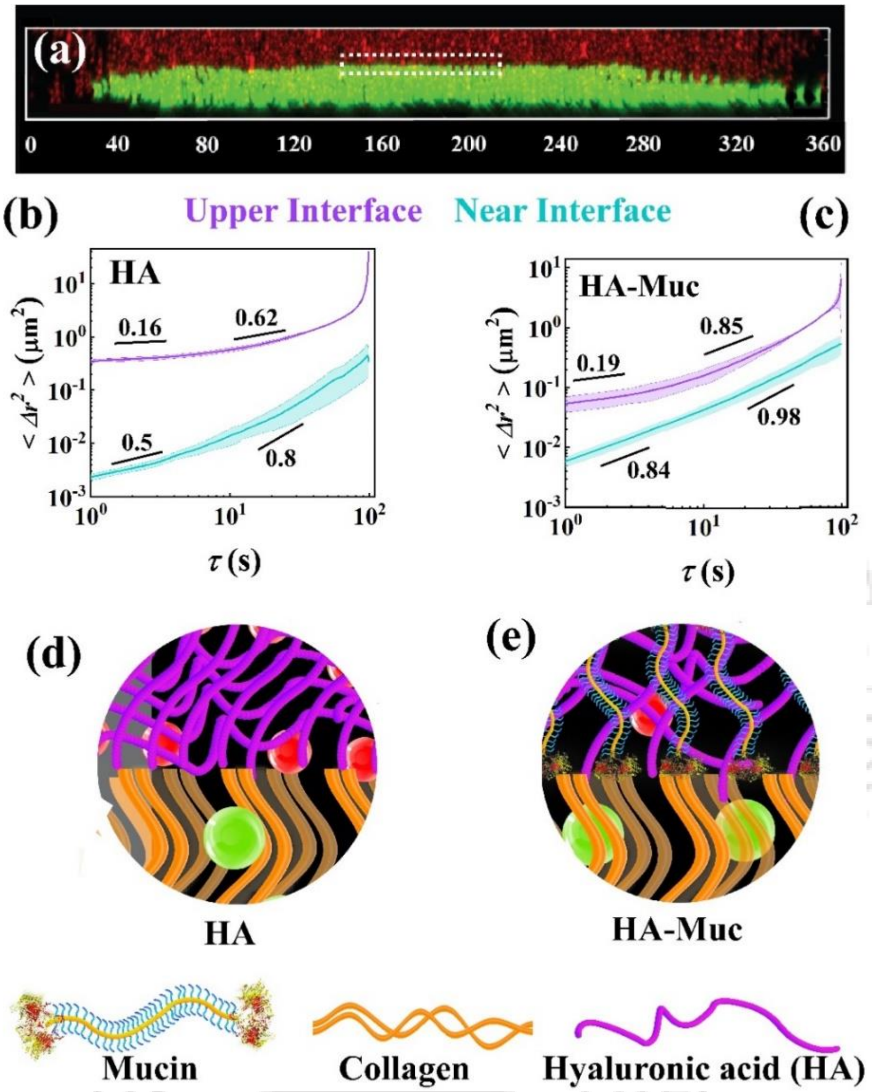

Figure 5.8. Microrheology at the collagen-viscosupplement interface. (a) 3D image of collagen-viscosupplement interface where the green tracer particles are embedded in collagen and red tracer particles are embedded in prepared viscosupplement. (b) MSD vs. τ plot of HA in the upper interface and at the near interface. (c) MSD vs. τ plot of HA-Muc in the upper interface and at the near interface. (d) Schematic representation of HA interacts with the collagen surface results in higher viscoelasticity. (e) Schematic representation of HA-Muc interacts with collagen surface resulted in less viscoelasticity.

A similar trend has been observed at high lag time also where the HA and HA-Muc power law exponents are 0.8 and 0.98. This signifies a more fluidic environment in the case of HA-Muc at the collagen interface compared to HA alone. The stiff behavior for HA might be due to higher collagen-HA interaction (**Figure 5.8d**). Conversely, the fluidic behavior of HA-muc might be arises due to increased interaction between collagen-mucin compared to HA (**Figure 5.8e**). Additionally, the upper interface of HA shows a higher MSD than the upper interface of HA-Muc. However, the power law exponent of HA is lower than HA-Muc. This indicates the HA shows a more stiffed behavior than the HA-Muc solution. Furthermore, to explore whether a low or high viscous environment is favorable for joint mobility, a COMSOL simulation has been performed. Interfacial viscosity is the combination of the both lower (collagen) and upper (viscosupplement) fluids. From the particle tracking experiments near the interface and the upper fluid, we have assumed near interface as a mixed layer of fluid which possess a higher viscosity than the upper fluid (viscosupplement) as described in the MSD calculation using a confocal laser scanning microscope. In the practical scenario, viscosupplement is sandwiched between the cartilage surfaces as shown in **Figure 5.7**.

It is well known that viscosity measures a fluid's resistance to deformation or flow, while a velocity profile represents the variation in fluid velocity across different layers. Viscosity stratification refers to changes in viscosity across fluid layers, which can significantly influence the velocity profile. In our simulation, we assume a Newtonian fluid with laminar flow, where the fluid moves in parallel layers with minimal mixing, making the impact of viscosity stratification more pronounced.

Dynamic viscosity μ directly affects the shear stress,

$$\tau = \mu_i \left(\nabla \mathbf{u}_i + \left(\nabla \mathbf{u}_i \right)^T \right), \tag{6}$$

here τ is the shear stress, μ_i is dynamic viscosity, and $\nabla \mathbf{u}_i$ is the velocity gradient.

Kinematic viscosity influences the rate of momentum diffusion,

$$v_i = \frac{\mu_i}{\rho_i}, \tag{7}$$

here v_i is the shear stress, μ_i is dynamic viscosity, and ρ_i is the density of the fluid.

In our simulation, we assume a Newtonian fluid with laminar flow, where the fluid moves in parallel layers with minimal mixing, making the impact of viscosity stratification more pronounced. We analyze lubrication and velocity profiles under two specific cases specified as case A and case B. Here, μ_{ij} denotes high viscosity fluid (*i*=1, *j*=A, B) near wall as explained in case A and case B, and μ_{ij} low viscosity fluid (*i* =2, *j*=A, B) at the centre as explained in case A and case B.

In case A, to replicate the highly viscous HA-collagen interface, two high-viscosity fluids (dynamic viscosity μ_{1A}) are positioned near the walls, with a low-viscosity fluid (dynamic viscosity μ_{2A}, where $\mu_{2A} < \mu_{1A}$) in the center (**Figure 5.9a**). In case B, to replicate the low viscous mucin blended (HA-Muc)—collagen interface the viscosity of the side fluids is slightly reduced $\mu_{1B} < \mu_{1A}$, and the middle fluid's viscosity is slightly increased $\mu_{2B} < \mu_{2A}$ (**Figure 5.9b**).

1. Case A (Higher Viscosity Fluids on the Sides)

The higher viscosity (μ_{1A}) near the walls results in a reduced velocity gradient in these regions compared to the central low-viscosity layer (μ_{2A}), which allows for higher velocity due to its lower resistance to deformation. The elevated viscosity near the walls also diminishes momentum transfer between the walls and adjacent fluid layers, while the less viscous middle layer experiences increased momentum transfer from its neighboring layers (**Figure 5.9a**). Consequently, the high viscosity near the walls generates greater shear stress, leading to increased frictional forces, even under slip conditions.

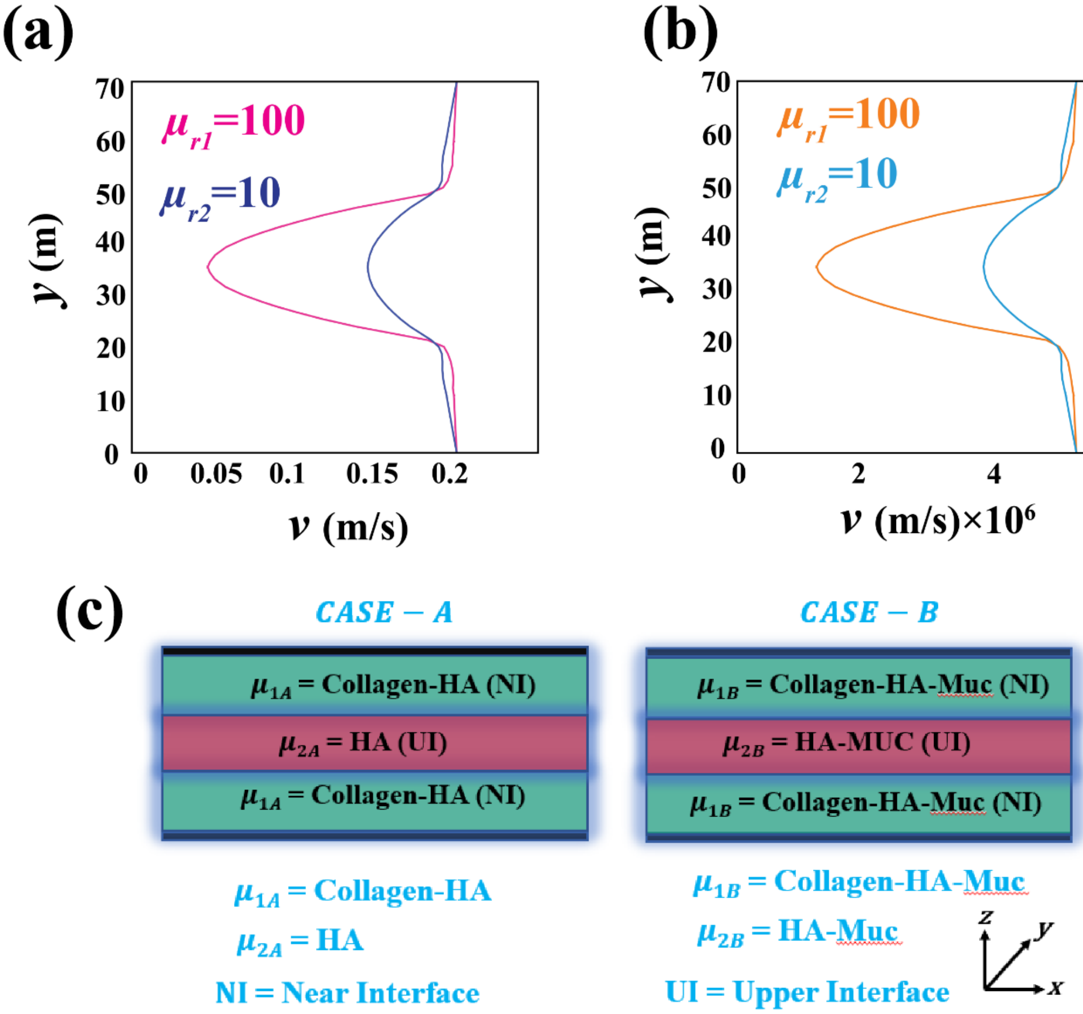

Figure 5.9. Velocity profile comparison of a high-viscosity fluid near the wall with low-viscosity fluid in the center (case A), and a low-viscosity fluid near the wall with high-viscosity fluid in the center (case B). (a) At low wall velocity. (b) At high wall velocity. (c) Schematic diagram of the computational model of Case A and Case B.

2. Case B (Reduced Viscosity of Side Fluids)

The reduced viscosity (μ_{1B}) near the walls, the velocity gradient in these regions increases compared to case A, while the middle layer (μ_{2B}) experiences only a modest increase in velocity due to the increased deformability of the adjacent layers as shown in **Figure 5.9 a-b**. The schematic representation of the computational model in consideration as shown in **Figure 5.9 c**. The lower viscosity near the walls enhances momentum transfer to and from the walls, further raising the velocity gradient (**Figure 5.9b**). Although the middle layer (μ_{2B}) continues to receive momentum transfer, the difference is less pronounced than in case A. The lower dynamic viscosity (μ_{1B}) near the walls reduces shear stress, leading to decreased frictional forces compared to case A.

Based on the discussion, we determine that in case B, lubrication is more effective due to the reduced viscosity (μ_{1B}) near the walls, which lowers frictional forces. This reduction results in a higher velocity gradient and smoother movement of the fluid layers, thereby enhancing the overall lubrication effect. Therefore, it is evident that the low viscous behavior at the interface between cartilage and HA-Muc helps in higher mobility compared to the higher viscous behavior between cartilage and HA. This leads to a higher velocity gradient and greater ease of movement for the fluid layers, enhancing the lubrication effect.

5.4. Conclusions

This chapter investigates the viscoelastic behavior of two potential viscosupplements, hyaluronic acid (HA) and Hyaluronic acid-mucin (HA-Muc), in a simulated arthritic joint environment. The initial study shows that adding lactic acid to pig synovial fluid causes co-precipitation and, as revealed by microrheological analysis, leads to a complete loss of viscoelasticity. This indicates that HA-based viscosupplements may be ineffective in managing elevated lactic acid levels associated with rheumatoid arthritis (RA). Additionally, FESEM analysis demonstrates that the nanoscaffold structure of native pig synovial fluid is disrupted by lactic acid treatment. Further, the pH study shows no significant changes in HA microrheology across clinically relevant pH levels, while a decrease in pH enhances the viscoelastic behavior of HA-Muc. In contrast to microrheology, bulk rheology experiments reveal that mucin decreases HA's viscosity at low shear rates and slows its deformation, compared to pure HA solutions. This is due to the transition of fibrous structure of HA to a fiber bundle like structure in presence of mucin as evident from the AFM analysis. Further, microrheological studies that HA-Muc retains its viscoelastic properties in simulated arthritic conditions, unlike HA alone. Furthermore, microrheology at the collagen interface, HA-Muc exhibits a more fluidic behavior, whereas HA interacts with collagen to produce an elastic response. This fluidity aids joint movement and provides boundary lubrication. Overall, this research paves the way for developing mucin-blended hyaluronic acid as a novel viscosupplement for treating rheumatoid arthritis.

References

(1) Murphy, A. C.; Muldoon, S. F.; Baker, D.; Lastowka, A.; Bennett, B.; Yang, M.; Bassett, D. S. Structure, Function, and Control of the Human Musculoskeletal Network. *PLOS Biol.* **2018**, *16* (1), 1–27. https://doi.org/10.1371/journal.pbio.2002811.

(2) Boskey, A. L.; Robey, P. G. The Composition of Bone. In *Primer on the Metabolic Bone Diseases and Disorders of Mineral Metabolism*; John Wiley & Sons, Ltd; pp 49–58. https://doi.org/https://doi.org/10.1002/9781118453926.ch6.

(3) Whillis, J. The Development of Synovial Joints. *J. Anat.* **2007**, *74*, 277–283.

(4) Schurz, J.; Ribitsch, V. Rheology of Synovial Fluid. *Biorheology* **1987**, *24*, 385–399. https://doi.org/10.3233/BIR-1987-24404.

(5) Oates, K. M. N.; Krause, W. E.; Jones, R. L.; Colby, R. H. Rheopexy of Synovial Fluid and Protein Aggregation. *J. R. Soc. Interface* **2006**, *3* (6), 167–174. https://doi.org/10.1098/rsif.2005.0086.

(6) Cook, S. G.; Guan, Y.; Pacifici, N. J.; Brown, C. N.; Czako, E.; Samak, M. S.; Bonassar, L. J.; Gourdon, D. Dynamics of Synovial Fluid Aggregation under Shear. *Langmuir* **2019**, *35* (48), 15887–15896. https://doi.org/10.1021/acs.langmuir.9b02028.

(7) Toole, B. P. Hyaluronan: From Extracellular Glue to Pericellular Cue. *Nat. Rev. Cancer* **2004**, *4* (7), 528–539. https://doi.org/10.1038/nrc1391.

(8) Lapcík L Jr and, L.; Lapcík, L.; De Smedt, S.; Demeester, J.; Chabrecek, P. Hyaluronan: Preparation, Structure, Properties, and Applications. *Chem. Rev.* **1998**, *98* (8), 2663–2684. https://doi.org/10.1021/cr941199z.

(9) Zhang, Z.; Barman, S.; Christopher, G. F. The Role of Protein Content on the Steady and Oscillatory Shear Rheology of Model Synovial Fluids. *Soft Matter* **2014**, *10* (32), 5965–5973. https://doi.org/10.1039/c4sm00716f.

(10) Jay, G. D.; Torres, J. R.; Warman, M. L.; Laderer, M. C.; Breuer, K. S. The Role of Lubricin in the Mechanical Behavior of Synovial Fluid. *Proc. Natl. Acad. Sci.* **2007**, *104* (15), 6194–6199. https://doi.org/10.1073/pnas.0608558104.

(11) Liddle, A. D.; Pegg, E. C.; Pandit, H. Knee Replacement for Osteoarthritis. *Maturitas* **2013**, *75* (2), 131–136. https://doi.org/10.1016/j.maturitas.2013.03.005.

(12) Conrozier, T.; Raman, R.; Chevalier, X.; Henrotin, Y.; Monfort, J.; Diraçoglù, D.; Bard, H.; Baron, D.; Jerosch, J.; Richette, P.; Migliore, A. Viscosupplementation for the Treatment of Osteoarthritis. The Contribution of EUROVISCO Group. *Ther. Adv. Musculoskelet. Dis.* **2021**, *13*, 1759720X211018605. https://doi.org/10.1177/1759720X211018605.

(13) DeMoya, C. D.; Joenathan, A.; Lawson, T. B.; Felson, D. T.; Schaer, T. P.; Bais, M.; Albro, M. B.; Mäkelä, J.; Snyder, B. D.; Grinstaff, M. W. Advances in Viscosupplementation and Tribosupplementation for Early-Stage Osteoarthritis Therapy. *Nat. Rev. Rheumatol.* **2024**, *20* (7), 432–451. https://doi.org/10.1038/s41584-024-01125-5.

(14) Shime, H.; Yabu, M.; Akazawa, T.; Kodama, K.; Matsumoto, M.; Seya, T.; Inoue, N. Tumor-Secreted Lactic Acid Promotes IL-23/IL-17 Proinflammatory Pathway. *J. Immunol.* **2008**, *180* (11), 7175–7183. https://doi.org/10.4049/jimmunol.180.11.7175.

(15) Pucino, V.; Nefla, M.; Gauthier, V.; Alsaleh, G.; Clayton, S. A.; Marshall, J.; Filer, A.; Clark, A. R.; Raza, K.; Buckley, C. D. Differential Effect of Lactate on Synovial Fibroblast and Macrophage Effector Functions. *Front. Immunol.* **2023**, *14*. https://doi.org/10.3389/fimmu.2023.1183825.

(16) Radu, A.-F.; Bungau, S. G. Management of Rheumatoid Arthritis: An Overview. *Cells* **2021**, *10* (11). https://doi.org/10.3390/cells10112857.

(17) Bullock, J.; Rizvi, S. A. A.; Saleh, A. M.; Ahmed, S. S.; Do, D. P.; Ansari, R. A.; Ahmed, J. Rheumatoid Arthritis: A Brief Overview of the Treatment. *Med. Princ. Pract. Int. J. Kuwait Univ. Heal. Sci. Cent.* **2018**, *27* (6), 501–507. https://doi.org/10.1159/000493390.

(18) De Lucia, O.; Murgo, A.; Pregnolato, F.; Pontikaki, I.; De Souza, M.; Sinelli, A.; Cimaz, R.; Caporali, R. Hyaluronic Acid Injections in the Treatment of Osteoarthritis Secondary to Primary Inflammatory Rheumatic Diseases: A Systematic Review and Qualitative Synthesis. *Adv. Ther.* **2020**, *37* (4), 1347–1359. https://doi.org/10.1007/s12325-020-01256-7.

(19) Sprott, H.; Fleck, C. Hyaluronic Acid in Rheumatology. *Pharmaceutics* **2023**, *15* (9). https://doi.org/10.3390/pharmaceutics15092247.

(20) Alarcon, P.; Hidalgo, A. I.; Manosalva, C.; Cristi, R.; Teuber, S.; Hidalgo, M. A.; Burgos, R. A. Metabolic Disturbances in Synovial Fluid Are Involved in the Onset

of Synovitis in Heifers with Acute Ruminal Acidosis. *Sci. Rep.* **2019**, *9* (1), 1–12. https://doi.org/10.1038/s41598-019-42007-1.

(21) Chang, X.; Wei, C. Glycolysis and Rheumatoid Arthritis. *Int. J. Rheum. Dis.* **2011**, *14* (3), 217–222. https://doi.org/10.1111/j.1756-185X.2011.01598.x.

(22) Zou, Y.; Zeng, S.; Huang, M.; Qiu, Q.; Xiao, Y.; Shi, M.; Zhan, Z.; Liang, L.; Yang, X.; Xu, H. Inhibition of 6-Phosphofructo-2-Kinase Suppresses Fibroblast-like Synoviocytes-Mediated Synovial Inflammation and Joint Destruction in Rheumatoid Arthritis. *Br. J. Pharmacol.* **2017**, *174* (9), 893–908. https://doi.org/10.1111/bph.13762.

(23) Dröge, W.; Roth, S.; Altmann, A.; Mihm, S. Regulation of T-Cell Functions by l-Lactate. *Cell. Immunol.* **1987**, *108* (2), 405–416. https://doi.org/https://doi.org/10.1016/0008-8749(87)90223-1.

(24) Anderson, J. R.; Phelan, M. M.; Clegg, P. D.; Peffers, M. J.; Rubio-Martinez, L. M. Synovial Fluid Metabolites Differentiate between Septic and Nonseptic Joint Pathologies. *J. Proteome Res.* **2018**, *17* (8), 2735–2743. https://doi.org/10.1021/acs.jproteome.8b00190.

(25) Gobelet, C.; Gerster, J. C. Synovial Fluid Lactate Levels in Septic and Non-Septic Arthritides. *Ann. Rheum. Dis.* **1984**, *43* (5), 742–745. https://doi.org/10.1136/ard.43.5.742.

(26) Gobelet, C.; Gerster, J. C. Synovial Fluid Lactate Levels in Septic and Non-Septic Arthritides. *Ann. Rheum. Dis.* **1984**, *43* (5), 742–745. https://doi.org/10.1136/ard.43.5.742.

(27) Ward, T. T.; Steigbigel, R. T. Acidosis of Synovial Fluid Correlates with Synovial Fluid Leukocytosis. *Am. J. Med.* **1978**, *64* (6), 933–936. https://doi.org/10.1016/0002-9343(78)90446-1.

(28) Pucino, V.; Certo, M.; Bulusu, V.; Cucchi, D.; Goldmann, K.; Pontarini, E.; Haas, R.; Smith, J.; Headland, S. E.; Blighe, K.; Ruscica, M.; Humby, F.; Lewis, M. J.; Kamphorst, J. J.; Bombardieri, M.; Pitzalis, C.; Mauro, C. Lactate Buildup at the Site of Chronic Inflammation Promotes Disease by Inducing CD4+ T Cell Metabolic Rewiring. *Cell Metab.* **2019**, *30* (6), 1055-1074.e8. https://doi.org/https://doi.org/10.1016/j.cmet.2019.10.004.

(29) Kakati, N.; Ahari, D.; Parmar, P. R.; Deshmukh, O. S.; Bandyopadhyay, D. Lactic Acid-Induced Colloidal Microrheology of Synovial Fluids. *ACS Biomater. Sci. Eng.* **2024**. https://doi.org/10.1021/acsbiomaterials.3c01846.

(30) Gonzales, G.; Zauscher, S.; Varghese, S. Progress in the Design and Synthesis of Viscosupplements for Articular Joint Lubrication. *Curr. Opin. Colloid Interface Sci.* **2023**, *66*, 101708. https://doi.org/https://doi.org/10.1016/j.cocis.2023.101708.

(31) Vincent, H. K.; Percival, S. S.; Conrad, B. P.; Seay, A. N.; Montero, C.; Vincent, K. R. Hyaluronic Acid (HA) Viscosupplementation on Synovial Fluid Inflammation in Knee Osteoarthritis: A Pilot Study. *Open Orthop. J.* **2013**, *7* (1), 378–384. https://doi.org/10.2174/1874325001307010378.

(32) Makvandi, P.; Della Sala, F.; di Gennaro, M.; Solimando, N.; Pagliuca, M.; Borzacchiello, A. A Hyaluronic Acid-Based Formulation with Simultaneous Local Drug Delivery and Antioxidant Ability for Active Viscosupplementation. *ACS Omega* **2022**, *7* (12), 10039–10048. https://doi.org/10.1021/acsomega.1c05622.

CHAPTER 6

Summary and Future Scope

Contents


भारतीय प्रौद्योगिकी संस्थान गुवाहाटी
Indian Institute of Technology Guwahati

6.1. Summary

This thesis utilizes the DWS microrheology as a tool to measure the viscoelastic behavior of two different biofluids namely mucin and synovial fluid. The use of different biophysical techniques like Circular dichroism, Fluorescence spectroscopy, and ξ-potential helps to uncover the molecular insights of these two biofluids. Additionally, quantum chemical calculation helps to elucidate the possible interactive forces between the molecules. This thesis provides an insight into establishing a bridge between rheology and molecular biology offering a deeper understanding of the molecular mechanism of viscoelasticity of biofluids. The crucial findings of this thesis are explained as follows—

In Chapter 2, the thesis explores the microrheological study of mucin and mucin-albumin complexes, demonstrating an increased complex viscosity compared to the pristine mucin. This enhancement is due to forming a compact networked structure as visualized by atomic force microscopy (AFM). Further study using ITC, reveals a weak binding force between mucin and albumin. However, this binding is pH dependent as evidenced by the microrheology of mucin-albumin at varying pH conditions which signifies the possible electrostatic interaction between mucin and albumin. The study also highlights the impacts of Ca^{2+} ions on this binding process and observes that introducing Ca^{2+} ions enhances the albumin-mucin interaction and increases viscous and elastic behavior. Further Circular dichroism (CD) spectra reveal that the mucin-albumin complex possesses an alpha-helical structure at pH 7.4 in contrast to the random coil structure of pristine mucin. These findings suggest that the albumin electrostatically binds with mucin and facilitates mucin assembly which leads to a compact networked structure. This structure might enhance the protective function of a mucus layer by potentially causing a barrier against pathogens and protecting the epithelial linings. However, this study also highlights the non-mucin protein and mucin interaction is not favorable for protein-based oral drug delivery as the drug might interact with the mucin and lead to slow diffusion. To circumvent this issue, we used ionic liquid which has been described in Chapter 3 of the thesis.

In Chapter 3, we delved into the microrheological investigation of mucin with a choline bicarbonate maleic acid (CBMA) based ionic liquid. The introduction of CBMA ionic liquid in the mucin solution resulted in decreased mean squared displacements (MSD), indicating aggregation of mucins. Atomic force microscopy (AFM) analysis suggests the aggregation of mucin after CBMA treatment compared to thread-like patterns in pristine mucin. To validate the protein-based drug and mucin interaction bovine serum albumin has been considered as a model protein-based drug. As observed in Chapter 2, albumin binds with the mucin and forms a more compact structure which leads to decreased MSD of probed particles. However, these changes in MSD are minimal in the case of CBMA treatment suggesting a lower binding affinity between mucin and the model drug albumin. Further, in the DFT simulation study, the charge transfer (CT) process plays an important role in closed-range charged interactions between the components of IL-mucin, which are in the following order: cysteine (−0.3e) < sialic acid (−0.263e) < GalNAc (−0.084e). The DFT simulation indicates the CBMA ionic liquid shields the negatively charged sialic acid present in the mucin leading to aggregation. It was established that interactions occurred at both short and medium ranges, with the IL-mucin components separated by a range of 1.52 to 2.2Å. The analysis of electron cloud distribution and the evolution of H-bonding, electrostatic as well as dispersion interactions—all of which have been confirmed by the NCI/RDG analysis—were caused by the presence of multiple electrophilic and nucleophilic active sites within the molecular groups present in the systems, as demonstrated by the ESP charge analysis. Furthermore, it has also been observed that the CBMA also interacts with the cysteine domain of mucin which is crucial for mucin non-mucin and mucin to the mucin interaction site. As a result, the model drug albumin could not bind to the cysteine domain and pave the way for a faster diffusion. To further explore this, a mucus-on-a-chip device was fabricated to simulate the intestine and assess the diffusion of an antibody. The results confirmed that the CBMA treatment leads to an enhanced diffusion of the antibody compared to the untreated one.

In Chapter 4, we studied the impacts of lactic acid, an anaerobic byproduct resulting from the hypoxic environment inside the joints, on synovial fluid. The microrheological study reveals that the normal synovial fluid possesses a viscoelastic behavior with a shear-thinning property. However, at elevated lactic acid concentration this viscoelastic behavior diminishes and shows a purely viscous Newtonian behavior. The AFM study, reveals that the normal synovial fluid possesses a nanoscaffold-like pattern that deteriorates and forms aggregations upon lactic acid treatment. However, upon lactic acid treatment. To further explore this, a model synovial fluid is prepared using hyaluronic acid, albumin, and gamma globulin and treated with varying concentrations of lactic acid. The result showed that beyond a critical limit (1mg/mL) of lactic acid, the model synovial fluid loses its viscoelasticity. The ξ-potential measurements show that albumin acquires a positive charge in the presence of an elevated quantity of LA, allowing it to interact with a negatively charged HA and produce the observed changes. Additionally, the CD spectra of BSA treated with LA lead to the unfolding of albumin which results in exposing more charged groups and promotes the electrostatic interaction with HA. This study indicates that the conventional hyaluronic acid-based viscosupplement might not be effective for arthritis as it might coprecipitate with the acidic proteins inside the arthritic joints. Therefore, there is a need for the development of an effective viscosupplement that can withstand such acidic environments.

In Chapter 5, we have prepared a mucin-blended hyaluronic acid viscosupplement for rheumatoid arthritis conditions. The microrheological study reveals that the mucin-blended hyaluronic acid retains its viscoelasticity at elevated lactic acid concentrations in contrast to pristine hyaluronic acid which is prone to phase separation with the synovial proteins. Hence this formulation could serve as a more effective viscosupplement for rheumatoid arthritis patients. Furthermore, the microrheological measurements at the near interface between collagen and prepared viscosupplement reveal that the mucin-blended hyaluronic acid possesses a less viscous layer at the interface which is beneficial for boundary lubrication at high load conditions as well as helps in joint mobility.

Overall, the thesis employs DWS to measure the viscoelastic behavior of two biomaterials Mucin and Synovial fluid, along with various biophysical techniques to characterize their molecular properties. A significant finding is that a non-mucin protein albumin promotes the hierarchical assembly of mucin through electrostatic interactions and forms a compact functional mucus layer. However, this non-mucin protein and mucin interaction is not favorable for protein-based oral drug delivery. This issue can be addressed by using choline bicarbonate – maleic acid ionic liquid, which interferes with the binding sites of mucin with the therapeutic drugs. Another important biomaterial is synovial fluid, where it is found that lactic acid degrades the viscoelastic properties of synovial fluid specially in the case of rheumatoid arthritis conditions. This highlights the need for improved viscosupplements that can function in acidic joints. Further, this issue can be mitigated by the use of a mucin-blended hyaluronic acid that has emerged as an alternative viscosupplement for rheumatoid arthritis problems.

6.2 Future Scopes

The extensive studies and findings from this thesis pave the way for future explorations, which can be extended in the following ways—

- The microrheology of mucin presented in this thesis could be further explored using a human mucus-on-chip model to achieve more physiologically relevant results. Additionally, studying the microrheology of human mucus from patients with conditions such as cystic fibrosis, chronic inflammatory bowel disease, and asthma may offer deeper insights into the pathological characteristics of these diseases and contribute to the development of more effective treatments.
- The design and development of compounds that modify mucus could be highly effective for drug delivery and therapeutic applications. Developing an effective mucus-modulating agent that improves the permeability of protein-based drugs across the mucus barrier would greatly advance both oral drug delivery and targeted therapeutic systems.
- The design and development of an effective therapeutic viscosupplement is essential for the comprehensive treatment of all types of arthritis. The rising incidences of various arthritic conditions globally underscore the pressing need for a viscosupplement that can effectively target both inflammatory and non-inflammatory types of arthritis.
- Microrheology of the tumor microenvironment is crucial for creating a tumor model suitable for drug screening applications. Developing an in vitro tumor model that accurately mimics in vivo tumor behavior is essential for screening various cancer drugs and conducting fundamental research. This necessitates a thorough understanding of the mechanical properties of the tumor microenvironment.

Appendix

Description of Videos, Publications, Conferences, and Patents

.

A1.1 Description of Video

CHAPTER-3:

1. Video 1: Spatiotemporal evolution of a droplet of BSA, HA, and model SF when treated with LA

A1.2 International Publications (From Thesis Work)

1. **N. Kakati**, D Ahari, P. R. Parmar, O. S. Deshmukh, and D. Bandyopadhyay, "Lactic Acid-Induced Colloidal Microrheology of Synovial Fluids", ACS Biomaterial Science and Engineering, 2024.
2. **N. Kakati**, C. K. Parashar, S. Thakur, O. S. Deshmukh, and D. Bandyopadhyay, "Microrheology of Mucin–Albumin Assembly Using Diffusing Wave Spectroscopy", ACS Applied Biomaterials, 2022.
3. **N. Kakati**, N. Paul, S. Dubey, J. Mahanta, A.R. Lakshmi, T. Banerjee, and D. Bandyopadhyay, "Microrheological Investigation of Ionic Liquid Treated Mucus for Effective Delivery of Protein-Based Drugs", (Under review).
4. **N. Kakati,** R. Deka, S. Agrawal, S. Dubey, S. Dey, P.R. Paramar, Omkar Suresh Deshmukh, Dipankar Bandyopadhyay, "Effects of Mucin on Synovial Fluid Microrheology for the Development of Artificial Synovial Fluid", (Under preparation).

A1.3. International Publications (In Collaboration)

1. P.R. Parmar, N. Yadav, N. Arfa, T. Ghoshal, J. Mahanta, **N. Kakati**, V. B. Vanarse, D. Bandyopadhyay, "Microdroplet Sensor for Point-of-Care-Testing of Glycemic Index Using Gold-Amylase Nanocomposite", IEEE Journal of Flexible Electronics, 2023.
2. A. Dixit, C. K. Parashar, S. Dutta, J. Mahanta, **N. Kakati**, D. Bandyopadhyay, "A Microfluidic Viscometer: Translation of Oscillatory Motion of a Water Microdroplet in Oil under Electric Field", Electrophoresis, 2021.

A1.3. Conferences

1. **N. Kakati**, D. Bandyopadhyay, “Microrheology of Biofluid in Health and Diseases”, Indo-German Workshop, IIT Kharagpur, 2024

2. **N. Kakati**, N. Paul, D. Bandyopadhyay, “Effects of Choline bicarbonate: maleic acid-based Ionic Liquids on the Microrheology of Mucus”, EBSA Congress, Stockholm, 2023

3. **N. Kakati**, P.R. Paramar, O.S. Deshmukh, D. Bandyopadhyay, “Effects of Lactic acid on Synovial Fluid”, CompFlu, IIT Kharagpur, 2022

A1.3. Patent

1. POCT device to detect cervical cancer-specific biomarker; Applicant: IIT Guwahati, CSIR; Indian patent; Patent no: 374832; Award date: 18-080 2021.


भारतीय प्रौद्योगिकी संस्थान गुवाहाटी
Indian Institute of Technology Guwahati